# MESOSCOPE: A MINIATURIZED HEADMOUNTED DEVICE FOR WHOLE CORTEX MESOSCALE ACTIVITY MAPPING IN FREELY BEHAVING MICE

By

DANIEL ALEXANDER SURINACH

A thesis submitted in partial fulfillment of
the requirements for the degree of

MASTER OF SCIENCE

UNIVERSITY OF MINNESOTA, TWIN CITIES
Mechanical Engineering

AUGUST 2020

## ACKNOWLEDGMENT

I would like to acknowledge Mathew Rynes, who helped formulate and explore the initial design for the device and experiments. He helped immensely throughout the scope of the project on everything from surgical work, to experiment design, to animal handling and training, and to computational data processing used throughout the manuscript.

I would like to thank Samantha Linn and Vijay Rajendran for all their help setting up experiments, making implants, and writing data analysis pipeline code used throughout the manuscript. I would like to thank Michael Laroque and Judith Dominguez for their immense help with device CAD design, benchtop testing and designing the open field a rena. I would also like to thank Zahra Sadat Navabi for her help with several surgeries. I would like to acknowledge Leila Ghanbari for her mentorship in the lab and for her help with See-Shell implant modification, the basis that made these types of experiments possible.

I am very grateful to Professor Suhasa Kodandaramaiah for guiding us through the project and pushing us to meet new standards in engineering that made this work possible. I am very thankful to have an amazing collaborative environment and lab group, who were always very welcoming, entertaining, and collaborative to push ideas and methods off of during my thesis.

I am very thankful to everyone who has provided support throughout this exciting and engaging period where I learned a lot about engineering in research.

MESOSCOPE: A MINIATURIZED HEADMOUNTED DEVICE FOR WHOLE CORTEX MESOSCALE ACTIVITY MAPPING IN FREELY BEHAVING MICE


Abstract

by Daniel Alexander Surinach, M.Sc.
University of Minnesota, Twin Cities
August 2020

PI: Suhasa Kodandaramaiah

The advent of genetically encoded calcium indicators, along with surgical preparations such as thinned skulls or refractive index matched skulls, have enabled mesoscale cortical activity imaging in head-fixed mice. Such imaging studies have revealed complex patterns of coordinated activity across the cortical surface during spontaneous behaviors, goal-directed behavior, locomotion, motor learning and perceptual decision making in head-fixed animals. However, neural activity during free, unrestrained behavior significantly differs from that recorded in head-fixed animals. Furthermore, freely moving animals exhibit a repertoire of behaviors that is vastly increased from head-fixed animals, and therefore the ability to perform mesoscale imaging of the cortex in freely behaving mice needs further investigation.

Here we present the "Mesoscope", a miniature, head-mountable imaging device compatible with transparent polymer skulls recently developed by our group. With an 8x10 $mm$ field of view, the Mesoscope can image most of the mouse dorsal cortex with a resolution ranging from 39.37 to 55.68 $\mu m$. The Mesoscope weighs 3.8 $g$ (<15% of a mouse's body

weight) and incorporates a magnetic interlocking mechanism that allows quick fixation (<1 $s$ of temporary restraint) to a 3D-printed morphologically realistic transparent polymer skull (See-Shell) implanted on an awake mouse. Open-field behavior tests indicate neither the See-Shell implantation nor the addition of Mesoscope significantly inhibits locomotion. The Mesoscope employs an array of blue LEDs to illuminate the cortical surface uniformly, with up to 31 $mW$ of light power. An additional green LED provides illumination for reflectance imaging of intrinsic optical signals arising from changes in cortical blood volume and oxygenation following neural activity. The LEDs are powered using a custom-designed printed circuit board that allows for fast LED switching on a microsecond scale.

We have used the Mesoscope to record neural activity across the dorsal cortex in mice during in a variety of different behaviors described as follows: spontaneous neural activity under light isoflurane anesthesia, sensory evoked neural responses under light isoflurane anesthesia, spontaneous neural activity during free awake behavior, spontaneous neural activity during awake social behavior, and spontaneous neural activity during sleep. The Mesoscope employs compact optical and electrical technologies that can perform mesoscale imaging across the dorsal cortex in freely moving and behaving mice and will potentially open new avenues of scientific inquiry.

# TABLE OF CONTENTS

# LIST OF TABLES

# LIST OF FIGURES

# Chapter One

# Introduction

Over the last several decades, neuroscientists have made significant strides to understand how neuronal computations occurring in isolated circuits in the brain mediate behavior. More recently, the advent of genetically encoded calcium[1] and voltage indicators,[2,3] along with transgenic approaches for broadly expressing these indicators in the brain in a cell type specific fashion[4,5] have enabled mesoscale imaging of multiple cortical regions simultaneously.[6–8] These studies have revealed how neural activity across multiple regions of the cortex are coordinated in a variety of behaviors.[9–15]

However, mesoscale cortical imaging studies have thus far been done exclusively in head-fixed animals. Even relatively simple behavioral assays in head-fixed animals require significant time for acclimatization and training.[16,17] To overcome some limitations of head-fixation, immersive virtual reality environments,[18] voluntarily head-fixation of mice in their home cages,[19] and a moveable head-restraint apparatus[20] have been used in mesoscale imaging studies. However, the lack of vestibular inputs and disruptions in eye-head movement coupling,[21] and behavioral effects from increased stress[22] can significantly alter neural activity during head-fixation as compared to freely behaving animals.[23]

While several head-mounted, miniaturized imaging devices have been developed for imaging neural activity in freely moving animals,[24–28] these devices are designed to per-

form cellular resolution imaging, and thus have small field of view (FOV), limiting their application to imaging single brain regions. Recently, progress has been in engineering a relatively large head-mounted imaging device for mesoscale imaging in rats.[29] In comparison to rats, mice have a much larger slate of genetic tools.[2,30,31]

Traditional one-photon excitation microscopy presents one-photon of light in the visible spectrum to excite fluorescent molecules. This requires close access to the optical plane desired for imaging due to the short, less-penetrating depth of visible light as it scatters through tissue. In contrast, two-photon excitation microscopy utilizes high-power, localized intensity provided through a femtosecond pulsing laser that fires two photons of energy at a higher wavelength closer to the infrared spectrum. The increased penetrating depth of the higher-wavelength photons can reach fluorophores deeper in tissue compared to one-photon imaging. The localized, lower energy photons also limit photobleaching to the tissue surrounding the focal plane, which allows longitudinal recordings to be conducted with minimal effects.[32] When coupled to rapid axial-scanning and miniaturization, two-photon microscopy can produce high-resolution three-dimensional images of dendritic spines and neuronal projections that are active in small regions of the cortex (FOV <2 micrometers laterally, <10 micrometers axially) during unrestrained behaviors.[26,33]

Miniaturized light field microscopes ('miniscopes') used in head-mounted imaging studies integrate lightweight and mass-producible components, highly sensitive sensors, and optical drivers to collect high-speed, cellular resolution images across a larger FOV (< 1 $mm^2$) compared to two-photon microscopy.[24,25] While still limited to a small FOV, the miniaturization process allows for multi-camera mounting to monitor interactions between brain regions in different areas of the cortex.[28]

With inspiration from both technologies, we have taken advantage of the miniaturization process and made modifications to the traditional light field fluorescence microscope to develop a new imaging device, the "Mesoscope", that is capable of obtaining mesoscale

images across the mouse dorsal cortex. We have used the Mesoscope to successfully record mesoscale cortical activity in freely behaving mice, during social interactions with a companion mouse, and during natural sleep. The large FOV captured by the Mesoscope has the potential to significantly expand investigations of mesoscale cortical dynamics during a vast number of free behaviors.

# Chapter Two

# Mesoscope Mechanical Design

## 2.1 Imaging Design Requirements

Before designing and miniaturizing a fluorescence microscope, chronic and long term optical access has to be granted to the dorsal cortex. Previous technologies developed in the lab allow for chronically implanted morphologically realistic transparent polymer skulls ("See-Shells") on mice for very long ($>$ 300 days) durations of time.[34] Additionally, surgical robotic platforms developed in the lab provide a robust and repeatable method to gain access to the dorsal cortex.[35] To meet the requirements of imaging the dorsal cortex during free behavior, the design specifications were broken down into 4 overarching requirements, which are expanded upon in the sections below.

1. Obtain an imaging area capable of encompassing the entire mouse dorsal cortex ($\sim$45 $mm^2$).

2. Design a device that weighs less than 15% of a mouse's body weight (< 4 g).

3. Obtain a resolution sufficient for mesoscale calcium imaging (< 60 $\mu m$ across the entire field of view (FOV)).

4. Design a device capable of correcting for hemodynamic signals.

## 2.2 See-Shell Implant Modification

To perform mesoscale imaging during free behavior, chronic optical access was provided through skull removal through a craniotomy and See-Shell implantation, which provided $\sim$45 $mm^2$ of the mouse cortex open for imaging. The See-Shell implants were modified from **Figure 2.1a** to **Figure 2.1b** to allow for quick fixation of the Mesoscope to the mouse. This modification moved away from the titanium head plate to restrain the mice so they could engage in free behavior. Magnets on the chronic implant would allow for easy fixation of the Mesoscope and an additional tail in the posterior of the device reduced axial movement of the scope. A set screw was also added to further fix the Mesoscope to the See-Shell implant on the mouse to ensure no motion of the head relative to the implant during vigorous behavior.

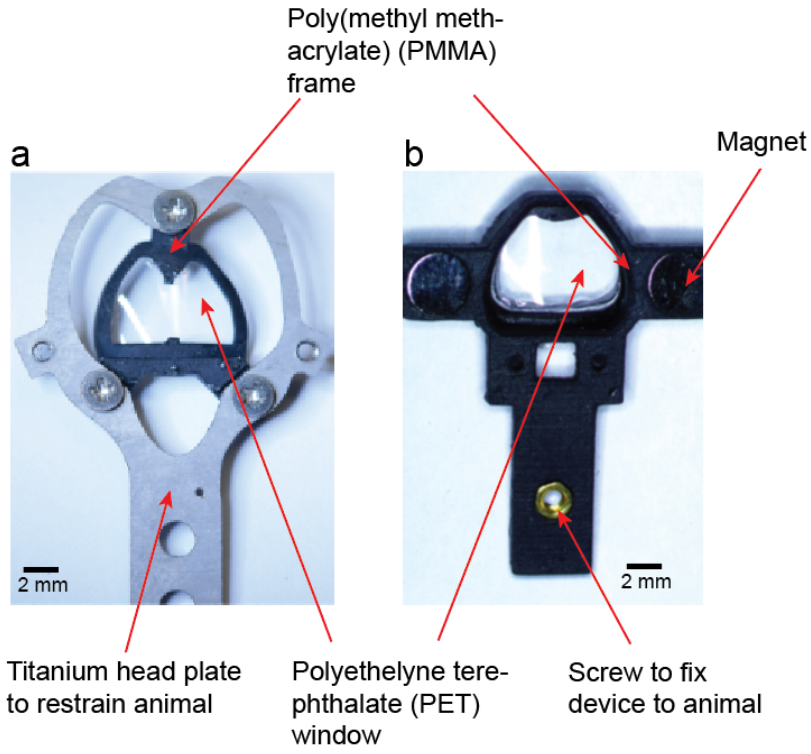


**Figure 2.1 See-Shell Implant Modifications:** **(a)** Photograph of the original See-Shell implant[34] designed for head-fixed experiments. **(b)** Photograph of the modified See-Shell implant with magnetic attachment points to allow for quick fixation of the Mesoscope. The tail end of the See-Shell and additional screw allow rigid fixation of the device to reduce movement artifacts.

## 2.3 Mesoscope Body Design

### 2.3.1 Preliminary Mesoscope Design Iterations

To minimize the impact of the device weight on natural mouse movement, the Mesoscope would have to weigh less than 4.0 $g$ to be within 15% of the mouse's body weight. To begin the iterative design process, it was important to note the fixed weight components of the Mesoscope. The Mesoscope utilizes the Miniscope imaging architecture[25] with a complementary metal–oxide–semiconductor (CMOS) sensor that captures a total area of 752 x 480 pixels. To maximize the resolvable area visible with this CMOS sensor, a single

bi-convex collector lens was utilized so that the focal plane was centered around the surface of the dorsal cortex. Additionally, the transgenic mice utilized for these experiments (Thy1-GCaMP6f mice) contain genetically encoded calcium indicators that require blue excitation light filtered at a wavelength between 460-480 $nm$ for activation. Thus, a minimum of 1 excitation filter would be required for the blue illumination light emitting diode (LED). To capture the GCaMP6f emission signal onto the CMOS sensor during neural activity, a minimum of 1 emission filter, bandpass filtered between 500-550 $nm$, is required. The weight of the fixed components is denoted in **Table 2.1**. Adding up the relevant components yields a mass of approximately 1.88 $g$, leaving 2.11 $g$ allocated for the Mesoscope body housing. In addition to being light-weight, the Mesoscope housing has to be machined to high-precision to fit the small features from the lens and filters placed in it. A high-precision stereolithography 3D printer (Form 2-3, Formlabs Inc.) was therefore utilized to prototype and print the fine features of the first Mesoscope iterations that were generated using a computer aided design (CAD) program (SolidWorks, Dassault Inc.).

| **Component** | **Weight (g)** |
|---|---|
| CMOS Sensor | 1.7645 |
| Bi-convex Collector Lens | 0.0684 |
| Excitation Filter | 0.0225 |
| Emission Filter | 0.0344 |
| *Total Fixed Weight* | 1.8898 |

**Table 2.1** Fixed Mesoscope component weights considered in design optimization.

A focusing mechanism on the Mesoscope was required to set the focal plane to the surface of the dorsal cortex. This was incorporated into the Mesoscope in the first design iteration completed by the lab (prior to this work), where the Mesoscope was separated

into a top and bottom housing shown in **Figure 2.2**. The CMOS sensor was fixed onto the top housing with 3 small screws. On the bottom housing, one blue excitation LED was incorporated into the design to illuminate the cortex. The LED was fixed onto the bottom housing with a custom-made 3D printed "Filter Cube" that contains the excitation filter to bandpass the blue LED to the peak absorption of GCaMP6f. Note that this preliminary design has a very coarse focusing mechanism (a simple click to different focus notches) and was made such that once focused, the top and bottom housing would be glued together to prevent axial motion artifacts.

Preliminary testing conducted noted that the illumination across the FOV with one excitation LED was insufficient to uniformly illuminate the whole FOV. Therefore, a second iteration of the Mesoscope was designed by adding an additional illumination arm in parallel with the first one. Additionally, the set screw tabs from the initial design required anesthetizing the mouse for prolonged durations (> 10 $s$) to secure the Mesoscope to the implant prior to imaging. To alleviate these issues, the set screw fasteners were replaced with magnets for quick attachment to the See-Shell implants. This design iteration is shown in **Figure 2.3**.

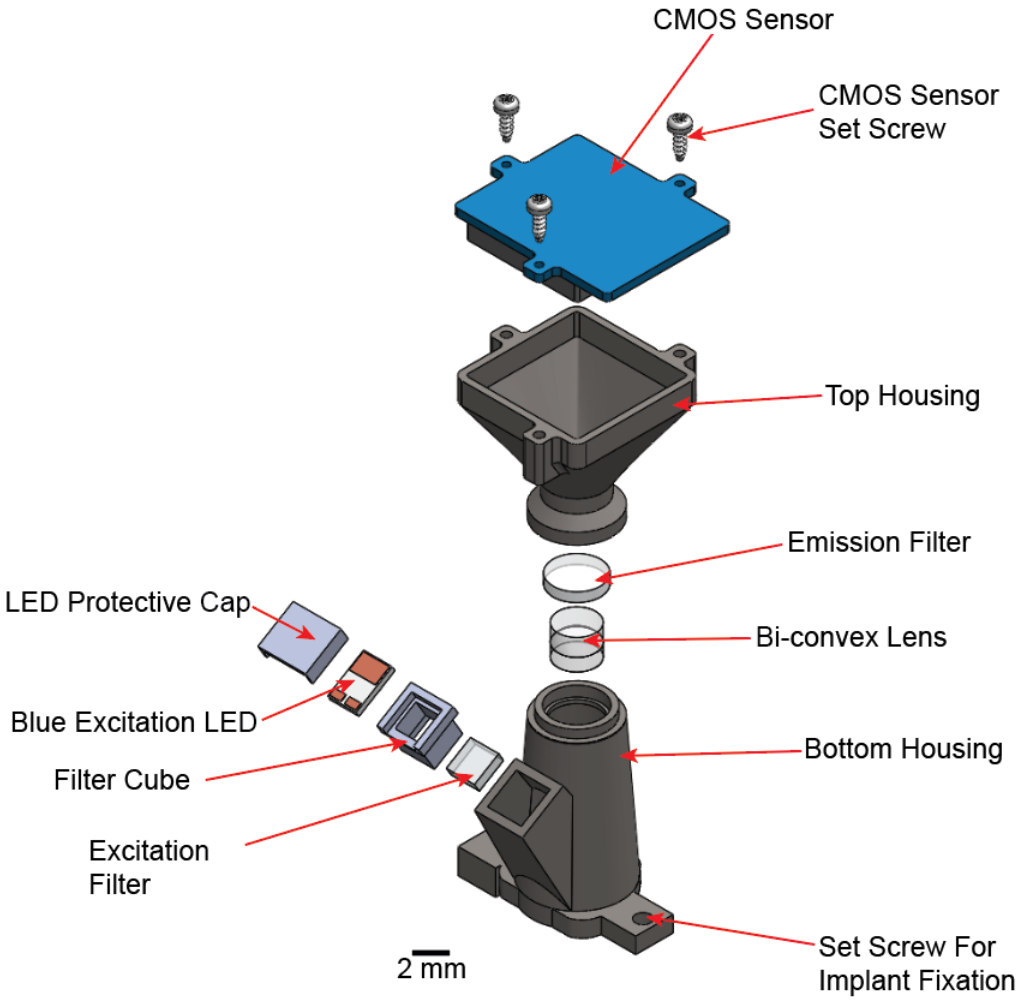


**Figure 2.2 Preliminary Mesoscope Design Iteration:** CAD rendering of the Mesoscope with the minimum relevant optics required for fluorescence imaging. The device is attached to the See-Shell implant via set screws. One blue LED is attached to a filter holder that has a 480 $nm$ excitation filter to excite GCaMP6f in the cortex. Resulting emission signals ($\sim$520 $nm$) are focused through a collector lens and passed through an emission filter onto a CMOS sensor that can be manually focused.

### 2.3.2 Further Mesoscope Iterations

While the first design iterations of the Mesoscope met the weight requirements, further refinements to the illumination across the FOV (see **section 3.3.1**), focusing mechanism (see **section 3.2.1**), hemodynamic correction hardware (see **section 3.3.2**), and motion

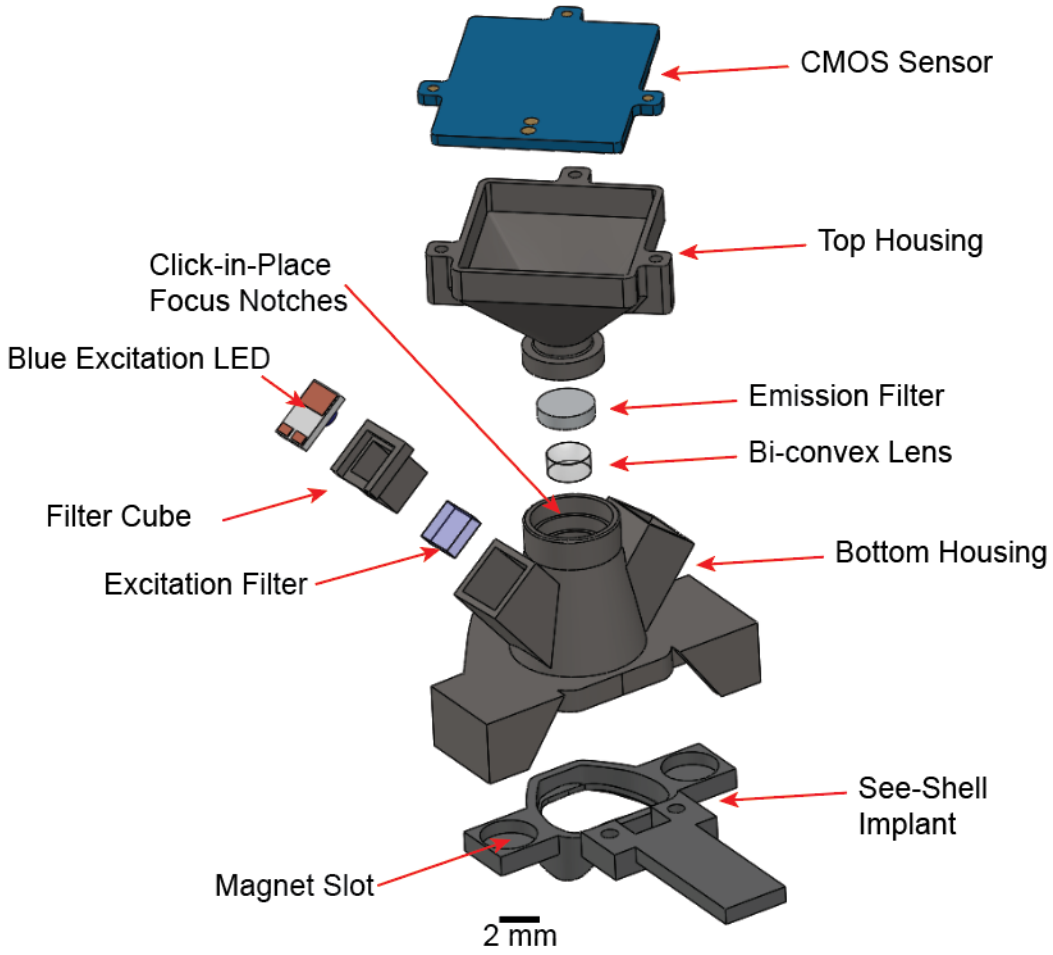


**Figure 2.3 Magnetic Interlocking Mesoscope Design Iteration:** CAD rendering of the Mesoscope with two blue LEDs attached to a filter holder that has a 480 $nm$ excitation filter to excite GCaMP6f in the cortex. Resulting emission signals ($\sim$520 $nm$) are focused through a collector lens and passed through an emission filter onto a CMOS sensor that can be manually focused. The Mesoscope contains magnetic interlocking mechanisms to attach to the implanted See-Shells.

artifact reduction (see **Figure 2.1b**) were implemented and are described in more detail in their respective sections. The final Mesoscope design containing the aforementioned optimizations includes disk magnets that were embedded in the two lateral tabs to align with disk magnets on the bottom of the See-Shell implants, comprising a quick fitting mechanism. A short sleeve surrounding the Mesoscope base and the posterior tab in the

bottom housing serve to kinematically constrain the Mesoscope once mounted on the See-Shell. The tab at the back of the See-Shell frame assists with temporary and gentle restraint of the mouse during removal of the protective cap and attachment of the Mesoscope. The entire process typically takes less than 5 $s$ and can be done without anesthetizing the mouse. For further stabilization, a fastening nut was embedded in the posterior tab of the See-Shell. An 0-80 screw is used to further secure the Mesoscope and minimize lateral motion.

The Mesoscope consists of two interlocking computer numerical control (CNC) machined Delrin housings. Three blue (480 $nm$) LEDs paired with an excitation filter are installed into three illumination arms in the bottom housing. An additional green LED provides illumination for reflectance measurements. A bi-convex collector lens and emission filter are embedded in a central shaft of the bottom housing. A CMOS imaging sensor is mounted on the top housing, which is designed to slide along the central square shaft of the bottom housing for focus adjustments. The CMOS sensor connects to a data acquisition (DAQ) board and is adapted from the open-source Miniscope system.[24,25] The three blue LEDs are wired in series and wires to power the green and three blue LEDs are routed through a commutator to alleviate torsional strain on the device when deployed on freely moving mice. Additional wire management slots were added to the top housing to provide further strain relief during mouse behavior.

The overall weight of the device is 3.8 $g$ and a CAD model of the components is shown in **Figure 2.4a**. Additional blue and green LED illumination paths are shown in the sagittal (**Figure 2.4b**) and coronal (**Figure 2.4c**) views. While the Mesoscope is heavier than miniaturized microscopes with small FOVs,[24,25] it has comparable weight to devices developed for volumetric imaging.[27] Based on CAD simulations, we estimate that the overall center of gravity is $\sim$24.7 $mm$ above the mouse head. While shorter focal length optics could be used to reduce the length of the device, we found that, given the curvature of the cortex, lenses with shorter focal lengths result in optical distortion. Detailed instructions

for assembling the Mesoscope are described in **Appendix A**. CAD files for component fabrication and a bill of materials is provided in **Supplementary Files 1**. Front and side views of the physical device are shown in **Figure 2.5**.

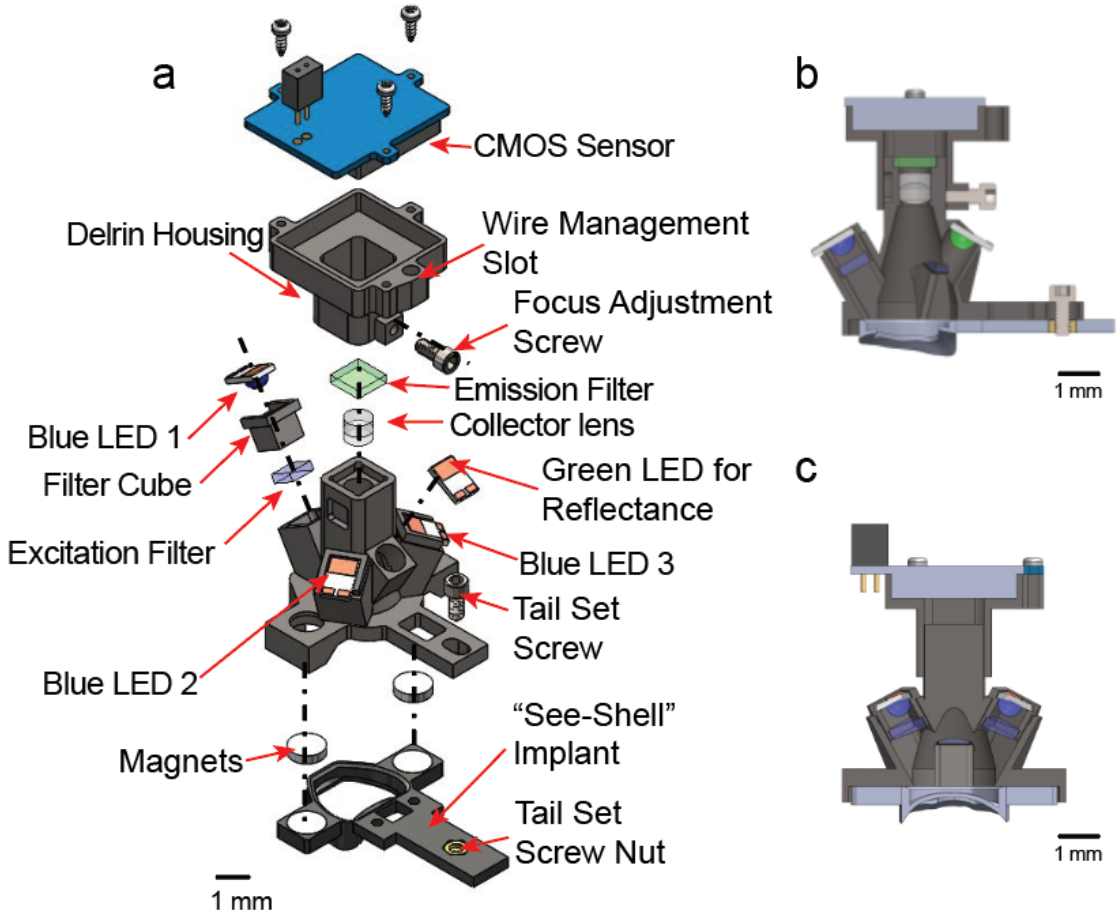


**Figure 2.4 Final Mesoscope Design Iteration:** **(a)** CAD rendering of the final Mesoscope design utilized for data collection, including optimizations to resolution, illumination, hemodynamic correction, weight reduction, wire management, and rigid fixation. **(b)** Sagittal view of the Mesoscope to show the illumination paths of the blue excitation LEDs and green hemodynamic correction LED. **(c)** Coronal view of the Mesoscope to show the illumination paths of the blue excitation LEDs.

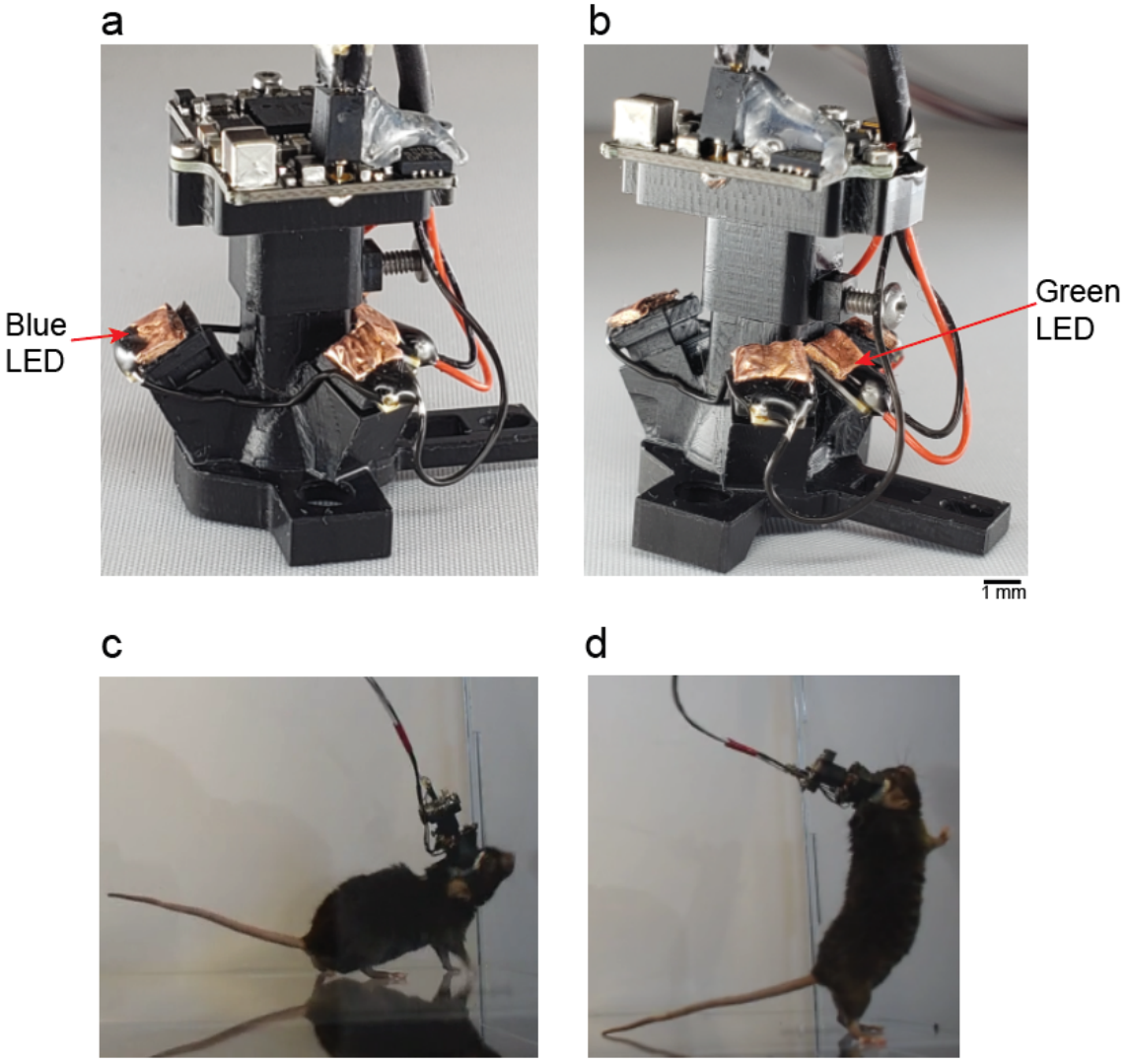


**Figure 2.5 CNC Machined Mesoscope:** **(a)** Side view of the final machined Mesoscope including optimizations to resolution, illumination, hemodynamic correction, weight reduction, wire management, and rigid fixation. **(b)** Rear view of the final machined Mesoscope prototype with 3 excitation blue LEDs and one reflectance green LED. **(c)** Still image of a mouse bearing the Mesoscope from (a-b) and freely behaving. The mouse is engaging in natural behaviors such as walking. **(d)** Still image of a mouse bearing the Mesoscope from (a-b) and freely behaving. The mouse is engaging in natural behaviors such as rearing.

# Chapter Three

# Mesoscope Optical System Design

## 3.1 Optical Design Requirements

To meet the minimum requirements for fluorescence imaging, the Mesoscope would need to be capable of performing imaging across the mouse dorsal cortex with sufficient resolution. Given the fixed weight constraints imposed by the most basic optics required, this resolution would have to be attainable with a single bi-convex lens attached to the Mesoscope with a focusing mechanism design. Additionally, to illuminate the cortex with sufficient power, the excitation LED power has to be well within previously established literature.[29] Hemodynamic signals taken with a reflectance LED should capture signals from a large portion of the cortex as well. The design iterations for these given constraints are expanded upon in the sections below.

## 3.2 Resolution System Design

To meet the resolution design criteria required for mesoscale imaging across the cortex, the Mesoscope needs to image the FOV with a resolution of less than 60 $\mu m$. To achieve this, several design iterations were conducted to design different focusing methods. The

first iteration began as a notch design (see **Figure 2.2**) whereby the top housing would click-in-place to the bottom housing with a series of small notches imprinted on the design. This design was further modified by changing the length of the bottom housing focusing arm to alter the distance between the lens and CMOS sensor, thus altering the magnification of the resolvable FOV. Once focused on one mouse, the top and bottom housings would be glued together with epoxy. While this design worked well for individual mice, we wanted to have a design that could be moved between different mice. To achieve this, we would need a device with a focusing arm that could be adjusted between each trial and mouse so we could achieve the optimal focus across the cortex in all mice. Resolution tests were conducted by viewing the 1951 USAF resolution test target through different Mesoscope designs to determine the minimum resolvable feature when the scope was in focus. This feature was defined as the smallest resolvable white gap between lines that was visible under the desired optical system. The resolution was calculated using the formula shown in **Equation 3.1**, where R is the resolution in micrometers, E is the element number and G is the group number.

$$R = \frac{\frac{32000}{2^{6+G}}}{2^{\frac{E-1}{6}}} \tag{3.1}$$

### 3.2.1 Focusing Mechanism Design

With the depth of focus given by the current bi-convex collector lens ($\sim$100 $\mu m$), we determined the Mesoscope would require a short, axial focusing arm to achieve a sharp and resolved image on the cortical surface. Addressing the limitations of the first prototype (see **Figure 2.3**), we designed a guide rail on the top housing that translates axially as a set screw is turned to achieve fine focus. The CAD model for the design is shown in **Figure 3.1**. We placed the USAF test target onto a test See-Shell implant and viewed it under the

Mesoscope. A representative resolution test target image from the first imaging sessions conducted with this design test is shown in **Figure 3.2**. Focused at the center of the FOV, the smallest resolvable feature observable yields a resolution of 63 $\mu m$ and decreases laterally and vertically across the FOV. This design therefore did not meet the resolution criteria desired for mesoscale imaging as the sharpest in-focus image collected with the focusing arm design was not sufficiently resolved. We therefore decided to tune the coarse-focus design so that the fine-focusing mechanism could yield more desirable results.

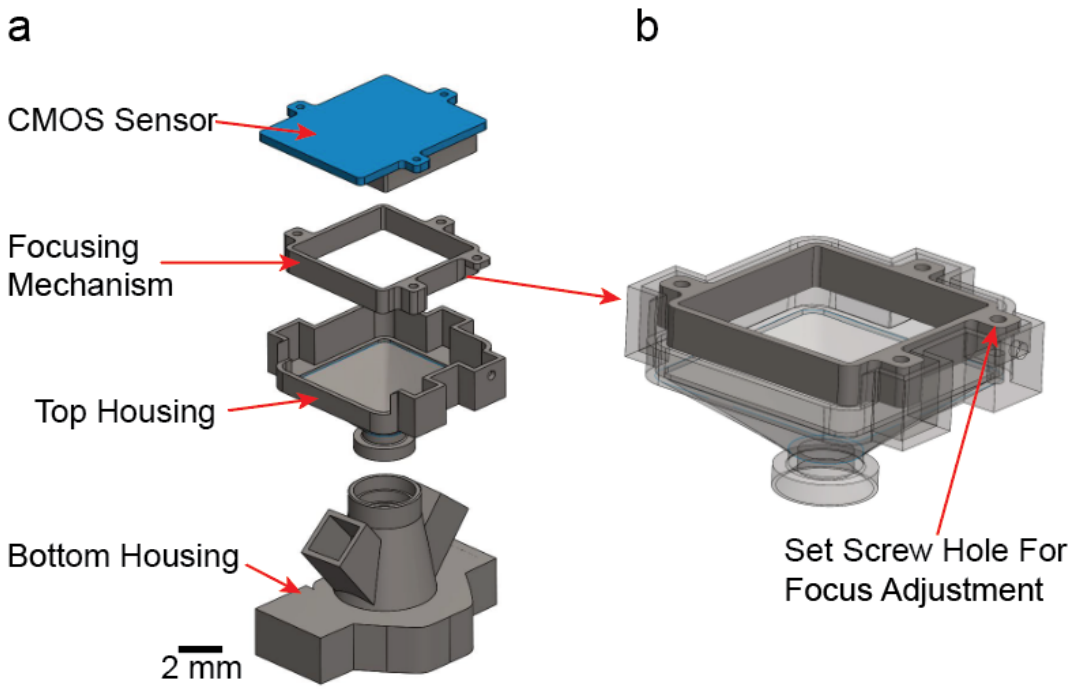


**Figure 3.1 Fine-Focus Mesoscope Design:** **(a)** CAD rendering of the fine-focus mechanism for the top housing of the Mesoscope. The walls were modified in the top housing to incorporate an additional thickness that can be altered for small changes between the CMOS sensor and the FOV. **(b)** Close-up schematic of the focus mechanism in (a). A set screw is tapped into the 3D printed focusing mechanism that moves in the z-direction as the screw is turned, allowing for small changes in focus.

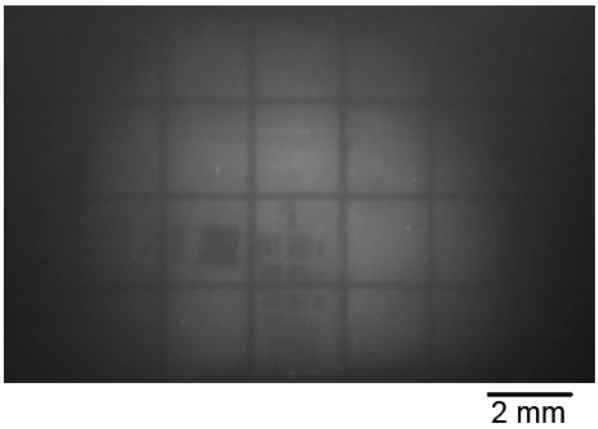


**Figure 3.2 Fine-Focus Mesoscope Design Resolution Testing:** Representative resolution test image of the USAF 1951 test target viewed through the Mesoscope with the fine-focus mechanism (see **Figure 3.1**). The Mesoscope is focused on the center of the FOV and the smallest resolvable feature visible in this test is approximately 63 $\mu m$ at the finest point of focus, with decreased resolution as you travel laterally or axially in the FOV.

Given the small range of the depth of focus, the focusing arm would have to be near the focal plane so we could tune fine-focus parameters with the set screw focusing mechanism. We conducted a series of experiments where we altered the distance between the lens and the CMOS sensor by changing the length of the bottom housing focusing shaft by introducing more notches for the top housing to be pressed into (**Figure 3.3**). Similar to previous resolution test target methods, the Mesoscope was focused at the center of the FOV and the USAF test target was moved across different areas in the FOV. Two representative images of this experiment are shown in **Figure 3.4**. While the resolution was sufficient near the midline of the FOV, we noticed that due to the curvature of the implant (which is morphologically realistic to the mouse brain), we see decreased resolution near the medio-lateral sections of the FOV, which were just below the resolution criteria desired (>35 $\mu m$ near the centroid of the FOV and >55 $\mu m$ approaching the edges of the FOV). Additionally, once the top housing was fit into a particular notch, the part would have to be broken to

separate the top and bottom housings repeatedly, and may not be desirable if the Mesoscope was to be used across a cohort of mice where the distance between the implant and the brain surface is variable.

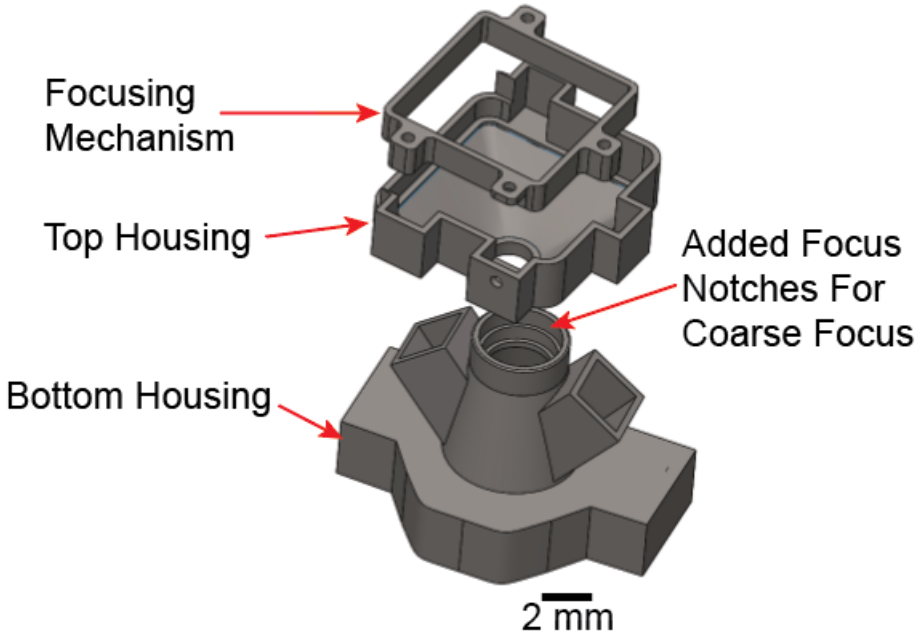


**Figure 3.3 Coarse-Focus Mesoscope Design:** CAD rendering of the coarse-focus mechanism for the Mesoscope with an increased number of notches that the top housing can fit and lock into, effectively changing the achievable focal length.

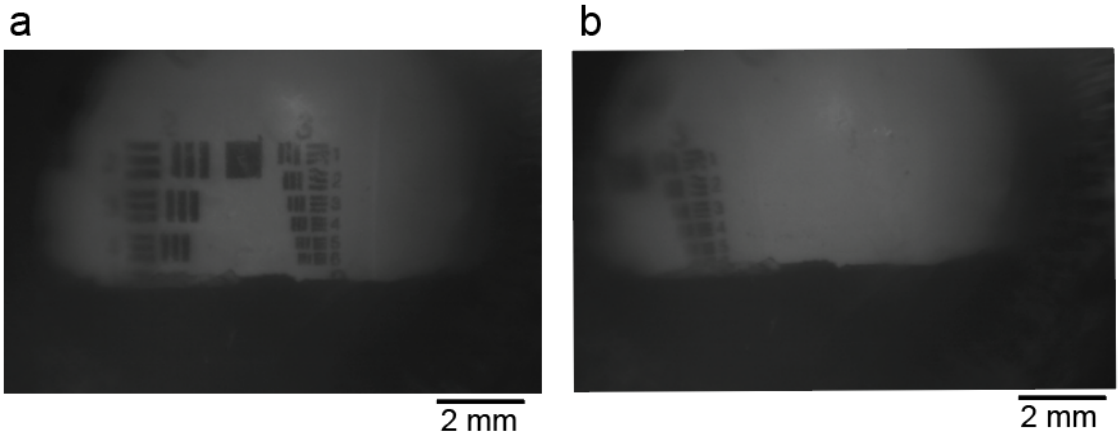


**Figure 3.4 Coarse-Focus Mesoscope Design Resolution Test: (a)** Representative resolution test image of the USAF 1951 test target viewed through the Mesoscope with the coarse-focus mechanism (see **Figure 3.3**). The Mesoscope is focused on the center of the FOV and the smallest resolvable feature visible in this test is approximately 35 $\mu m$ at the finest point of focus, with decreased resolution laterally and vertically in the FOV. **(b)** USAF 1951 test target placed laterally in the FOV and viewed through the Mesoscope with the coarse-focus mechanism (see **Figure 3.3**). The Mesoscope is focused on the center of the FOV and the smallest resolvable feature visible in this test is approximately 60 $\mu m$ at the finest point of focus.

To mitigate this issue, the top and bottom housings of the Mesoscope moved away from a notch design for the coarse-focusing mechanism and towards a sliding mechanism where the top housing slides over the bottom housing until a desired focus is attained and a set screw locks the current focal plane in place. The design for the bottom housing was altered so that the focus arm was rectangular instead of circular as well so that the focus set screw could have friction at a perpendicular angle to the arm and prevent sliding of the arm when the top and bottom housings are fixed to each other. This design is shown in **Figure 3.5** and is modular so that the top and bottom housings can include a wider range of focus across different focal planes and do not need to be epoxied together. Note that an additional LED illumination arm was also added and is described in more depth in **Section 3.3.1**.

Qualitatively, attaching the Mesoscope to a transparent polymer skull allowed us to achieve a high optical resolution across the whole FOV compared to imaging the cortex through the intact skull. Vasculature at the surface of the brain was clearly visible. To measure the resolution, we imaged a 1951 USAF resolution test target positioned at 8 different locations across the FOV. A representative image captured with group 3 of the test target located $\sim$-5.5 $mm$ anteroposterior (AP), $\sim$0 $mm$ mediolateral (ML) is shown in **Figure 3.6a**. Lines in group 3, element 6 are clearly visible, indicating a resolution of 39.36 $\mu m$ at this location. Since a single biconvex lens was used to image a convex surface, not all areas of the cortex are in focus and the optical resolution varied. In all experiments, the top housing was adjusted to obtain the best focus at $\sim$1 $mm$ lateral to the midline. At this focus setting, the resolution ranged from 39 $\mu m$ along the midline to 55.6 $\mu m$ more laterally (**Figure 3.6b**). Since our goal was to observe mesoscale calcium activity, we found these resolutions to be sufficient and the next design iteration with illumination could be worked on.

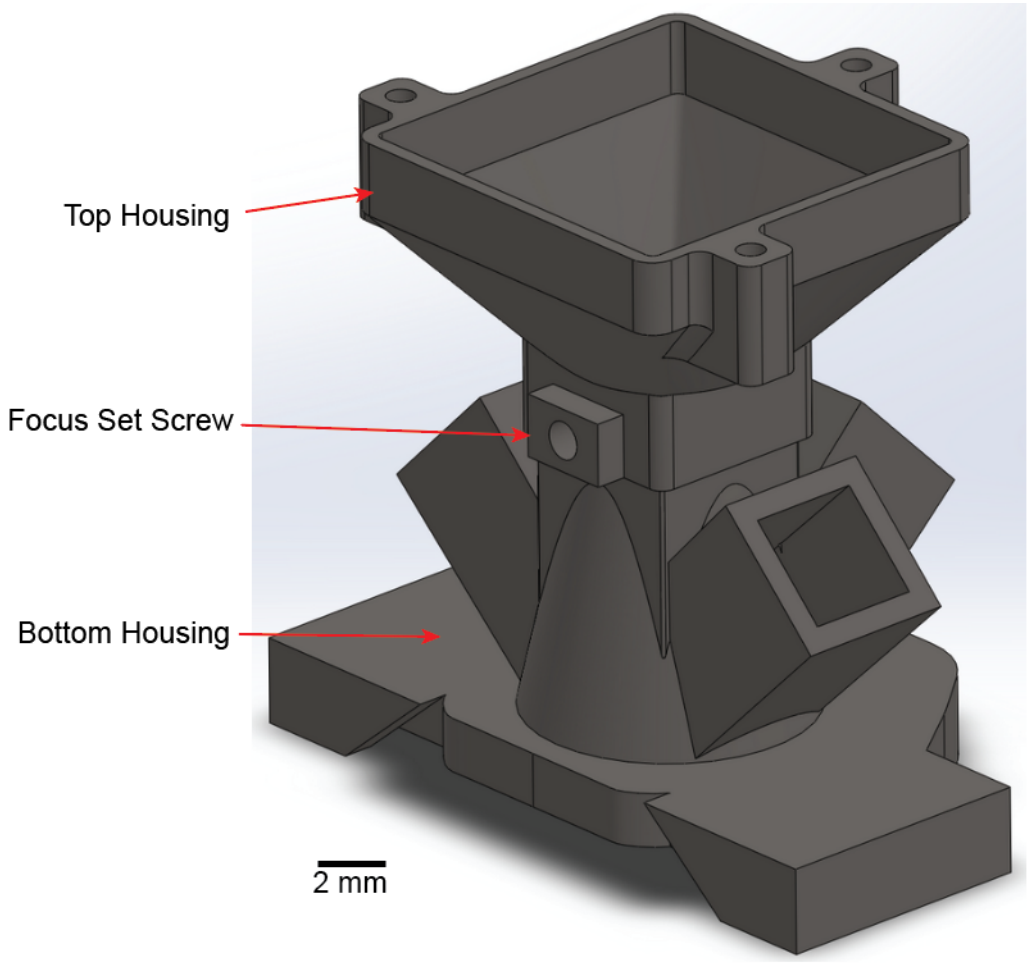


**Figure 3.5 Sliding Focus Mesoscope Design:** CAD rendering of the sliding focus mechanism on the Mesoscope where the top housing slides onto the bottom housing and a focal length can be set by tightening a set screw on the side of the top housing.

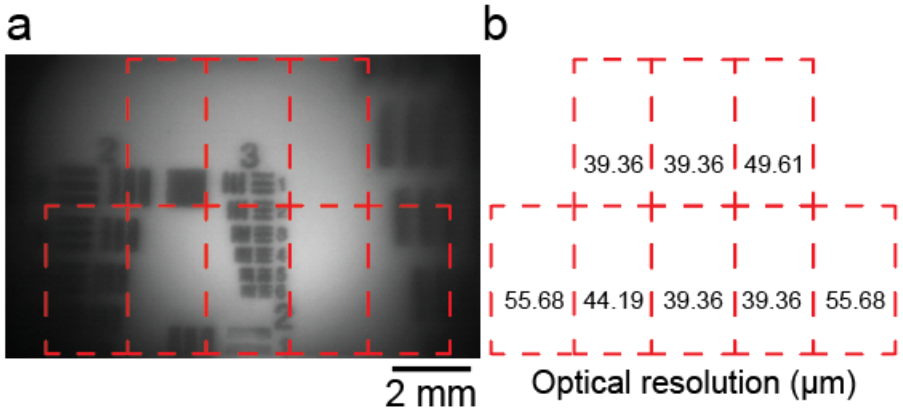


**Figure 3.6 Final Resolution Test:** **(a)** Representative image of the USAF 1951 test target viewed through the Mesoscope that is focused at the center of the FOV. The test target was moved to 8 different locations indicated by the red dashed rectangles and the resolution was calculated at each of these grids. **(b)** Optical resolution test results from the grid locations marked in (a).

## 3.3 Illumination System Design

Imaging the entire dorsal cortex requires uniform illumination across the FOV. The GCaMP6f fluorescent indicators require blue light for excitation, and their emission signal response is proportional to the excitation light power provided to them. As such, it is important to get uniform illumination across the entire FOV to ensure that fluorescence can be captured across the cortex. To measure the uniformity of illumination, 3% agar gel consisting of 10% concentration fluorescein dye (F2456, Sigma Aldrich Inc.) was prepared. A custom 3D printed acrylic container was filled with fluorescein dye infused agar gel phantom and the See-Shell implant was placed on the container such that the entire bottom surface of the See-Shell was coated uniformly with fluorescent gel phantom (**Figure 3.7**). The Mesoscope was attached to the See-Shell using the magnetic interlocking mechanism. Single images where acquired using the Mesoscope and the current delivered to the LEDs was modulated to ensure no part of the FOV was saturated. The captured

images were analyzed in Matlab (Mathworks, Inc) using custom code. Additionally, *in-vivo* experiments were conducted alongside the agar phantom gel control to view how the illumination design actually performed across the cortex. This process was repeated for different illumination configurations and is described further in detail below.

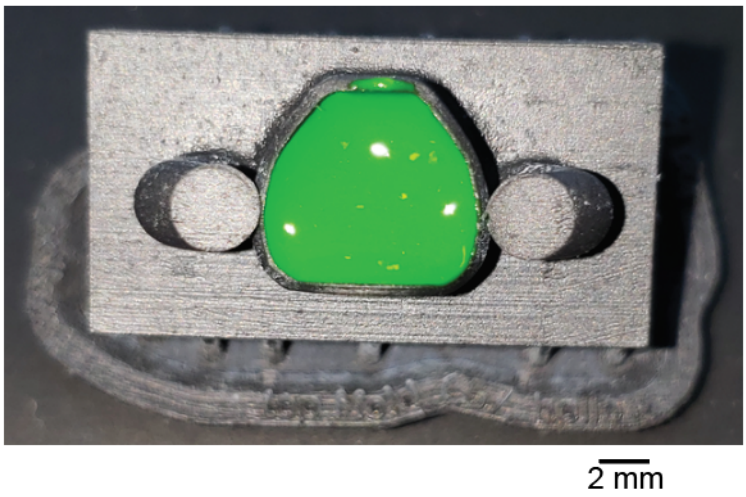


**Figure 3.7 fluorescein Dye Infused Agar Gel Phantom Mold:** 3% agar gel consisting of 10% concentration fluorescein dye that was poured into a custom 3D printed black PMMA container that was an inverse mold to the See-Shell implants. The See-Shell implant was placed on top of the container such that the entire bottom surface of the See-Shell was coated uniformly with fluorescent gel phantom.

### 3.3.1 Excitation LED Illumination Design

As mentioned in **Section 3.2**, pairwise optimization was conducted between resolution testing and illumination. At the end of the resolution testing, a prototype with 3 excitation illumination arms (see **Figure 3.6**) was at a minimum required to achieve greater illumination across the medio-lateral and anterior-posterior edges of the FOV. While under the current weight limitations, an additional design with 4 illumination arms, the most that could fit on the bottom housing, was designed to view the effects of patterning on the illumination

across the FOV. A series of experiments was conducted to view the effects of rotating the angle of the arms across the optical axis ($\phi_i$), which is perpendicular to the optical imaging plane (**Figure 3.8a**), and altering the rotation angle of the arms around the bottom housing ($\Theta_i$), which is in-plane with the optical imaging plane (**Figure 3.8b**) on illumination. Given the symmetry of having 4 illumination arms, we chose to design and 3D print a Mesoscope with $\Theta_i$ rotations at 0 and 45 degrees. Additionally, through preliminary benchtop assembly, we determined that the maximum attainable $\phi_i$ with the current Mesoscope bottom housing design was 70 degrees due to limitations on 3D printability and machining. We therefore printed Mesoscopes with $\phi_i$ rotations about the optical axis at 45, 55, and 65 degrees at each $\Theta_i$ of 0 and 45 degrees. A representative $\Theta_i$ rotation at 0 and 45 degrees and $\phi_i$ rotation at 55 degrees and 65 degrees is shown for each illumination arm in **Figure 3.8c** and **Figure 3.8d**, respectively.

For preliminary testing, a Mesoscope with parallel arms oriented with a $\Theta_i$ angle of 0 degrees and a $\phi_i$ angle of 45 degrees was tested with the fluorescein dye phantom agar. Parallel pairs of LED arms were turned on in the anterior-posterior (**Figure 3.9a**) and medio-lateral (**Figure 3.9c**) orientations and imaged while focused on the fluorescein dye phantom agar. The mean pixel intensity across the FOV was measured across 3 different anterior-posterior locations (**Figure 3.9b,c**). All LEDs were then turned on to show the full illumination capabilities at the given $\Theta_i$ and $\phi_i$ (**Figure 3.9e-f**). In addition to the illumination decreasing drastically at the lateral ends of the FOV, further investigation looking at inhomogenious brain tissue (i.e. non-control phantom agar) was required to ensure the Mesoscope can work *in-vivo* as well as in benchtop testing.

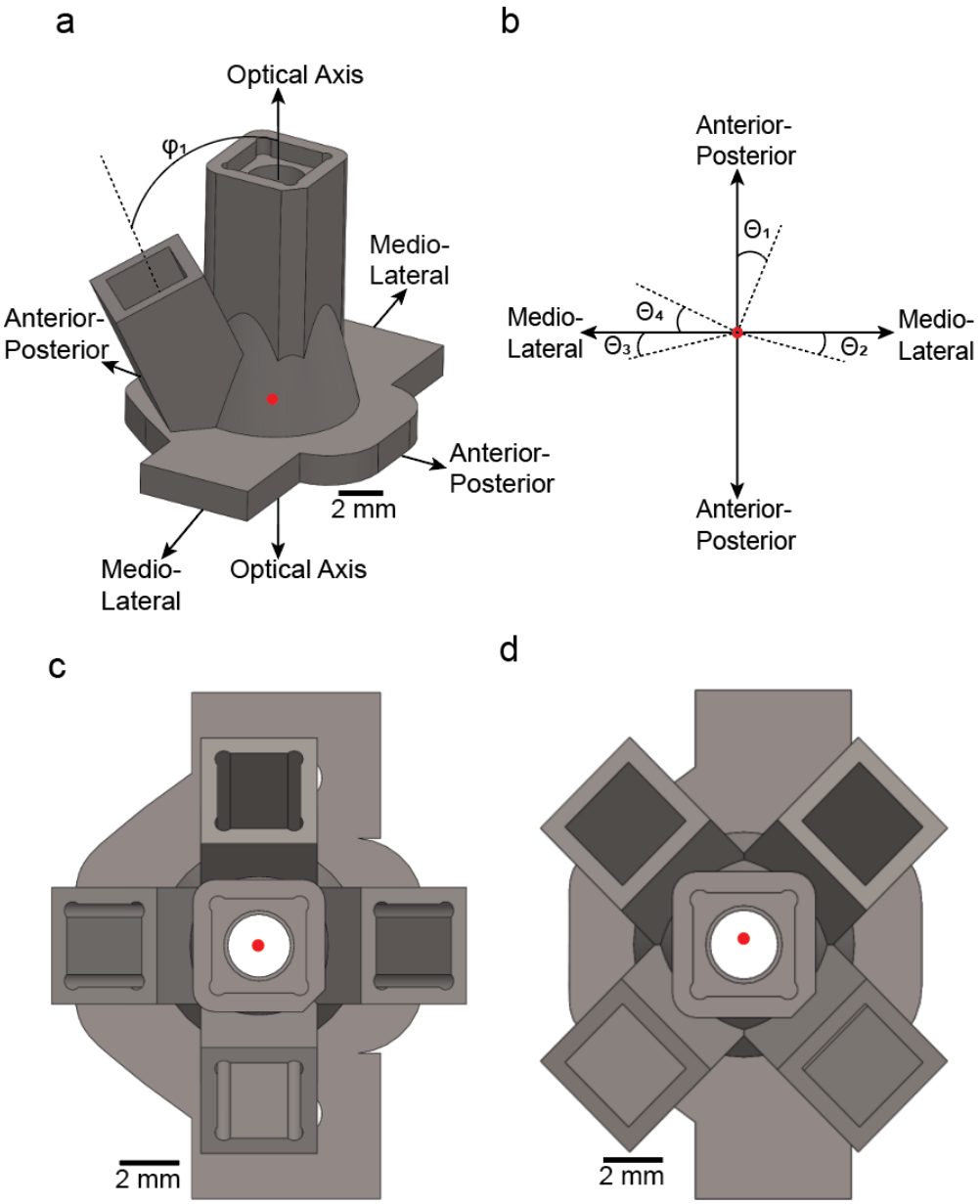


**Figure 3.8 Illumination Design Optimization:** CAD of the illumination designs on the Mesoscope. **(a)** Optical imaging design iterations conducted to improve the uniformity of the illumination across the FOV. The arms were rotated across the optical axis ($\phi_i$) to change the angle of illumination in the cortex and each LED arm can have a separate rotation angle. **(b)** Optical plane view from (a). Each LED arm can be rotated to different orientations around the bottom housing ($\Theta_i$) independently to change the location of the LED illumination in the FOV. **(c)** CAD model with arms $\phi_i$ rotated by 55 degrees and $\theta_i$ rotated by 0 degrees. **(d)** CAD model with arms $\phi_i$ rotated by 65 degrees and $\theta_i$ rotated by 45 degrees

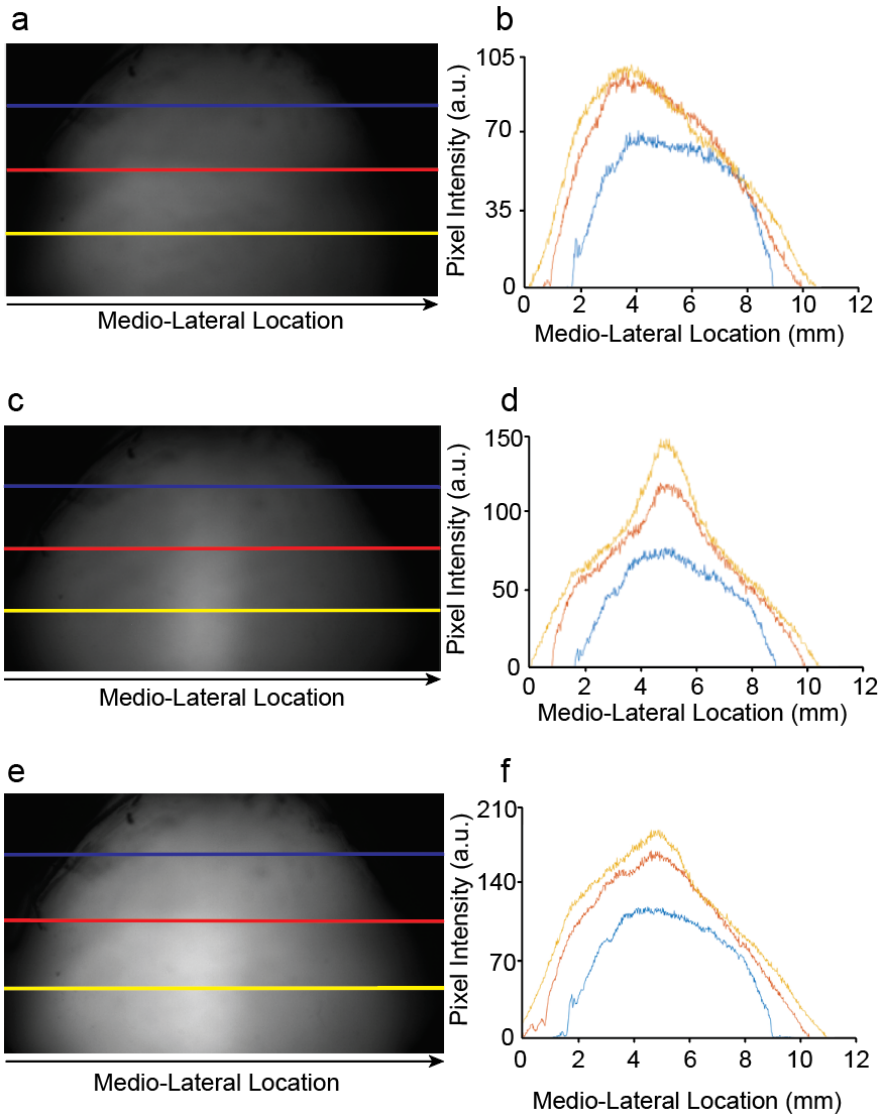


**Figure 3.9 Phantom Agar Illumination Test - Illumination Arm Design Iteration:** A still frame of the illumination pattern across a uniform fluorescein dye infused agar gel phantom captured through the Mesoscope. The pixel intensity across the FOV was calculated at three different areas highlighted by the different colors in each design. **(a)** Two illumination arms along the anterior-posterior axis are turned on and a still frame is captured. **(b)** Corresponding pixel intensity along the colored lines drawn in (a). **(c)** Two illumination arms along the medio-lateral axis are turned on and a still frame is captured. **(d)** Corresponding pixel intensity along the colored lines drawn in (c). **(e)** Two illumination arms along the medio-lateral axis and two illumination arms along the anterior-posterior axis are turned on and a still frame is captured. **(f)** Corresponding pixel intensity along the colored lines drawn in (e).

Each illumination arm was tested alone with a head-fixed GCaMP6f mouse under 2% isoflurane anaesthesia to view the illumination across the FOV *in-vivo* at each orientation. A representative example of this testing with a $\Theta_i$ rotation of 0 degrees and $\phi_i$ rotation of 55 degrees is shown in **Figure 3.10a**, where only one illumination arm along the anterior-posterior axis is turned on. Turning on a different illumination arm along the medio-lateral axis for the same $\Theta_i$ and $\phi_i$ yields the image produced in **Figure 3.10b**. In a different orientation, the arms are $\Theta_i$ rotated at 45 degrees and $\phi_i$ rotated at 55 degrees and the same illumination arm from **Figure 3.10a** is shown in **Figure 3.10c**. Keeping the same $\Theta_i$ angle of 0 degrees and changing the $\phi_i$ angle to 65 degrees is shown in **Figure 3.10d**. As you can see, the effects of both the $\Theta_i$ and $\phi_i$ angles affect illumination across the FOV and a combination of different arms would be required to illuminate the entire cortex.

To further quantify the illumination efficiency of different designs, the mean pixel intensity across the left and right hemispheres of the brain were calculated with different $\phi_i$ angles when $\Theta_i$ is either 0 or 45 degrees and is tabulated in **Table 3.1** and **Table 3.2**. From this information, we can conclude that while having 4 arms provides the most illumination, we can cut off the illumination added by 1 LED arm by patterning the bottom housing with one arm located in medio-lateral direction and rotating the anterior-posterior arms by the same $\Theta_i$. Additionally, while a 65 degree $\phi_i$ rotation about the optical axis provides the brightest illumination for most trials, it does introduce unwanted oversaturation (glare spots) in the FOV for some arm orientations, so there can be a mix of $\phi_i$ rotations for each of the necessary 3 arms.

Combining illumination arms to view their cumulative effect on the illumination of the cortex can be seen in the CAD model in **Figure 3.11a**, and subsequently during *in-vivo* testing (**Figure 3.11b**), where the brightest illumination of the cortex was achieved with one arm located medio-laterally with a $\Theta$ angle of 0 degrees and $\phi$ angle of 65 degrees. The two anterior-posterior arms were rotated with a $\Theta_i$ angle of 30 degrees and a $\phi_i$ angle of 60

degrees.

The Mesoscope's array of three blue LEDs paired with excitation filters delivered a cumulative $\sim$31 $mW$ of power. In an additional control experiment, we imaged fluorescein dye-infused agar gel using the Mesoscope to investigate illumination uniformity (**Figure 3.12a**). To reduce glare while maximizing power delivery to the FOV, the blue LEDs are 9.55 $mm$ from the imaged surface. We observed that the normalized light intensity decreased by 56.1%, 53.3%, and 46.2% compared to the maximum intensity at the ML lines at 1.4 $mm$ AP, -2.8 $mm$ AP, and -4.2 $mm$ AP, respectively (**Figure 3.12b**). The greatest reduction of illumination from the maximum did not exceed 60%. In an additional analysis performed, a heat map was generated to show the illumination intensity spread across the entire FOV (**Figure 3.12c**). These metrics are comparable to the performance of previously developed large FOV scopes,[29] and allowed signals obtained from all pixels to be well within the dynamic range of the CMOS sensor.

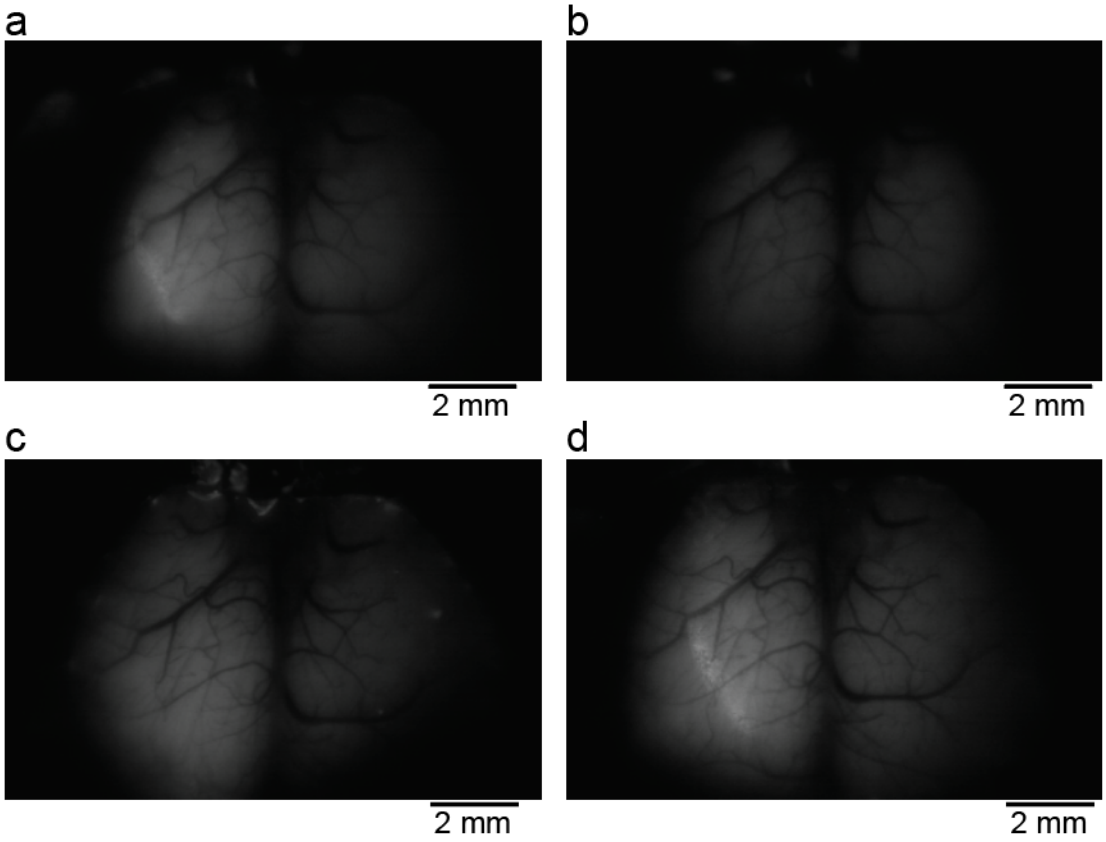


**Figure 3.10 In-Vivo Illumination Arm Testing:** Different combinations of the bottom housing in the Mesoscope are tested to determine the best rotations of the illumination arms about the bottom housing and optical axes (see **Figure 3.8**). Single illumination arm LEDs are switched on to illuminate the cortex of an *in-vivo* GCaMP6f mouse under 2% isoflurane to visualize illumination efficiency across the FOV. **(a)** Still image of the cortex when illumination arm 1 is switched on along the anterior-posterior axis when the $\Theta_i$ angle of rotation is 0 degrees and the $\phi_i$ rotation is 55 degrees. **(b)** Still image of the cortex when illumination arm 2 is switched on along the medio-lateral axis when the $\Theta_i$ angle of rotation is 0 degrees and the $\phi_i$ rotation is 55 degrees. **(c)** Still image of the cortex when illumination arm 1 is switched on along the anterior-posterior axis when the $\Theta_i$ angle of rotation is 45 degrees and the $\phi_i$ rotation is 55 degrees. **(d)** Still image of the cortex when illumination arm 1 is switched on along the anterior-posterior axis when the $\Theta_i$ angle of rotation is 0 degrees and the $\phi_i$ rotation is 65 degrees.

| Angle | Arm Number | Mean Pixel Intensity (a.u.) | |
|---|---|---|---|
| | | Left Hemisphere | Right Hemisphere |
| 45 Degree | 1 | 44.15 | 20.07 |
| | 2 | 28.27 | 22.97 |
| | 3 | 28.66 | 23.87 |
| | 4 | 19.22 | 36.93 |
| 55 Degree | 1 | 53.81 | 25.24 |
| | 2 | 28.83 | 31.48 |
| | 3 | 28.52 | 22.53 |
| | 4 | 22.22 | 39.77 |
| 65 Degree | 1 | 53.91 | 26.94 |
| | 2 | 37.22 | 33.46 |
| | 3 | 38.07 | 34.37 |
| | 4 | 23.26 | 34.71 |

**Table 3.1** Different combinations of the bottom housing in the Mesoscope are tested to determine the best rotations of the illumination arms about optical axis (see **Figure 3.8**) when $\Theta_i$ is fixed at 0 degrees. Single illumination arm LEDs are switched on to illuminate the cortex of an *in-vivo* GCaMP6f mouse under 2% isoflurane to visualize illumination efficiency across the FOV. The mean pixel intensity across the left and right hemispheres of the cortex are calculated for each $\phi_i$ angle.

| Angle | Arm Number | Mean Pixel Intensity (a.u.) | |
|---|---|---|---|
| | | Left Hemisphere | Right Hemisphere |
| 45 Degree | 1 | 35.61 | 14.98 |
| | 2 | 13.48 | 36.22 |
| | 3 | 25.06 | 15.05 |
| | 4 | 17.84 | 22.09 |
| 55 Degree | 1 | 48.88 | 21.01 |
| | 2 | 21.61 | 42.98 |
| | 3 | 33.22 | 22.63 |
| | 4 | 21.46 | 25.95 |
| 65 Degree | 1 | 50.09 | 28.49 |
| | 2 | 39.67 | 66.43 |
| | 3 | 41.91 | 27.84 |
| | 4 | 28.34 | 31.27 |

**Table 3.2** Different combinations of the bottom housing in the Mesoscope are tested to determine the best rotations of the illumination arms about optical axis (see **Figure 3.8**) when $\Theta_i$ is fixed at 45 degrees. Single illumination arm LEDs are switched on to illuminate the cortex of an *in-vivo* GCaMP6f mouse under 2% isoflurane to visualize illumination efficiency across the FOV. The mean pixel intensity across the left and right hemispheres of the cortex are calculated for each $\phi_i$ angle.

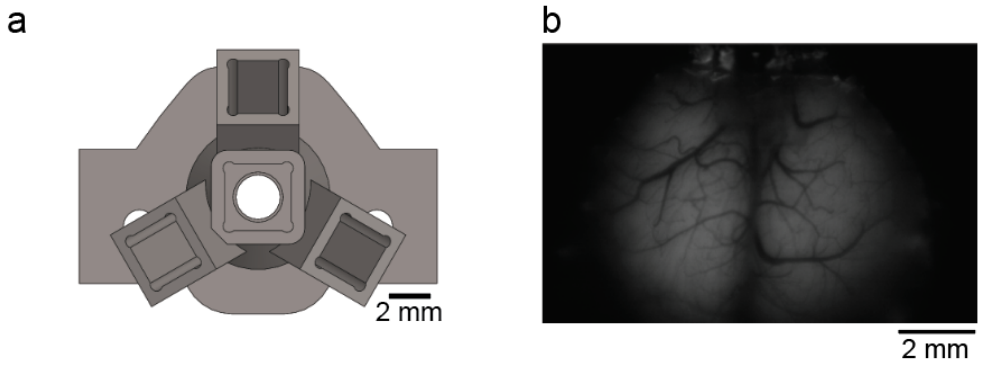


**Figure 3.11 Final Illumination Design For Mesoscope Excitation LEDs - *In-vivo* Testing:** Different combinations of the bottom housing in the Mesoscope are tested to determine the best rotations of the excitation illumination arms about the bottom housing and optical axes (see **Figure 3.8**). **(a)** Computer-aided design (CAD) of the final illumination arm patterning where one arm located medio-laterally was rotated with a $\Theta$ angle of 0 degrees and $\phi$ angle of 65 degrees. The two anterior-posterior arms were rotated with a $\Theta_i$ angle of 30 degrees and a $\phi_i$ angle of 60 degrees. **(b)** Still image of the cortex of an *in-vivo* GCaMP6f mouse under 2% isoflurane anasthesia captured to visualize the illumination efficiency across the FOV when all illumination arm LEDs are switched on.

### 3.3.2 Reflectance LED Illumination Design

In addition to providing excitation light to illuminate the cortex, the Mesoscope would also need to have capabilities to correct for hemodynamics, which are the intrinsic optical signals arising from changes in cortical blood volume that are proportional to neural activity.[36] This can be completed by using single-diffuse green wavelength light at approximately 500-550 $nm$. As light enters the cortex, it will scatter and be absorbed through the various components that make up tissue, with the highest scattering materials to be hemoglobin and water. The changes in the blood flow in the cortex during neural activity lead to different proportions of oxygenated and de-oxygenated hemoglobin, which both interact with light differently. However, around the 500-550 $nm$ band, they have approximately the same scattering coefficient, which means their scattering effects compound and therefore can be accounted with a single-diffuse green light source. Additionally, this wavelength band is

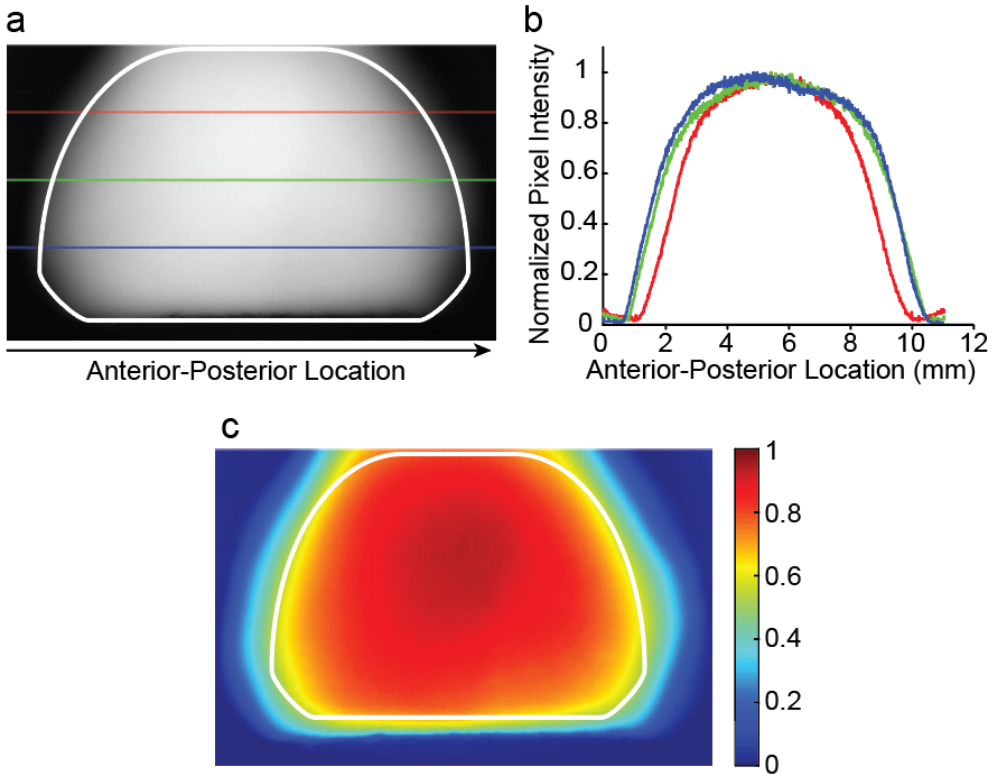


**Figure 3.12 Phantom Agar Illumination Test - Final Illumination Design:** **(a)** Still image of a uniform fluorescein dye gel phantom captured through the Mesoscope with the final illumination design in **Figure 3.11a**. **(b)** Normalized mean pixel intensity of the entire FOV across the colored lines drawn in (a). **(c)** Heat map of the spread of pixel intensities across the imaged FOV. The colorbar indicates normalized pixel intensity.

in the same region as the emission signal from the GCaMP6f, so no additional optics are required aside from adding a reflectance green LED light source to measure these changes in tissue reflectance. Similar to the excitation illumination design, a similar series of *in-vivo* experiments were conducted to optimize the location of the green illumination arm and the optimal rotation around the optical axis to provide sufficient illumination. A preliminary model was developed to incorporate both excitation and reflectance illumination sources in the same illumination arm by incorporating a dichroic mirror such that blue light can pass through it at a perpendicular angle and green light can pass through it at a 45 degree angle

(**Figure 3.13**). This design, however, was too heavy for the weight constraints set previously and the green LED would have to be housed separately from the blue LED sources.

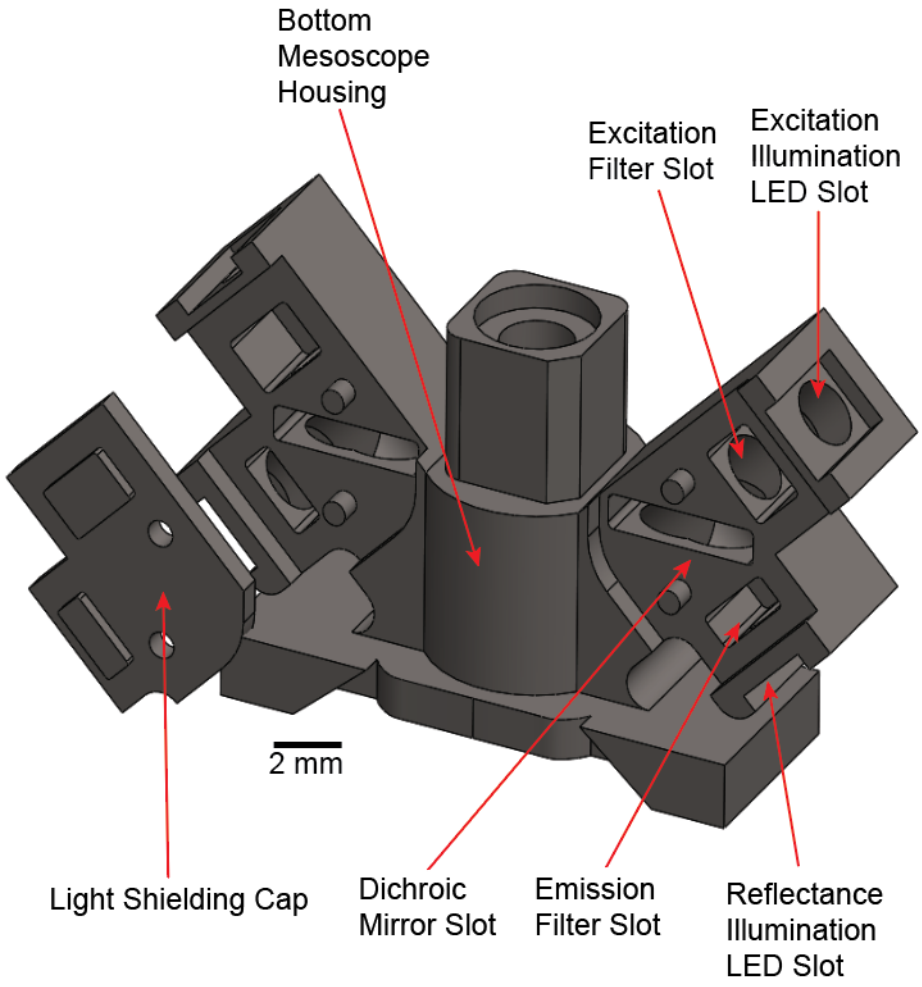


**Figure 3.13 Multiple LED Illumination From One Illumination Arm Model:** CAD rendering of the bottom Mesoscope housing that incorporates both blue excitation and green reflectance light sources required for calcium imaging and hemodynamic response measurements, respectively. The excitation light travels through a dichroic mirror at a 90 degree angle and passes to the FOV. The reflectance light travels through the same dichroic mirror at 45 degrees and is reflected towards the imaging plane to illuminate it with green light. Both emission signals are collected through the same emission filter and lens and onto the CMOS sensor as in previous designs.

Given the weight constraints of the Mesoscope, there would only be sufficient area to either include one macroscopic green LED on an illumination arm (similar to the blue excitation LED arms), or to include several much smaller green LEDs and incorporate them into the Mesocope body without an illumination arm. Beginning with the latter, we designed a bottom housing with slots to attach micro-LEDs to the inside of the bottom housing for reflectance measurements. Given the limitations to 3D printing (and future machining inquiries), we manufactured the smallest slot that could fit micro-LEDs (Kingbright 570nm LEDs, DIGIKEY) into the housing. The CAD model of the bottom housing design is shown in **Figure 3.14a**. Furthering the design, we added extrusions to the LED slots (**Figure 3.14b**) so that the LED could be rotated about the optical axis to maximize illumination of each LED in the FOV. The micro LEDs were very difficult to solder with over-the-counter soldering equipment so a printed circuit board (PCB) was designed to solder wires onto the LED to provide power (**Figure 3.14c-d**). With negligible added weight, the PCB was epoxied to the inside (**Figure 3.14e**) and outside (**Figure 3.14f**) of the bottom housing. While this design did not add significant weight to the Mesoscope, the illumination provided to the design was difficult to distribute towards the FOV as each green LED PCB was too large to fit within the machined slots with precision. Although this design was discontinued moving forwards, we gained valuable knowledge that only small amounts of green light were required to provide reflectance information.

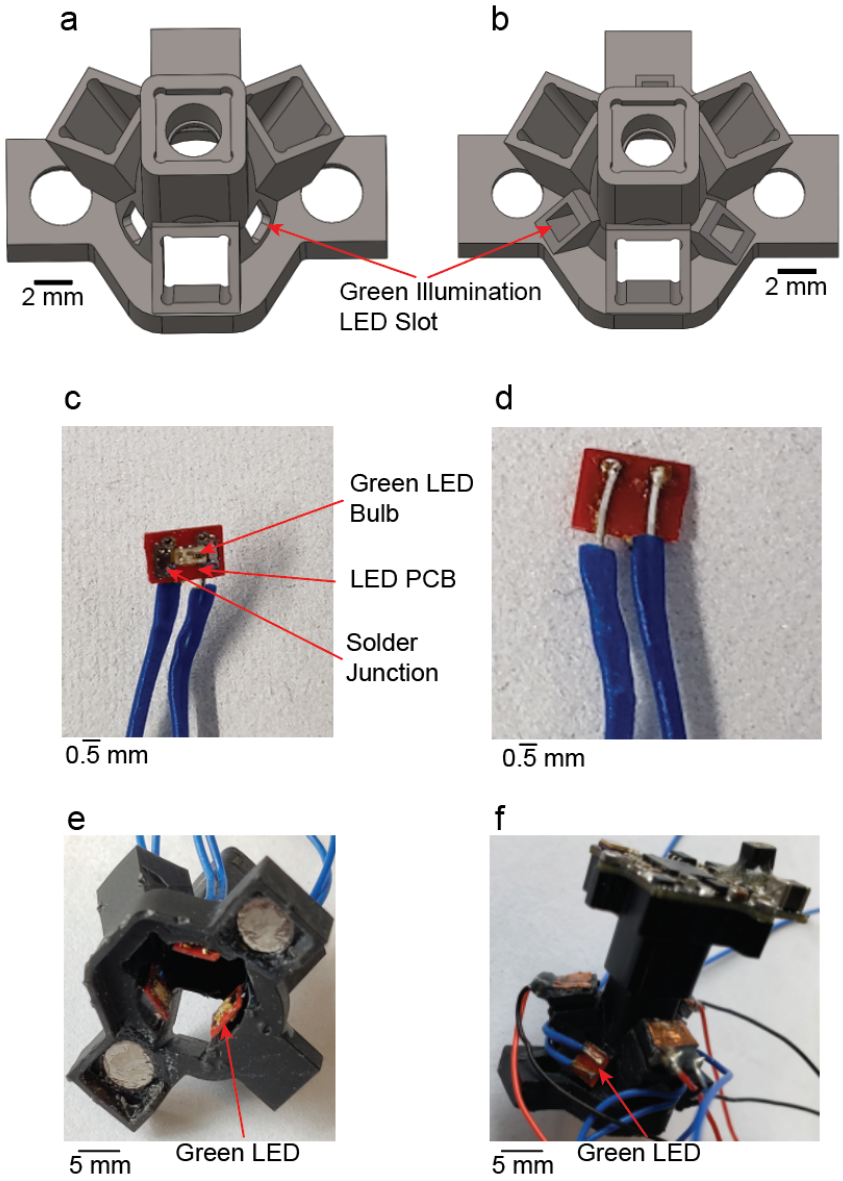


**Figure 3.14 Green Illumination Micro-LED Design:** CAD rendering of the bottom housing of the Mesoscope with a through-hole that can fit a micro-LED mounted to a PCB. **(a)** A model where the LED is housed inside the bottom housing. **(b)** A model where the LED is housed outside the bottom housing. **(c)** Front view of a 500-550 $nm$ green micro-LED soldered to a machined printed circuit board (PCB). **(d)** Rear view of the LED PCB illustrating the soldering junction for 28 gauge wires. **(e)** 3D printed bottom housing where the green LEDs are placed inside the Mesoscope and wires are fed through the through-holes that were machined in (a). **(f)** 3D printed bottom housing where the green LEDs are placed outside the Mesoscope on the illumination LED extrusion in (b).

We designed a Mesoscope bottom housing with only one green illumination source which did not require an excitation filter for reflectance measurements. An extrusion was added to the bottom housing that could hold a macroscopic green LED (**Figure 3.15a**). Similar to optimization for the blue excitation LED arms, we altered the $\phi$ angle of the extrusion about the optical axis (see **Figure 3.8a**) at 50 degrees (**Figure 3.15b**), 55 degrees (**Figure 3.15c**) and 60 degrees (**Figure 3.15d**) to visualize the effects of this rotation on illumination in the FOV. Note that in **Figure 3.15b, d**, there are glare artifacts that appear at these rotation angles. In a short but descriptive experiment, we utilized a spectrometer to measure the reflectance emission of the PET used as the transparent polymer skull in the See-Shell design (see **Figure 2.1**). The PET has a reflectance signal also in the 530-550 $nm$ green emission band, and therefore at certain angles provides the glare artifacts aforementioned. We determined that glare can be significantly reduced by moving the source of light further away from the FOV, but this would require adding additional extrusion material to the LED arm, which impacts the weight design constraint we currently have. We therefore decided that the 55 degree angle was sufficient and necessary to illuminate approximately 70% of the cortex that is illuminated with blue excitation LEDs and provide information used to correct for hemodynamics within the illuminated FOV. The green LED delivered $\sim$0.22 $mW$ of power to investigate reflectance.

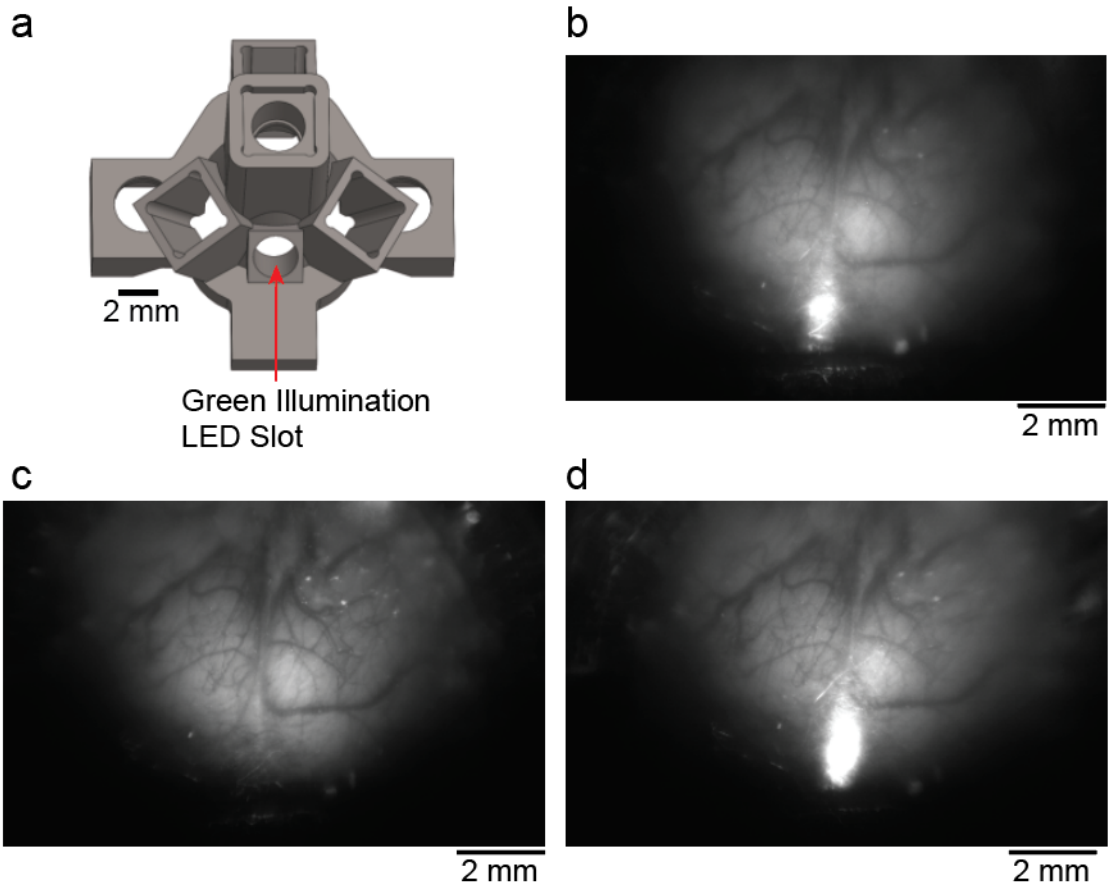


**Figure 3.15 Single Green LED Illumination Design:** Different combinations of the bottom housing in the Mesoscope are tested to determine the best rotations of the emission illumination LED slot about the optical axis (see **Figure 3.8**). The illumination slot LED is switched on to illuminate the cortex and collect reflectance signals of an *in-vivo* GCaMP6f mouse under 2% isoflurane anasthesia to visualize illumination across the FOV. **(a)** Computer-aided design (CAD) rendering of an illumination LED slot that a 500-550 nm green LED can be epoxied to. Similar to the excitation LED slots, the green illumination slot can be revolved about the optical axis via a $\phi$ rotation. **(b)** Still image of the cortex when the reflectance illumination arm is switched with a $\phi$ rotation of 50 degrees. **(c)** Still image of the cortex when the reflectance illumination arm is switched with a $\phi$ rotation of 55 degrees. **(d)** Still image of the cortex when the reflectance illumination arm is switched with a $\phi$ rotation of 60 degrees.

# Chapter Four

# LED Switching Circuit Design

## 4.1 LED Pulsing Circuit Design Requirements

While simultaneously investigating the resolution, weight, and illumination of the Mesoscope, we also focused on power circuit designs to have a fully functioning imaging device. Most conventional microscopes currently utilized for whole-cortex imaging in head-fixed animals utilize high-powered lasers for excitation and reflectance measurements[37] with sophisticated power control methods. A wide range of these power control methods include heat sink designs that mitigate LED power fluctuations and damage to the LED PCB so they can be powered on for long durations of time at powers higher than their rated design specifications. Additionally, the Mesoscope has to collect GCaMP6f signals and reflectance signals from the cortex, and cannot do so simultaneously since there is only one CMOS sensor recording information from both these channels. As such, the LEDs have to be alternatively pulsed to collect both channels of information and this pulsing has to be repeatable and synchronized with the images acquired by the Mesoscope. The LEDs require sufficient power to excite the calcium molecules across the cortex and need to be stable with noise reduction in order to capture the small changes in fluorescent signals. Additionally, the LEDs need to be powered by a fast-speed microsecond switching circuit controlled with

a precisely synchronized microcontroller. Several experiments were conducted to address these design specifications and are highlighted in the sections below.

## 4.2 LED Pulse Dynamics

Given the weight constraints of the Mesoscope, we implented some simple but necessary heat sink methods to each LED to provide them with sufficient cooling for long term use while they are operated at high powers. Each LED has a 3 $mm$ x 2 $mm$ copper heat sink pad to mitigate LED cooling. To maximize heat conduction through the copper, an 80 $mm$ strip of heat sink copper tape was folded 4-5 times to layer it with small pockets of air in-between each fold. This strip was then cut to the dimensions of the heat sink pad (**Supplementary Figure A.1a, left**) and soldered (**Supplementary Figure A.1a, right**) to it to increase the lifespan of each LED. We found that this layered copper was sufficient to power the LEDs for 8-10 minute experiments without any significant residual heating or decrease in their light power. We measured the power of Mesoscope's array of three blue LEDs paired with excitation filters and they delivered a cumulative 28-31 $mW$ of power (at an operating voltage of 9 $V$). The green LED delivered 0.22-0.23 $mW$ of power (at an operating voltage of 6 $V$).

With a stabilized performance over time, we then investigated the repeatability of controlling LED pulses with a microcontroller. Given the fast response of GCaMP6f in the cortex ($\sim$7 Hz firing rate), we would require a microcontroller that can send out pulses at speeds no slower than the Nyquist frequency to capture the emission signals ($\sim$15 Hz) without signal loss. A Teensy 3.5 microcontroller was therefore selected as our microcontroller as it has a processing speed of $\sim$120 MHz and therefore could theoretically perform the microsecond pulsing we require if there are no heavy computations during pulsing. A randomly selected pulse time (100 Hz) was sent to the blue LEDs and their

intensity profile was measured with a photoresistor (**Figure 4.1a**). This was repeated for 130 cycles per trial for 6 total trials. The intensity data was analyzed in Matlab and each set of 130 cycles was averaged and collapsed into a single trial plotted in **Figure 4.1b**. This demonstrates that the microcontroller is capable of sending out repeatable pulses across time with little variation across different experiment times. Similar experiments were conducted with the green LED. Additionally, we derived first-order dynamics of the LEDs during this cyclic testing and determined the blue and green LEDs have time constants (to reach 66.66% peak power) of $1.79 \pm 0.31\ ms$ and $1.97 \pm 0.10\ ms$, respectively. Additionally, we learned that the LEDs have slower shut-down dynamics than turn-on dynamics, and therefore could lead to the potential bleed-over between the blue and green illumination sources.

To further investigate stability and drift of the LEDs, experiments were performed on fluorescein dye infused agar phantom to determine the illumination performance of the LEDs over time when measured with the Mesoscope CMOS sensor. This gives the most representative type of testing we can perform as the agar phantom has similar excitation and emission bands as GCaMP6f does. We conducted imaging sessions typically 3-4 minutes in length to determine if there was any observable drift in LED performance over longer experiment durations using realistic powers we would require for *in-vivo* testing. A simple switching circuit was designed to provide power to each LED source at power specifications greater than the Teensy could provide. An n-doped MOSFET was utilized to act as an open switch at resting state when no pulsing is desired. The Teensy provides a pulse to the MOSFET, which closes the switch and allows power from a power supply to flow through the LEDs to provide illumination (**Figure 4.2a**) that is collected onto the CMOS sensor. The mean fluorescent intensity of the entire FOV was averaged for each frame to generate a time series of intensity data. When operating at full power, the blue LEDs exhibited non-linear behaviors during the initial $\sim$120 seconds of testing (**Figure 4.2b**). We therefore determined that each experiment we conduct moving forward would have to include at least

120 seconds of LED warm-up time to reach a stable imaging point. The green LED does not exhibit the same behavior (**Figure 4.2c**) and instead has a stable intensity profile during illumination.

To address the cross-bleed over effect from the blue LED source into the green source, we noted that the excitation strength of GCaMP6f is proportional to the blue light power provided. As the blue LED source rapidly decays, the amount of GCaMP6f that is excited and can emit a signal also rapidly decays and therefore the signal cross-bleeding effect from the blue channel to the green channel is negligible. The reverse, however, may not be true as the green LED source measures tissue reflectance, which is calcium independent. The decay of the green signal will elicit a proportional reflectance signal from tissue, and we visually confirmed there was potential for cross-bleeding effects from the green to the blue channel. We tuned the pulse durations for each illumination source to minimize the effects of cross-bleeding and determined that at a 30 Hz CMOS sampling rate (15 Hz for each channel), a duty cycle of 30% (20 $ms$ every odd frame that lasts 33.3 $ms$) for blue LEDs and 6% (4 $ms$ every even frame that lasts 33.3 $ms$) for green LEDs resulted in a negligible (0.34%) increase in the mean blue channel intensity when the green illumination source is switched on (**Figure 4.2d**).

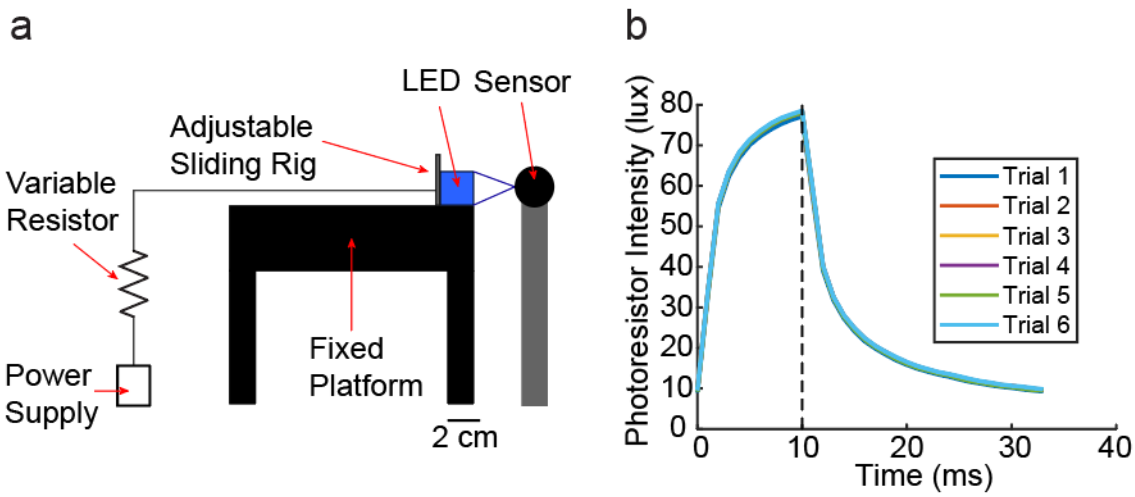


**Figure 4.1 LED Pulse Repeatability:** **(a)** Schematic of a setup used to collect LED illumination pulse dynamics for any source of LED. The sensor can be interchanged between a photoresistor to measure cyclic light intensity or a photodiode to measure absolute light power. The adjustable sliding rig can change the distance to the sensor to mimic light power decreases as the location of the sensor moves away from the source. A power supply and variable resistor are used to tune the LED power as per the desired test. **(b)** Cyclic LED pulse dynamics measured for an arbitrary pulse time of 100 Hz given to the blue LEDs. Their intensity response was measured with a photoresistor across 130 cycles per trial for 6 trials. All 130 cycles were collapsed into a single average pulse per trial and were plotted.

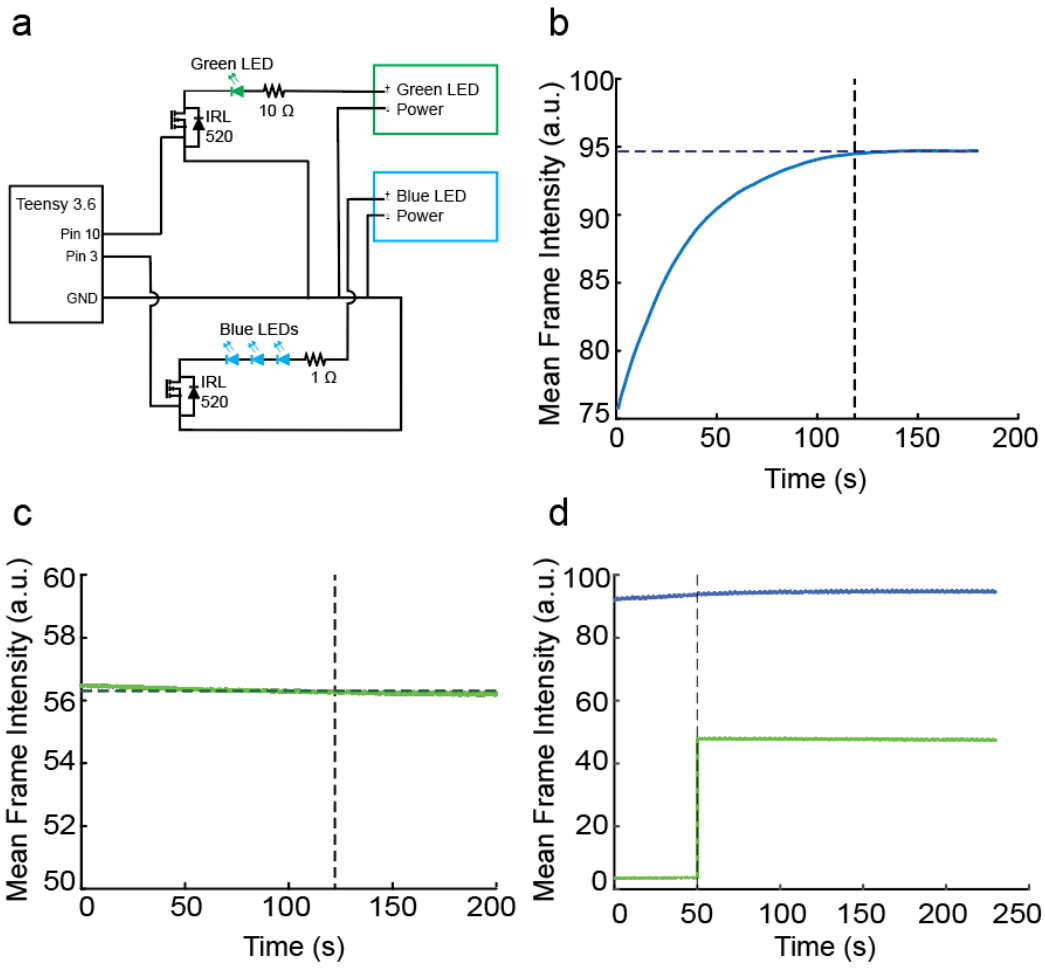


**Figure 4.2 LED Stability:** **(a)** Switching circuit diagram schematic that is used to pulse two LED sources. A microcontroller is utilized to send pulses to two independent MOSFETs connected to the blue and green illumination sources. When triggered, the MOSFET switch closes and power from a separate power supply runs through each LED. The LEDs illuminate a fluorescein dye agar phantom with excitation and emission bands similar to GCaMP6f. The resulting emission signals are collected onto the Mesoscope CMOS sensor. **(b)** Mean frame intensity data captured when blue light is used to excite the agar phantom. The black dashed line indicates an approximate 120 second warm-up period until a stable illumination point is reached, which is shown by the blue dashed line. **(c)** Mean frame intensity data captured when green light is used to collect reflectance data from the agar phantom. The dark green dashed line indicates a stable illumination point. **(d)** Mean frame intensity data captured when both illumination sources are powered. The blue illumination source is powered alone for approximately 50 seconds before the green illumination source is turned on to investigate its effects on the blue channel signals collected.

## 4.3 LED Frame Capture Synchronization

With stable LED dynamics, we then focused on designing a circuit interface to precisely synchronize the LED pulsing with the CMOS sensor frame capture on the Mesoscope. When we utilized the microcontroller as a global clock to synchronize LED pulses, we observed a drift in the frame pacing in some trials that would cause delays in the frame capture, thereby switching the order of the blue and green channel frames. This observation was consistent with previous literature[29] and could be mitigated by adding an experimentally determined delay into the pulse dynamics. However, we found this delay to be dependent on several parameters, such as data transmission speed from the CMOS sensor to the computer, which varied based on how many applications were open on the computer or how long the data transmission cable was. To work around this issue, we used the microcontroller as an external trigger to the Miniscope DAQ to start a recorded video and then synchronized LED pulses with incoming frame captures sent as transistor–transistor logic (TTL) pulses by the Miniscope DAQ. We implemented hardware interrupts into the microcontroller control algorithm to detect a change in the TTL pulse, which indicates a new frame capture. Additionally, the Miniscope software architecture allows for precise behavior camera synchronization with the CMOS sensor and a summary schematic of the data transfer and wiring for the system is shown in **Figure 4.3a**. Every odd frame was assigned to the blue LED illumination source and every even frame was assigned to the green LED illumination source (**Figure 4.3b**). We designed a PCB to house the microcontroller and power the illumination sources for further experiments and added modular external stimulus capabilities to the circuit (**Figure 4.4**) for experiments expanded upon in a later section.

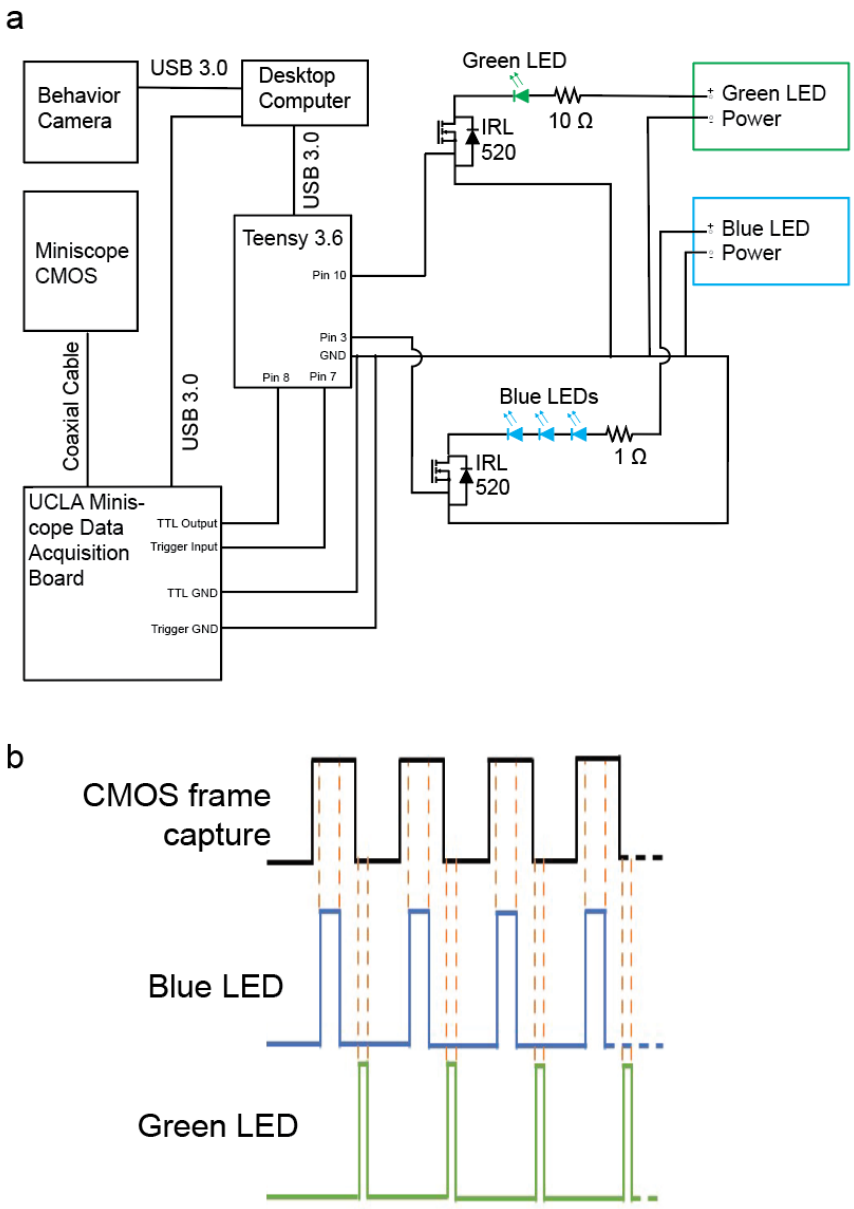


**Figure 4.3 Mesoscope Hardware Control Schematic:** **(a)** Final hardware schematic for the Mesoscope system wiring including the microcontroller interface with the computer, CMOS sensor, and LED illumination sources. There is also synchronized behavior camera recording with the CMOS sensor mounted to the Mesoscope. All hardware components are timed and synchronized through a custom built computer to handle high data acquisition. **(b)** A trigger circuit uses time stamps of CMOS frame acquisitions to precisely switch between the blue LEDs and green LED. At 30 Hz CMOS frame acquisition, the blue LEDs were pulsed for 20 ms during odd frames and the green LEDs were pulsed for 4 ms during even frames.

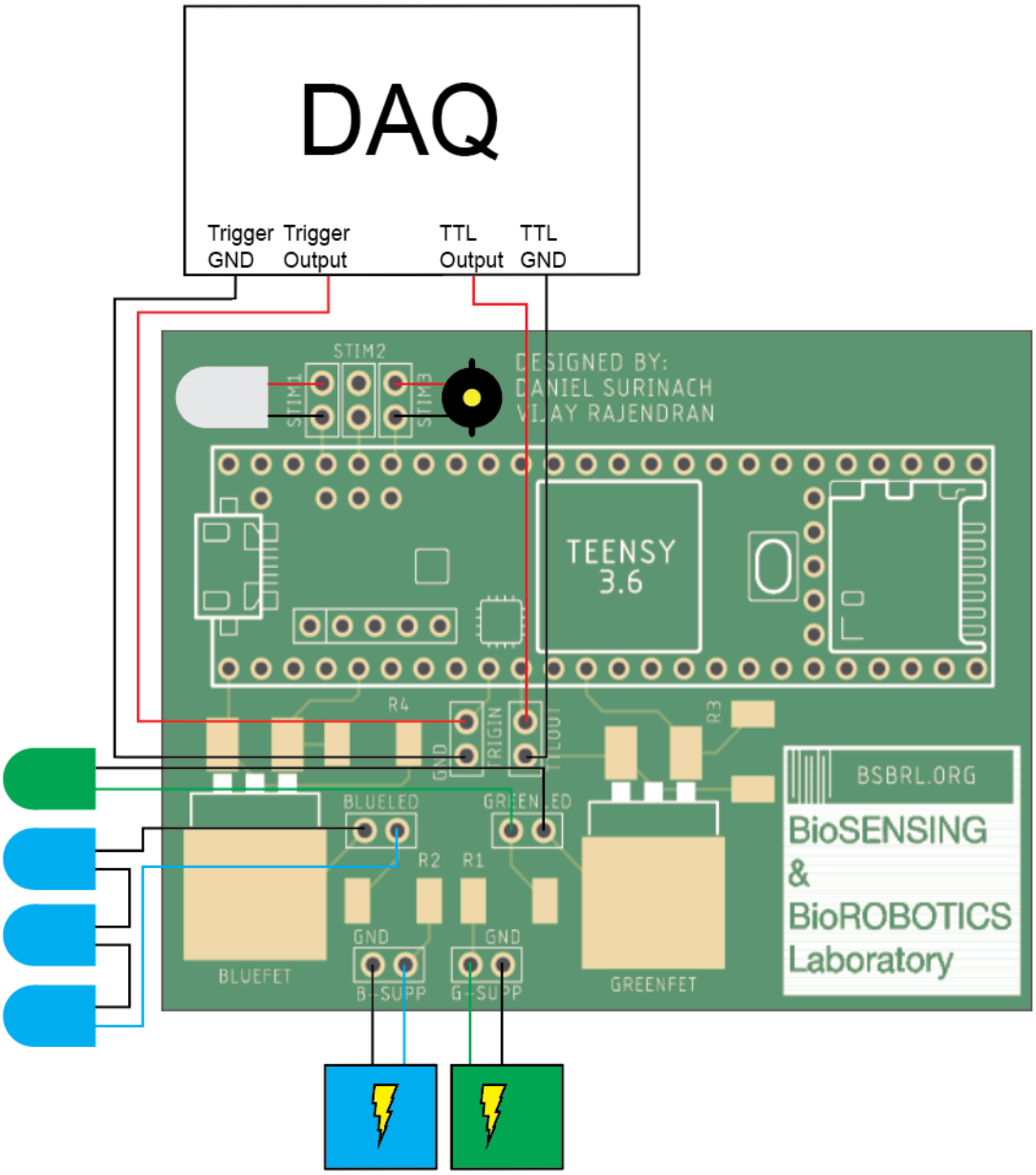


**Figure 4.4 LED Power Printed Circuit Board Design:** A PCB was designed to house the microcontroller and on-board components required for the switching circuit. The PCB can connect to different illumination sources that are powered with external power supplies. The Miniscope DAQ can interface with the microcontroller through set pins on the PCB to synchronize LED pulsing with frame acquisition. The PCB has functionality to control external stimuli. Shown here are a white LED and a piezo-vibrating element for sensory stimuli.

# Chapter Five

# Software and Hardware Development

## 5.1 Microcontroller Programming

The Teensy microcontroller has interface capabilities with the native Arduino library and was programmed using the Arduino IDE. There were programmed 5 output pins on the microcontroller that control blue LED illumination, green LED illumination, video triggering, and 2 optional external stimuli. There was 1 programmed input pin that reads TTL pulses from the CMOS sensor to precisely time LED illumination. The script prompts the user to input a command ('y') which sends the video trigger pulse to the DAQ to begin the behavior and CMOS sensor recordings. The microcontroller is then programmed to wait until it receives the first TTL pulse from the DAQ indicating the video has been triggered to start and a frame has been collected. The first TTL pulse value is assigned to the blue illumination output pin and will be switched on for the desired pulse duration during odd frames. A non-blocking function takes advantage of the micro-second clock on the microcontroller to switch the LED sources on and off without delaying the microcontroller. The microcontroller is programmed for hardware interrupts when the state of the TTL pulse has changed (i.e. during an even frame capture) and will switch the illumination output pin source (i.e. switch to the green illumination pin during even frame captures). Similar

non-blocking functions are implemented for external stimuli, whereby the user can input a real-world time to apply the stimulus and how frequently to apply it in an experiment. This process is repeated until the user-defined experiment and trial time have been reached. A summary of the code architecture is shown in **Figure 5.1**. In addition to alternating LED control, the microcontroller can be programmed to pulse only one LED repeatedly.

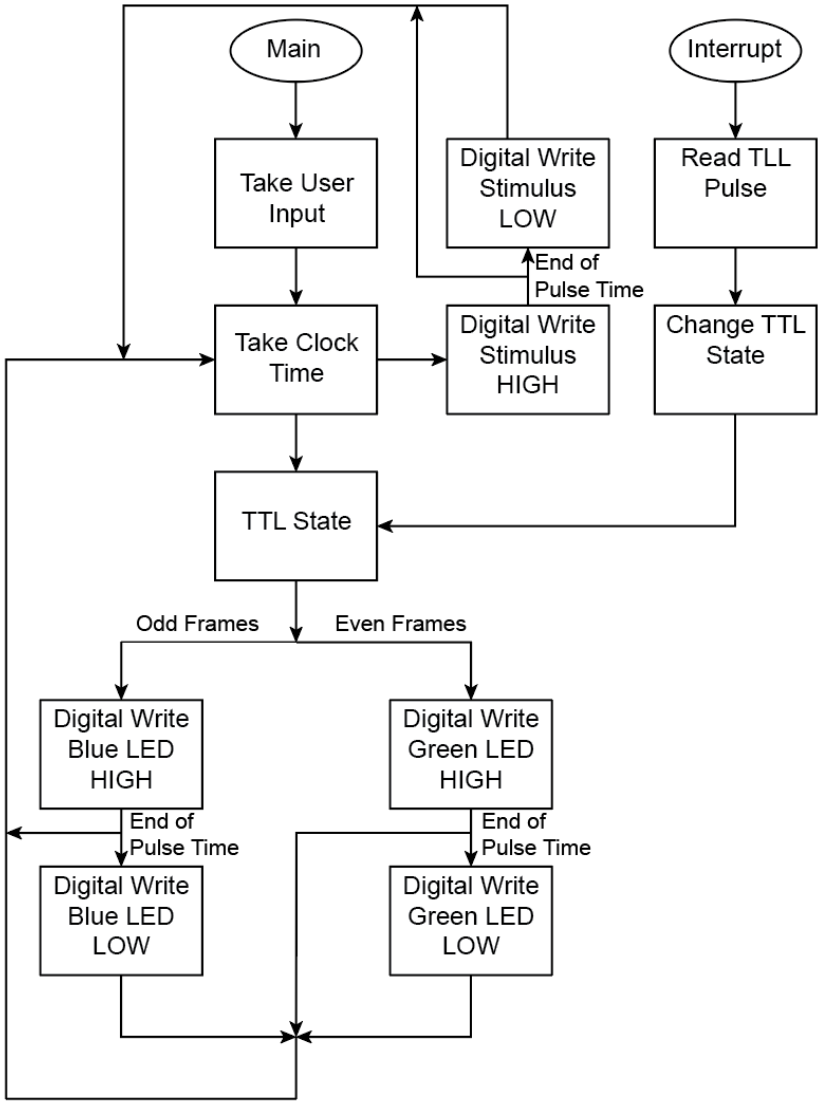


**Figure 5.1 Microcontroller Programming Schematic:** Microcontroller programming schematic detailing the process behind synchronized LED pulsing and optional stimulus presentation. The main function takes in user-inputs to trigger video capture and a hardware interrupt function runs outside of the main loop to read changes in the TTL pulse received when a frame is captured. The hardware interrupt will execute when a state change is detected and restart the program to the beginning of the main loop. Non-blocking functions power each LED and stimulus by taking advantage of the microcontroller micro-second clock. Digital signals (+3.3V) are written to turn on each desired output pin until the user-set time limit has been reached. The digital signal then inverts and shuts off power to the desires output pins. This process occurs delay-free with a constant micro-second clock time taken every main loop iteration.

## 5.2 Data Analysis Pipeline

### 5.2.1 Behavior Video Analysis

In the open field and social behavior experiments, DeepLabCut[38] was used to track the position of the solitary mouse and the companion mouse over time. Twenty frames from each social behavior trial were randomly extracted using k-means clustering and used as training data for the machine learning algorithm. Four body points were tracked on each mouse via deep neural networks embedded in the DeepLabCut software. The positions of all points were averaged to acquire a center-of-mass-like position of each mouse, which was tracked across all frames to generate the plot shown in **Figure 7.3b, Figure 7.4b**. To segment the behavior based on different behavior epochs, we manually scored behavior with 1 s precision based upon whether the mouse with the Mesoscope was moving, still, grooming or rearing, and whether the mice engaged in social behavior or not indicated by touching, sniffing, or close proximity to the companion mouse and categorized into "contact" and "no contact" epochs. This data was further processed only if there was consensus among at least 3 of the 4 independent scorers.

### 5.2.2 Imaging Data Pre-Processing

All data from the CMOS sensor was captured in .avi format (RGB, 480x752 image size) and contained alternately pulsing blue and green channel data. The video sequences were processed through a custom MATLAB script. Videos were converted from RGB to grayscale and segmented to exclude the 2-minute LED warmup period at the start of each trial. The resulting video sequence was segmented into individual blue and green channel videos.

### 5.2.3 Sensory Evoked Responses

The blue and green channel videos contained 18 stimulus trials per experiment. A time stamp file generated during the experiment was used to segment this video into its respective 18 trials. We detrended and spatially filtered each individual trial using a custom weighted spatial filter to remove additional illumination artifacts from the LEDs. The resulting DF/F data for each trial was saved to a .csv file and then averaged into a single .csv DF/F file.

### 5.2.4 Open Field Experiments

The blue and green channel videos acquired from freely moving animals were additionally corrected for lateral motion artifacts using MoCo rigid motion correction.[39] A macro was used to automate the process and maintain consistency of MoCo parameters across trials. The first frame of the video was used as the template for motion correction. Parameters used for the MoCo plugin were w = 40 and a down sample value = 0.5. Log files of pixel displacements were saved to .csv files. Resulting videos were saved as .avi files with JPEG compression at 15 fps. The motion corrected blue and green channel videos were re-concatenated back into an alternately pulsing video to mitigate data storage issues during further analysis.

The time stamp data from the Miniscope software contains a list of frames captured by the behavior camera and CMOS sensor. To mitigate frame pacing issues with the CMOS sensor, only frames within $\pm$ 10% of the specified frame rate were kept. To address the frame dropping issues with the behavior camera (usually dropped $\sim$400/10800 frames), common frames that exist in the CMOS video and behavior camera video were kept. The resulting data was compared to the scoring data to find the intersect between these frame data sets. Finally, this data set was searched through to find points with paired blue and green frames (for hemodynamic corrections) and served as the final blue and green channel

frame data used for analysis.

Each motion corrected pulsing video was binned using a bilinear spatial binning algorithm in MATLAB. Pixels in each channel were separately corrected for global illumination fluctuations using a global correction algorithm[6] and were spatially filtered using a custom weighted spatial filtering algorithm.

### 5.2.5 Hemodynamic Correction

After correction for global and illumination artifacts, the corrected frames were passed to a hemodynamic correction algorithm[13] shown below:

$$F_C = \frac{\frac{F_b}{\overline{F_b}}}{\frac{F_g}{\overline{F_g}}} \tag{5.1}$$

$F_b$ is the corrected fluorescence trace for a blue frame and $\overline{F_b}$ is the mean fluorescence trace across all blue frames in the time series. The green frames' normalization is conducted similarly. Dividing both the normalized blue and green intensities in every pixel and frame yields $F_c$, the hemodynamic corrected pixel data for every frame in the FOV.

### 5.2.6 Blood Vessel Diameter Tracking

Blood vessel diameter tracking was performed using a custom written macro in Fiji. Blue channel videos were inverted, and the background was subtracted using a rolling ball radius of 30 pixels. The rectangular ROI was then drawn around the vessel to be analyzed. The rectangle was used as a guide to create 6 evenly spaced, horizontal lines along the height of the rectangle. The lines were 5 pixels thick and as long as the width of the

rectangle. These lines were used as ROIs to track the vessel diameter throughout a trial (**Figure 7.2a-b**). To calculate vessel diameter, the intensity profile along a line was first plotted. Then, the maximum intensity and its corresponding location in pixels along the line was found. Using half of the maximum intensity as a threshold, the macro then searched for the pixel with the lowest intensity greater than the threshold in both directions from the maximum intensity. The difference between the pixel locations of these two values was then stored as the vessel diameter. This process was repeated for each line and each frame in a video. Values were saved in a .csv file for further analysis.

Post-processing and plotting of data were performed in MATLAB. The percent change in vessel diameter (Dd/d) was calculated for 4 of the 6 ROIs (the most anterior and most posterior ROIs were excluded due to sub-optimal resolution in these regions). The baseline was the average vessel diameter across time at each ROI. Time-series of diameter changes were then plotted as 5-point moving averages along with the average of those traces (**Figure 7.2b**). Behavior data was plotted using the consensus among scorers and then padding the behavior epochs on either side by $\sim$0.5 $s$ (7 frames). Spikes with prominence greater than 10% and longer than 1/3 $s$ were detected using MATLAB. Variances shown in **Figure 7.2c-d** were calculated by first pooling the variances from behavior epochs to obtain a variance for each behavior within a trial. The weighted average of these variances was then taken across trials to obtain a single measure for each behavior.

A Wilcoxon signed-rank test was performed on variances from still, moving, grooming, and rearing behavior (**Figure 7.2c**). A paired sample t-test was performed on spike frequencies from still, moving, and grooming behavior (**Figure 7.2e**). Statistical tests were not performed for social behavior plots due to the small number of samples (n = 3).

### 5.2.7 DF/F Calculations

Intensity values from the selected ROIs from the blue and green illumination videos were computed using FIJI.[40] Further analysis was performed in MATLAB. Change in fluorescence for both GCaMP and reflectance signals were calculated over a baseline average across the whole time series. Correction for hemodynamics was performed using a ratiometric method as described previously.[41]

### 5.2.8 Seed-Pixel Correlation Maps During Free Behavior

Cortical regions of interest were selected within each video trial by removing the background and areas with high vasculature (**Figure 7.3d, Figure 7.4d**) and seed pixels within 6 regions (motor cortex (M1), frontal lobe (FL), barrel cortex (BC), retrospenial cortex (RSC), visual cortex (VC), hind limb (HL)) were selected for further analysis. Seed pixel correlation maps were generated using Pearson's correlation coefficient (PCC) to compare the correlation between a desired seed pixel corrected GCaMP trace and the other pixels in the FOV. The data from the manual scoring in (**Figure 7.3c, Figure 7.4c**) was used to generate a list of frame numbers where the mouse was either moving or still. These epochs of time are discontinuous between behaviors, so a moving window was applied to each continuous epoch of time. The window length was 1 $s$ (15 frames at 15 fps) with a 0.5 $s$ sliding window. The PCC between the seed pixel trace and every other pixel in the desired regions of the cortex was calculated for each window length portion. The mean of all the PCCs was calculated and stored as the PCC value for each pixel in the ROI relative to the desired seed pixel. This process was repeated for each trial and mouse to generate representative seed pixel maps for one trial as shown in **Figure 7.3e**. Focusing on the PCC between seed pixels in the same representative trial, we generated a cross-correlational map shown in **Figure 7.3f**, where the bottom triangular data represents the still behavior

PCC values and the top triangular data represents the moving behavior PCC values. The PCC value between the chosen seed pixels were averaged across all trials in spontaneous free behavior to generate the inter-seed cross-correlational plots shown in **Figure 7.3g**. To measure the change in activity across the left hemisphere where the seed pixels were chosen, the percentage of pixels in this ROI with PCC r>0.5 was averaged across trials (**Figure 7.3h**). Similar analysis was performed for social interaction experiments (**Figure 7.4**).

### 5.2.9 Glutamate Data Preprocessing

Raw data of spontaneous glutamate activity was preprocessed based on the following steps: First, the time series of each pixel was filtered using a zero-phase bandpass Chebyshev filter between 0.1 and 5 Hz. Then a baseline signal was calculated by averaging all the frames, and the fluorescence changes were quantified as DF/ F x 100, where F is the filtered signal. To reduce spatial noise, images were filtered by a Gaussian kernel (5x5 pixels, sigma = 1).

### 5.2.10 State Scoring During Sleep Studies

Behavioral states were scored visually using hippocampal LFP and movement signal in 10 $s$ epochs. Movement signals were calculated using a previously described algorithm63. Active wakefulness (aW) was characterized by theta hippocampal activity and high movements. Quiet wakefulness (qW) was characterized by theta hippocampal activity and minimum movement. NREM sleep (N) was characterized by large irregular activity in hippocampus and no movement. REM sleep (R) was characterized by theta hippocampal activity and no movement.

### 5.2.11 Correlation Analysis During Sleep Studies

A uniform meshgrid with 1.2 $mm$ distance between its points was laid on the field of view and signal at each ROI (0.2 $mm^2$) was calculated. Quiet wake, NREM sleep and REM sleep were scored for each recording based on above criteria and Pearson correlation coefficients were calculated between each ROIs during qW, NREM and REM.

# Chapter Six

# In-vivo Calcium Imaging in Anesthetized Mice

## 6.1 Mouse Preparation For Imaging Sessions

Prior to every in-vivo study performed throughout this paper, See-Shell implants are prepared and surgically implanted[35] on Thy1-GCaMP6f mice using the techniques adapted from our previous work.[34] See-Shell implants are retrofitted with the magnetic interlocking mechanism (see **Figure 2.4a**) for quick attachment to the Mesoscope. The mice were allowed to recover for at least 7 days after implantation prior to any experiments. The recovery period was followed by an acclimatizing period whereby an experimental handler trained each mouse with the Mesoscope. For experiments requiring anaesthetization, mice are given experiment-dependent isoflurane anaesthesia concentrations and head-fixed with a custom machined stereotax.

## 6.2 Focusing and Calibration of The Mesoscope

Prior to imaging experiments, each mouse was briefly anesthetized under 0.5-1% isoflurane in oxygen. The protective cap was removed and any debris on the surface of the See-Shell implant was cleaned using distilled water and cotton tipped applicators. The Mesoscope was placed on the implant and secured via the magnetic interlocking mechanism and an 0-80 screw in the posterior tab. The green LED was switched on and the position of the top housing relative to the bottom housing was manually adjusted until the area around the midline was in focus (**Figure 6.1a**) and the adjustment screw was tightened to secure it in place. Once focused, the three blue LEDs and the single green LED were alternately pulsed and their intensities were adjusted by modulating the power delivered to the LEDS using each power supply to ensure there are no points of over-saturation in the FOV (**Figure 6.1b**).

## 6.3 Comparison to Conventional Widefield Epifluorescence Imaging

To benchmark *in-vivo* imaging capabilities of the Mesoscope, we performed experiments in which a mouse anesthetized with isoflurane was imaged using the Mesoscope and a conventional epifluorescence macroscope in the same experimental session (**Figure 6.2a**). Mice were anesthetized with 1% isoflurane in a custom stereotaxic setup under a conventional epifluorescence macroscope (Leica MZ10F, Leica AG). Images from the macroscope were captured using a sCMOS camera (Orca Flash 4.0, Hamamatsu Inc.). Bright field images were first captured to assess the quality of the cranial window followed by epifluorescence imaging. Since blue illumination was provided every alternate frame in the Mesoscope, the effective image capture rate was 15 Hz. To closely replicate these

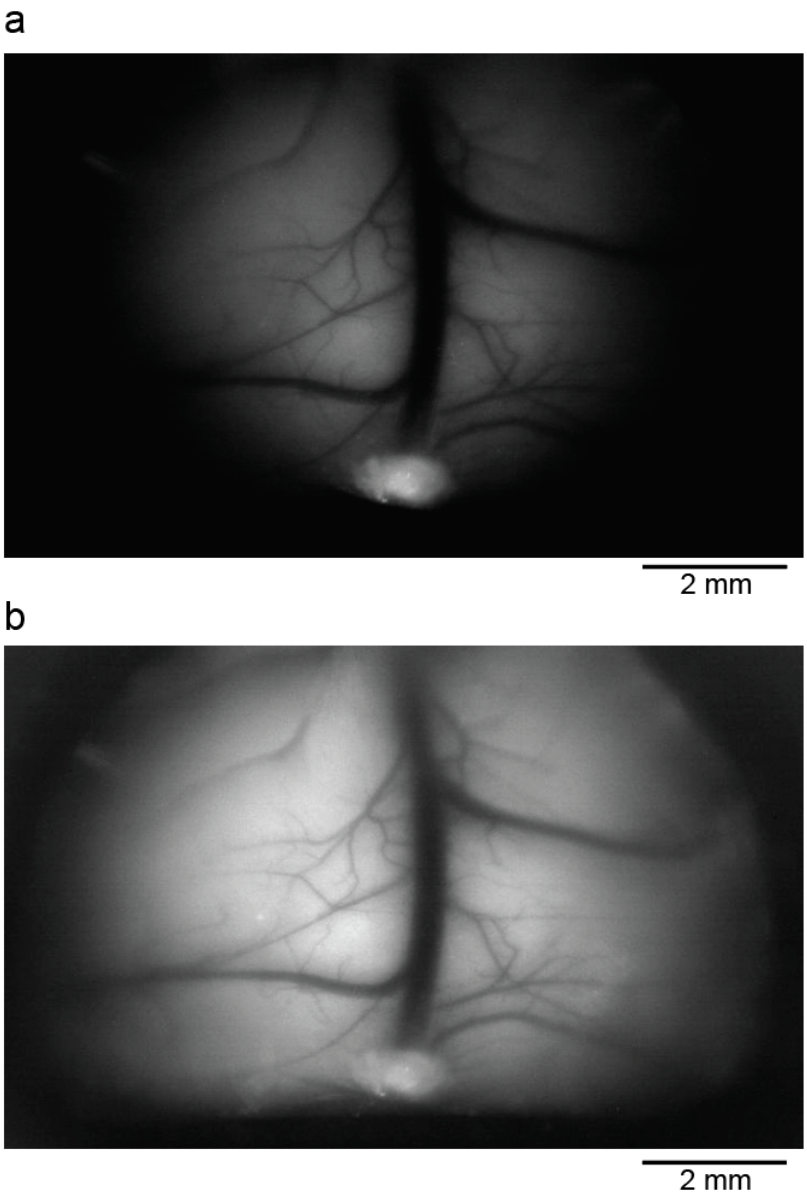


**Figure 6.1 Focusing and Calibration of An *In-Vivo* Mouse Cortex:** *In-vivo* focusing and calibration of the mouse dorsal cortex viewed through the Mesoscope. Mice were briefly anesthetized under 0.5-1% isoflurane and the position of the top housing of the Mesoscope relative to the bottom housing was manually adjusted until the area around the midline was in focus. **(a)** Still image of the cortex captured through the Mesoscope under green LED illumination. Continuous green illumination is utilized to focus the Mesoscope along the midline and pulsing green illumination is utilized to collect reflectance data. LED power adjustments are made for green illumination until there are no points of over-saturation in the FOV. **(b)** Still image of the cortex captured through the Mesoscope under blue LED illumination at the same focal point set in (a). Pulsing blue illumination is utilized to collect calcium data. LED power adjustments are made for blue illumination until there are no points of over-saturation in the FOV.

imaging conditions, the sCMOS camera was configured to acquire images at 8 bits and 30 fps. In the final imaging analysis, every other frame was discarded to ensure an effective acquisition rate of 15 Hz. The Mesoscope was attached immediately after image acquisition from the macroscope and 4 minutes of video was captured at 30 fps.

Despite significant differences in optics quality, we captured qualitatively comparable images with both instruments. Vasculature was sharper in imaging data from the macroscope, but most major blood vessels and some finer details were visible in imaging data from the Mesoscope (**Figure 6.2b**). Additionally, we observed oscillations in the calcium signals at 6-7 Hz in the imaging performed with both instruments (**Figure 6.2c-d**), consistent with previous studies.[29] A discrete Fourier transform (DFT) of the calcium traces illustrates clear peaks that are observed in this frequency range (**Figure 6.2c**). We next analyzed the DF/F traces captured from randomly chosen ROIs at $\sim$3 $mm$ laterally and -2 $mm$ posterior to Bregma across the FOV. The histogram of DF/F values acquired from three ROIs is shown in **Figure 6.2d** indicates minimal differences in mesoscale DF/F traces between the data captured from the two instruments. No differences were apparent in the z-scores of the intensity values, which normalizes the variance of raw intensity values thereby accounting for differences in baseline intensities (**Figure 6.2e**).

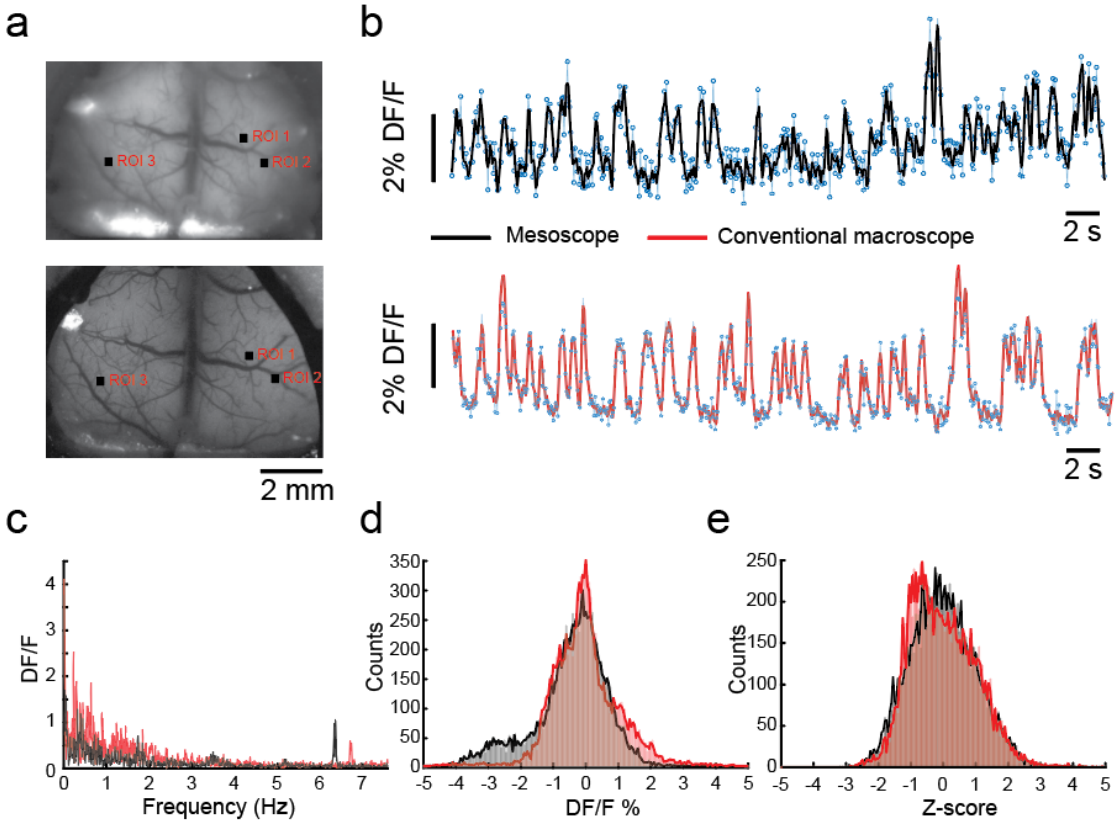


**Figure 6.2 Comparison of Calcium dynamics imaged with the Mesoscope to A Conventional Macroscope:** *In-vivo* experiments conducted on an anesthetized Thy1-GCaMP6f mouse under 1% isoflurane anesthesia. **(a)** *Top:* Image of the dorsal cortex taken with the Mesoscope. *Bottom:* Image taken with a conventional widefield epifluorescence macroscope during the same experimental session. Black squares indicate ROIs selected for DF/F traces analyzed in (b-e). **(b)** DF/F traces of ROI 1 shown in (a) recorded for 120 seconds. Black and red traces indicate filtered traces (Savitzky-Golay filter, 3rd order polynomial, 5 point moving average) of DF/F recorded from the Mesoscope and the macroscope respectively. Blue trace with markers indicates raw DF/F values. **(c)** Plot of the DF/F/Frequency obtained by computing the discrete Fourier series of the traces shown in (b). **(d)** Histogram of DF/F values over 2-minute videos captured with the Mesoscope and the conventional macroscope in the three ROIs indicated in (a). **(e)** Histogram of z-scores of fluorescent intensity values over 2-minute videos captured with the Mesoscope and the conventional macroscope in the three ROIs indicated in (a).

## 6.4 Sensory Stimulus Evoked Responses

Stimulating distinct sensory pathways evoke neural activity in distinct primary sensory areas located within the dorsal cortex. We used the Mesoscope to map evoked responses to two sensory stimuli. Each experiment set contained 18 stimuli. A mouse under light (< 1% isoflurane) anesthesia was first provided with a series of brief vibrational stimuli (1 $s$ long, 100 Hz) to the right hind limb (**Figure 6.3a**). As expected, somatosensory stimulus evoked robust calcium activity in the contralateral hind limb (HL) region of the somatosensory cortex within 500 $ms$ of the onset of stimulus (**Figure 6.3b-c**). The peak post stimulus response was 1.68% $\pm$ 0.49% DF/F (**Figure 6.3d**, n = 17 trials in 1 mouse). In comparison, the peak post-stimulus response on the ipsilateral side was 0.70% $\pm$ 0.34% DF/F (**Figure 6.3e**), significantly lower as compared to the contralateral response (**Figure 6.3f**, p < 0.01, t-test). In a similar fashion, the same mouse was presented with a 100 $ms$ long flash of white light to the left eye (**Figure 6.4a**), and we observed a robust increase in calcium activity in the contralateral visual cortex (**Figure 6.4b-c**). The peak post stimulus response was 1.7% $\pm$ 0.32% DF/F (**Figure 6.4d**, n = 18 trials). In comparison, the peak post-stimulus response on the ipsilateral visual cortex was 0.38% $\pm$ 0.057% DF/F (**Figure 6.4e**), significantly lower as compared to the contralateral response (**Figure 6.4f**, p < 0.01, t-test). Thus, the Mesoscope is able to reliably measure expected evoked response to varied sensory stimuli in both hemispheres of the dorsal cortex.

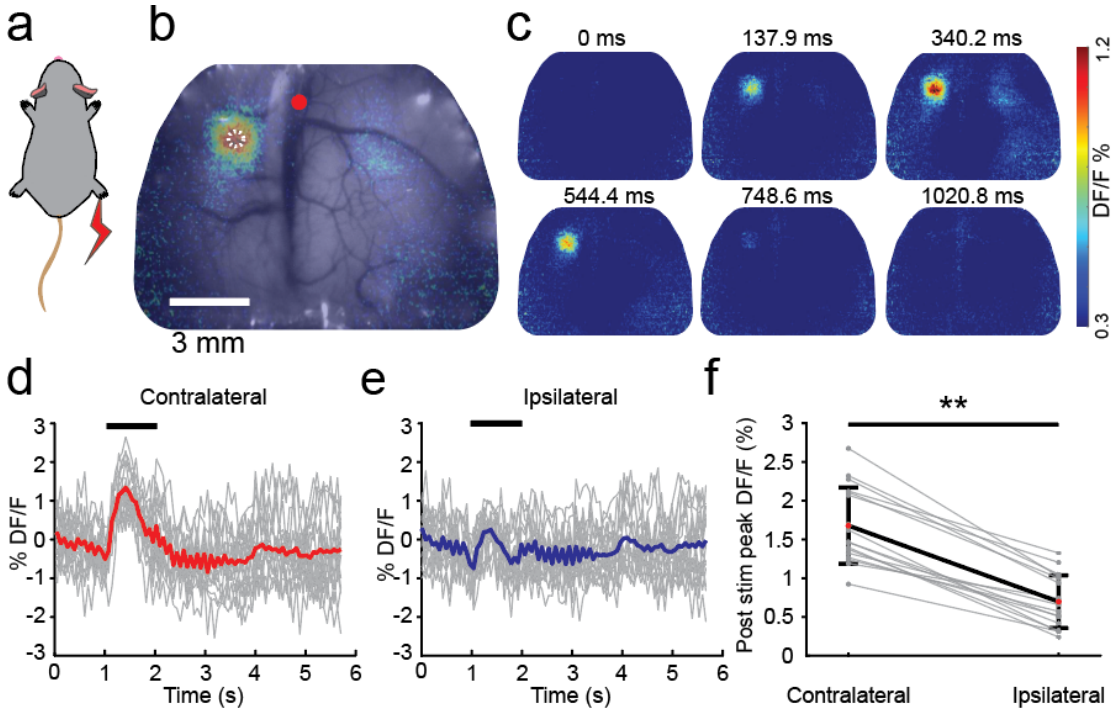


**Figure 6.3 Motor Cortex Evoked Responses Imaged By The Mesoscope:** **(a)** Depiction of a Thy1-GCaMP6f mouse under 1% isoflurane anesthesia conditions with an applied vibration sensory stimulus. **(b)** Composite image of the raw, grayscale brain captured through the Mesoscope and the frame where the largest average DF/F occurred within the 1-second stimulus period. **(c)** Pseudo-color images of time-series evolution of the calcium response in the average DF/F video in response to the vibration stimulus. **(d)** DF/F traces of the contralateral ROI drawn in (b). Red line denotes the average contralateral response whereas the grey lines denotes each individual trial. **(e)** DF/F traces of ipsilateral pair of the ROI drawn in (b). The blue line denotes the average ipsilateral response whereas the grey lines denote each individual trial. **(f)** Peak contralateral and ipsilateral response to the vibration stimulus taken within a 1-second window after the stimulus is applied. The bolded line corresponds to the average peak response whereas the grey lines indicate the peak response for each trial.

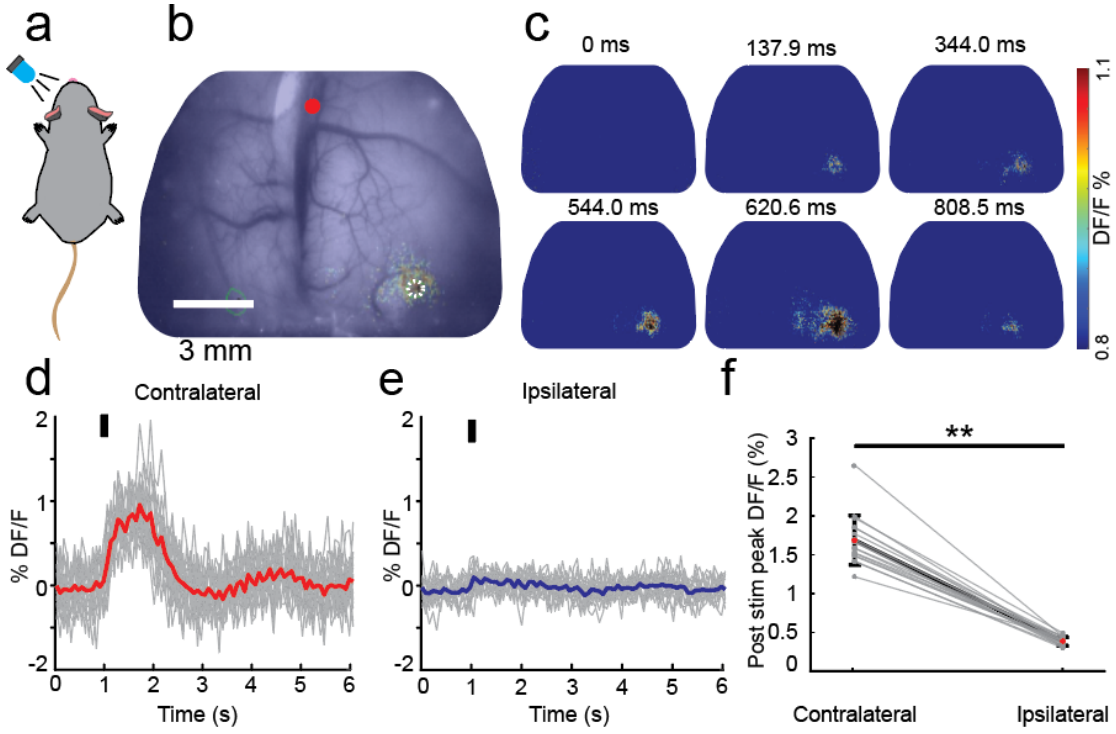


**Figure 6.4 Visual Cortex Evoked Responses Imaged By The Mesoscope:** **(a)** Depiction of a Thy1-GCaMP6f mouse under 1% isoflurane anesthesia conditions with an applied LED sensory stimulus. **(b)** Composite image of the raw, grayscale brain captured through the Mesoscope and the frame where the largest average DF/F occurred within the 1-second window following a 100 $ms$ stimulus period. **(c)** Pseudo-color images of time-series evolution of the calcium response in the average DF/F video in response to the LED stimulus. **(d)** DF/F traces of the contralateral ROI drawn in (b). Red line denotes the average contralateral response whereas the grey lines denotes each individual trial. **(e)** DF/F traces of ipsilateral pair of the ROI drawn in (b). The blue line denotes the average ipsilateral response whereas the grey lines denote each individual trial. **(f)** Peak contralateral and ipsilateral response to the LED stimulus taken within a 1-second window after the stimulus is applied. The bolded line corresponds to the average peak response whereas the grey lines indicate the peak response for each trial.

# Chapter Seven

# Open Field and Social Behavior Experiments

Mice were prepared for *in-vivo* experiments in a similar fashion as previously described (see **Section 6.1**).

## 7.1 Stability of Mesoscope Imaging in Freely Moving Mice

We next proceeded to use the Mesoscope to obtain calcium dynamics in freely behaving mice. Free behavior can cause motion artifacts due to two issues: the Mesoscope can move relative to the implant, or the brain can move relative to the implant. When the Mesoscope was attached with the stabilizing screw on the rear tab, there were minimal lateral motion artifacts while the mouse was performing vigorous behaviors such as rearing and grooming (**Supplementary Video 2**). A representative trial of the FOV displacement is shown in **Figure 7.1a**. In the trials that were analyzed, the absolute maximum x and y displacements of the FOV were 21.0 $\pm$ 21.8 $\mu m$ and 14.4 $\pm$ 17.1 $\mu m$, respectively (**Figure 7.1b**, n = 3 mice, 3 trials each). The mean absolute x and y displacement were 2.0 $\pm$ 2.5 $\mu m$ and 9.3 $\pm$ 4.9 $\mu m$, respectively. These motion artifacts were adequately corrected for using using

MoCo rigid motion correction.[39] Limitations on the weight of the device precluded us from adding any more instrumentation such as a laser range finder[19] to measure z-axis deflection. However, based on the numerical aperture of the collector lens, the Mesoscope's depth of focus ranges from $\sim$120 $\mu m$ near the optical axis to $\sim$180 $\mu m$ in more lateral regions of the FOV. Thus, small fluctuations in the z-direction should be within the depth of focus of the device. While it is possible for the brain to move relative to the implant, our previous study has demonstrated that the brain is stable enough across much of the dorsal cortex to enable 2P imaging of single neurons in awake head-fixed animals.[34] Fluctuations of the brain position relative to the implant larger than 100 $\mu m$ should be easily perceptible to the naked eye. In this study (**Supplementary Video 2**), as well as our previous work,[34] such large fluctuations have not been observed.

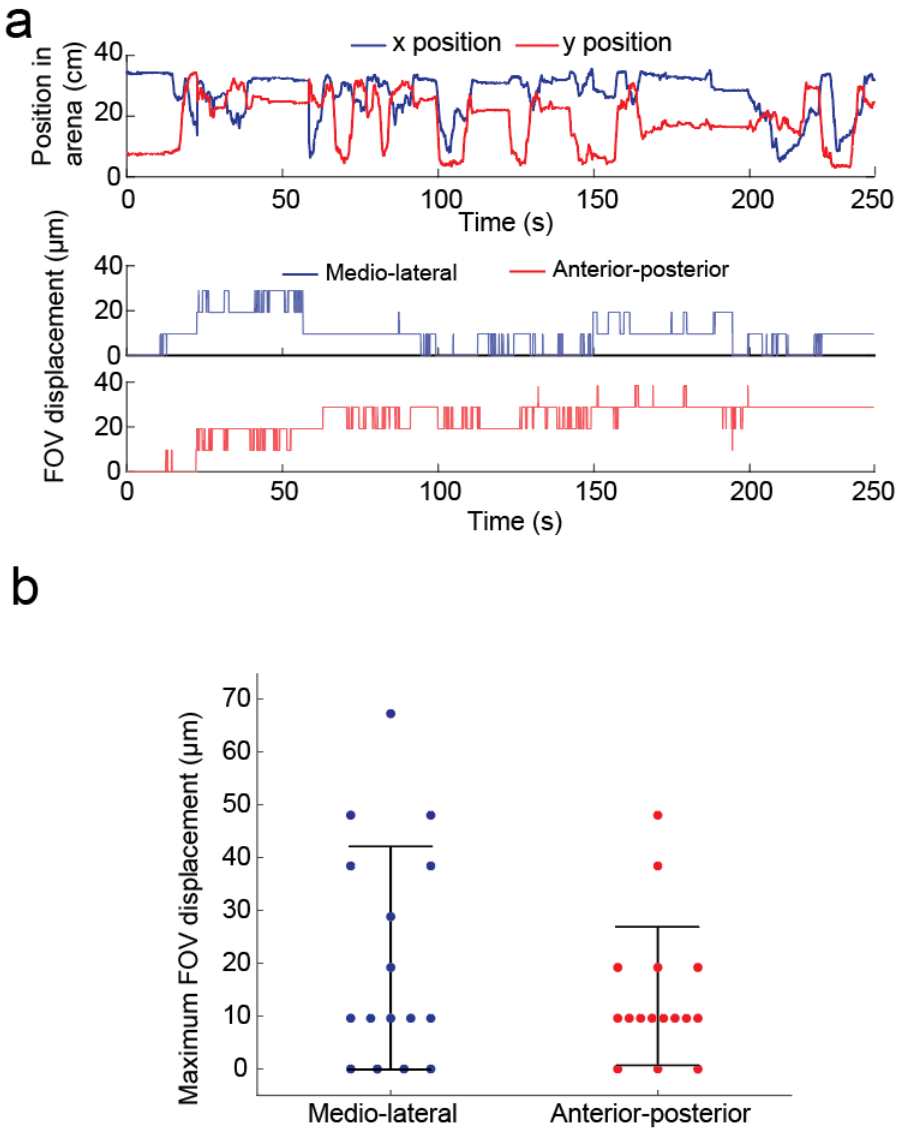


**Figure 7.1 Stability of Mesoscope Imaging:** **(a)** Top: X and Y coordinates of mouse in a 30 $cm$ by 30 $cm$ open field arena during a 4-minute trial. Bottom: Rigid translations of the Mesoscope FOV to correct for motion artifacts in the calcium dynamics video corresponding to the mouse behaving with the positions depicted in (a). **(b)** Maximum rigid translations of Mesoscope FOV to correct for motion artifacts in calcium dynamics videos (n = 16 videos).

## 7.2 Tracking Changes in Superior Sagittal Sinus Diameter During Free Behavior

The Mesoscope images the cortex through the transparent See-Shell implants, allowing relatively high-resolution imaging of the surface cerebral vasculature compared to intact skull imaging. In raw calcium activity imaging videos acquired during freely moving behavior, we observed large changes in the diameter of the superior sagittal sinus (SSS) that were perceptible to the naked eye (**Supplementary Video 2**). Using image processing, we analyzed the changes in diameter of the SSS at various locations (**Figure 7.2a**). Representative traces of the time-series of SSS diameter during an open field behavior trial are shown in **Figure 7.2b**. The measured diameters varied throughout the trial and the variance in percentage change in vessel diameter was comparable when the mice remained stationary, were moving or grooming (n = 6 trials, 3 mice) (**Figure 7.2c**). There was no statistically significant difference between the groups ($p > 0.05$, Wilcoxon signed-rank test). The variance increased during social contact (n = 3 trials, 3 mice) (**Figure 7.2d**). In all trials, we further observed rapid (<0.5 s) and large (>10%) contractions in the SSS. We initially hypothesized that they may occur during motion artifacts caused by behavior. But such spike-like reduction in diameters were observed even when the mice were stationary (**Figure 7.2e**). Like the variances, there was no statistically significant difference between the spike frequencies ($p > 0.05$, paired sample t-test). A consequence of this observed phenomenon was that the areas adjoining the SSS had large lateral motion artifacts that could not be corrected using rigid body motion correction algorithms. Thus, areas within 500 $\mu m$ were excluded in our data analyses of calcium activities. Further, blood from much of the frontal and parietal areas drain into the SSS. Fluctuations in the diameter of the SSS may affect the outflow of blood from these upstream brain regions and potentially points to

mechanism for mesoscale control of cerebral blood flow.

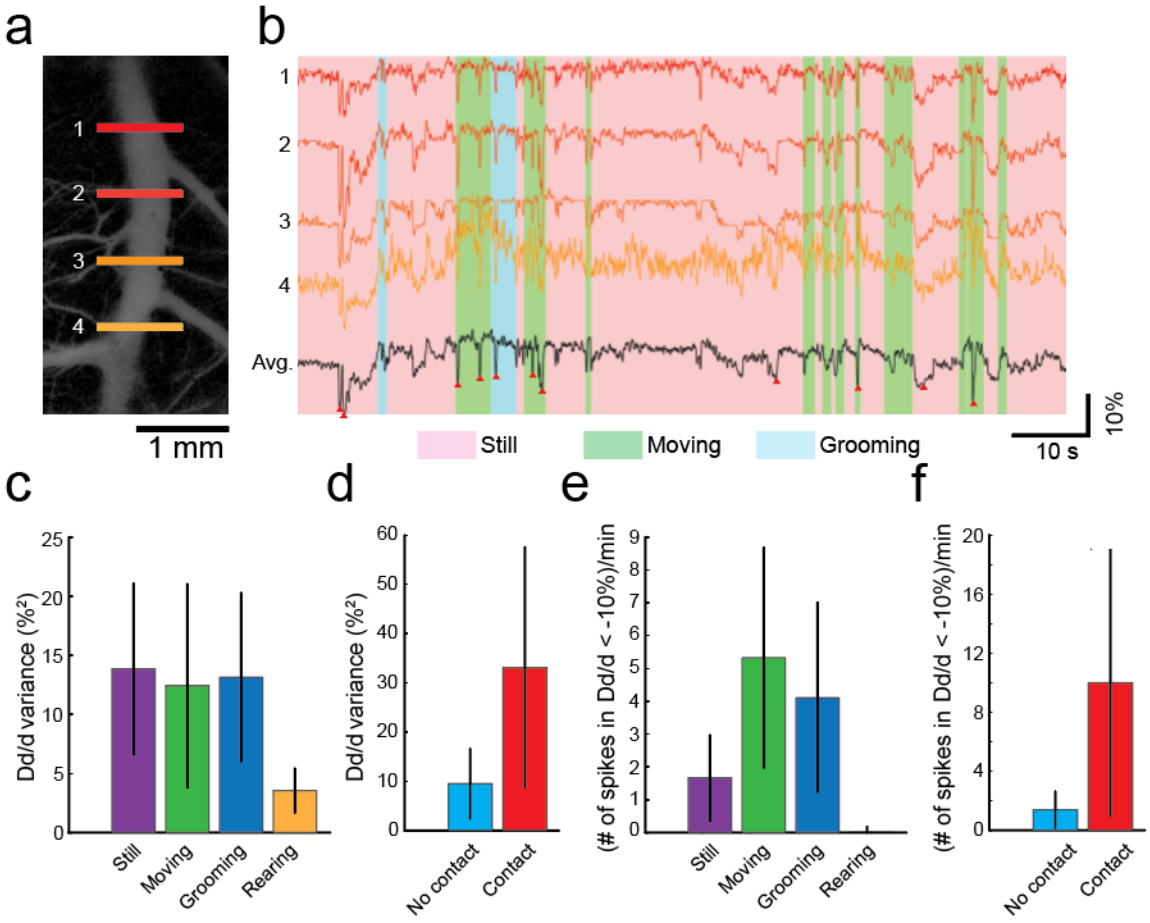


**Figure 7.2 Tracking Diameter of Superior Sagittal Sinus (SSS) During Free And Social Behavior:** **(a)** Image of SSS in the dorsal cortex. Numbered lines indicate cross sections selected for diameter tracking analysis in b. **(b)** Time series evolution of percentage change of vessel diameter at the cross sections specified in a and their average during still, moving, and grooming behaviors. Red triangles along the average trace indicate spikes exceeding 10% prominence. **(c)** Bar graph of the variance in percentage change of vessel diameter (n = 6 trials, n = 3 mice) by behavior. **(d)** Bar graph of the variance in percentage change of vessel diameter by social activity (n = 3 trials, n = 3 mice). **(e)** Bar graph of the rate of occurrence of 10% prominence spikes by behavior (n = 6 trials, n = 3 mice). **(f)** Bar graph of the rate of occurrence of 10% prominence spikes by social activity (n = 3 trials, n = 3 mice).

## 7.3 Cortical Functional Connectivity During Open Field Exploration and Social Interactions

Mesoscale imaging has been used to reveal functional connectivity between cortical areas during spontaneous resting state activity.[6] Such functional connectivity studies have thus far been conducted in head-fixed animals.[6,19] Here we used the Mesoscope to examine functional connectivity during open field behavior of solitary mice and during social interactions with a companion mouse. An overhead camera tracked behavior simultaneously during Mesoscope imaging (**Figure 7.3a, Figure 7.4a**). This was followed by analysis of the behavior videos using DeepLabCut[38] (**Figure 7.3b, Figure 7.4b**). Solitary open field trials, each lasting 2 minutes, were manually segregated into four types of behaviors – time periods when mice were still, moving, grooming, or rearing. On average, mice spent 70.6% $\pm$ 9.0% of the time remaining still (n = 6 trials, 3 mice), while spending 20.7% $\pm$ 7.51% of time moving within the cage. Grooming and rearing were much less frequent and shorter in durations, accounting for 7.7% $\pm$ 6.02% and 1.04% $\pm$ 1.17% respectively (**Figure 7.3c**). To study social behavior, mice bearing the Mesoscope were allowed to first explore the arena for 4 minutes before a companion mouse of the same sex was introduced (n = 3 trials, 3 mice, **Supplementary Video 3**). Social trials lasted a further 2 minutes. Mice spent 41.305% $\pm$ 19.5% of time socially interacting with each other, including touching whiskers or the body (**Figure 7.4c**).

We next constructed seed-pixel cross-correlation maps of the cortex from the calcium activity videos acquired by the Mesoscope during open field behavior. Maps with respect to six seeds within the motor cortex (M1), the forelimb (FL), the hind limb (HL), the barrel cortex (BC) areas in the somatosensory cortex, the retrospenial cortex (RSC) and the visual cortex (VC) were analyzed in each mouse (**Figure 7.3d, Figure 7.4d**). Representative seed

pixel correlation maps with respect to 5 seeds from a mouse during an open field behavior trial are illustrated in **Figure 7.3e**. Correlations between the seed locations changed when the animal was moving versus still. Between the seeds, correlations increased, particularly between those located within somatosensory cortex **Figure 7.3f**. Overall movement induced increased variance in the inter-seed correlations (**Figure 7.3g**). The overall area of the left hemisphere of the cortex that is highly correlated with respect to a given seed location increased for all seeds analyzed when the animal was moving (**Figure 7.3h**) and these increases were found to be significantly higher for M1 and HL ($n = 11$ trials, 3 mice, $p < 0.05$, Mann-Whitney U-test). Similarly, seed-pixel correlation maps were constructed for mice engaging in social behaviors (**Figure 7.4e**). Most social interactions involved mice pausing movement to engage in social behaviors (**Figure 7.4b**). Despite the lack of movement, intra-cortical connectivity was increased during times where the mice were engaged in social behaviors (**Figure 7.4e-h**). These results demonstrate the utility of the Mesoscope to study functional connectivity during two behaviors that are unique to freely behaving mice.

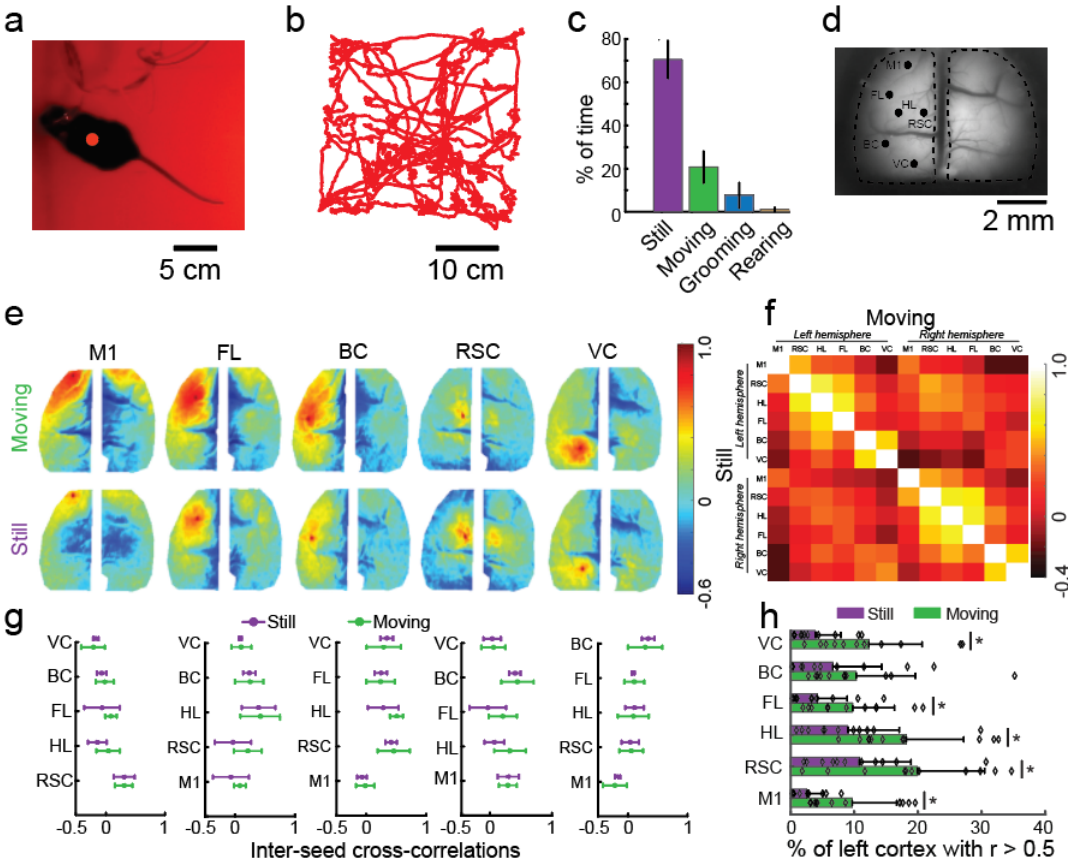


**Figure 7.3 Open Field Behavior Mesoscale Activity Mapping:** **(a)** Photo of a female GCaMP6f mouse fitted with a Mesoscope exploring a 30 $cm^2$ open field arena. **(b)** Trace of instantaneous location of the Mesoscope bearing mouse shown during a 4-minute trial. **(c)** Bar graph showing the average percentage of time spent still, moving, grooming, and rearing during open field behavior (n = 6 trials). **(d)** Representative image of the cortex captured by the Mesoscope during an open field behavior trial. Locations of the seed pixels used for analysis in (e-h) are indicated. **(e)** Seed pixel correlation maps of selected ROIs during movement and no movement. Top row: Average of cross correlations during 1 $s$ epochs of movement. Bottom row: Average of cross correlations during 1 $s$ epochs of no movement. **(f)** Matrix of changes in correlation between selected ROIs in (e) during still and moving behavior epochs. The bottom triangular section represents no motion. The top triangular section represents motion. **(g)** Line plots of average inter-seed cross correlations (n = 11 trials, n = 3 mice). **(h)** Summary plot of change in percentage of cortical hemisphere with r > 0.5 with respect to seed pixels analyzed. * indicates p < 0.05 (Mann-Whitney U-test, n = 11 trials, n = 3 mice).

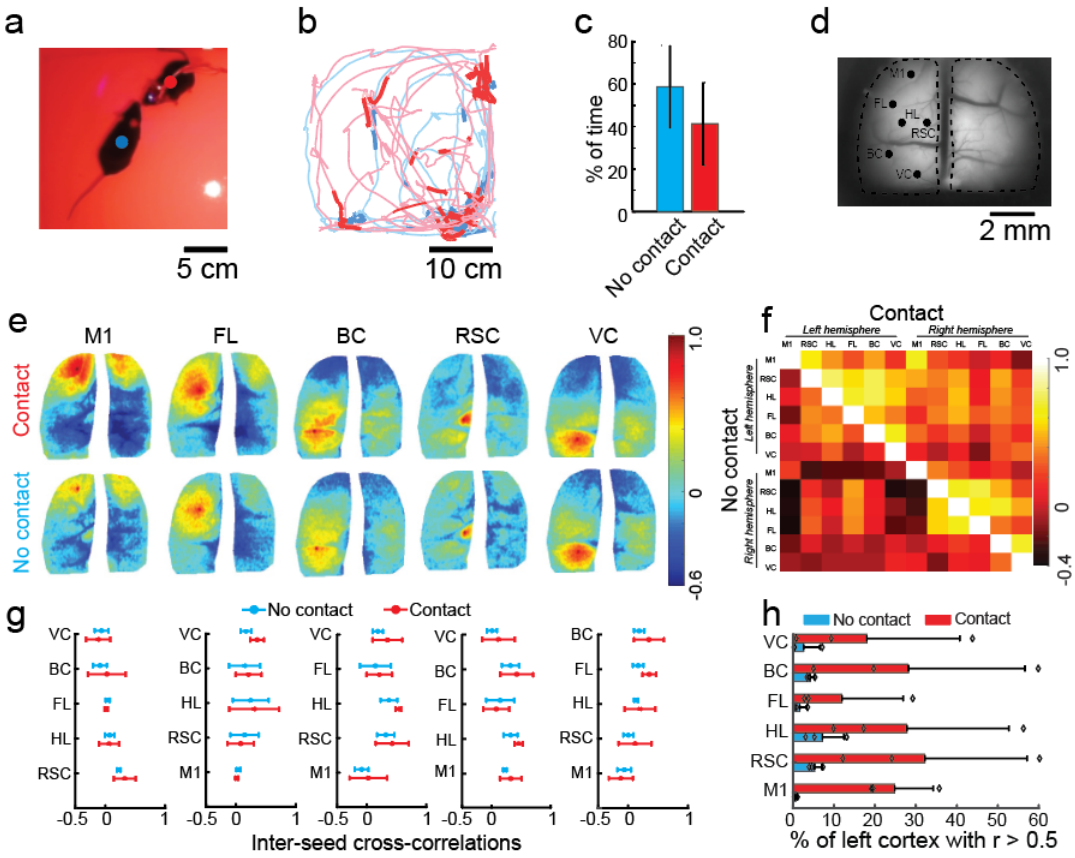


**Figure 7.4 Social Behavior Mesoscale Activity Mapping:** **(a)** Photo of a male GCaMP6f mouse fitted with a Mesoscope interacting with a male C57BL6 mouse in a 30 $cm^2$ open field arena. Mesoscope attached to mice annotated with red marker. Companion mouse annotated with blue marker. **(b)** Trace of instantaneous locations of the two mice shown during a 4-minute trial. The blue trace indicates a mouse with a Mesoscope fitted, and the red trace indicates the companion mouse. The segments of darker blue and red indicate positions of the mice when they were within 5 $cm$ of each other. **(c)** Bar graph showing the average percentage of time spent in contact and not in contact with the companion mouse behavior during trials (n = 3 trials). **(d)** Representative image of the cortex captured by the Mesoscope during a social behavior trial. Locations of the seed pixels used for analysis in (e-h) are indicated. **(e)** Seed pixel correlation maps of selected ROIs during non-social and social behavior epochs. **(f)** Matrix of changes in correlation between selected ROIs in (e) during no contact and contact with the companion mouse epochs. The bottom triangular section represents no contact. The top triangular section represents contact. **(g)** Line plots of average inter-seed cross correlations (n= 3 trials, n = 3 mice). **(h)** Summary plot of change in percentage of cortical hemisphere with r > 0.5 with respect to seed pixels analyzed.

## 7.4 Hemodynamic Correction

Mesoscale imaging of calcium activity using GCaMP indicators is affected by the absorption of light by hemoglobin in the blood.[41,42] Localized changes in blood flow can alter the absorption properties, which can in turn significantly affect the measured fluorescence signal. The green LED in the Mesoscope was switched on every alternate frame to capture reflectance changes simultaneously with calcium activity. Two randomly selected ROIs were drawn around areas of the cortex with pronounced vasculature (**Figure 7.5a**). DF/F head maps were rendered for each frame for the blue, green, and hemodynamic corrected channels (**Figure 7.5b-d** using a previously proposed methodology.[36] **Figure 7.5e** shows representative traces of raw uncorrected blue DF/F signals, green reflectance DF/F signals, and hemodynamic corrected DF/F signals from a randomly seed pixel selected in each ROI. These results demonstrate that the Mesoscope can acquire calcium signals and correct them for artifacts due to hemodynamic responses in regions with pronounced vasculature.

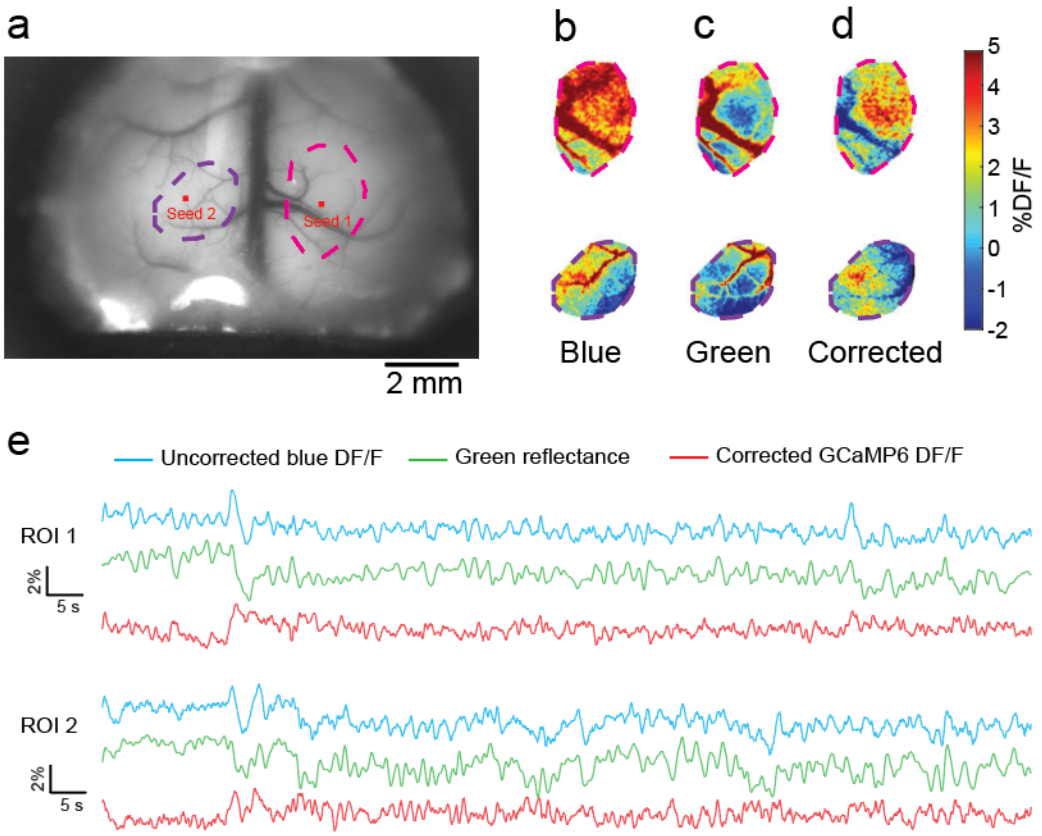


**Figure 7.5 : Hemodynamic Correction:** **(a)** Representative image of the cortex of a GCaMP6f mouse engaging in social behavior. The black line indicates a selected region of interest (ROI) with pronounced vasculature for a hemodynamic correction. **(b)** The blue channel DF/F heat map from the ROI in (a) is selected for a still frame where there is reported high fluorescence activity. **(c)** The green channel DF/F heat map from the ROI in (a) is selected for a still frame where there is reported high reflectance data. **(d)** The corrected DF/F heat map from the ROI in (a) by using the correction algorithm from **equation 5.1**. **(e)** From the same ROI, we can select seed pixels to analyze their traces. **(f)** DF/F traces from the seed pixels chosen in (e) that exist in the ROI chosen in (a) for the blue channel (blue trace), green channel (green trace), and corrected channel (red).

## 7.5 Imaging Glutamate Release Dynamics During Wakefulness and Natural Sleep

As a final demonstration, we used the Mesoscope to measure dynamic changes in extracellular glutamate release in the cortex during transition from wakefulness to natural sleep. Glutamate is an important neurotransmitter that regulates neural activity and cerebral metabolism during wakefulness and sleep. However, much of the previous work studying extracellular release has been done using fixed-potential amperometry,[43] or optical imaging in head-fixed mice.[44] Inducing sleep in head-fixed mice is challenging and typically requires sleep deprivation which can alter the overall sleep structure and patterns of rapid eye-movement (REM) and non-REM (NREM) sleep.[45,46] The design flexibility of the See-Shells allowed us to incorporate local field potential (LFP) recording electrodes in the dorsal hippocampus in Emx-CaMKII-Ai85 mice, expressing iGluSnFR in glutamatergic neocortical neurons.[31,44,47]

In experiments where we performed simultaneous electrophysiology and mesoscale imaging, the hippocampal electrode was implanted through a hole outside the area of the See-Shell craniotomy. Briefly, a bipolar (tip separation of 500 $\mu m$) electrode made from Teflon-coated stainless-steel wire (bare diameter 50.8 $\mu m$) was placed in the pyramidal layer of the right dorsal hippocampus. It was inserted posterior to the occipital suture at a 33-degree angle (with respect to the vertical axis) according to the following coordinates relative to bregma: ML: 2.3 $mm$; dorsoventral (DV): 2.2 to 2.5 $mm$. The position of the electrode tips was confirmed using an audio monitor (AM8C 72x32B, Grass Instrument Co.). After electrode implantation, the craniotomy was performed and the See-Shell was implanted on the skull as described above.

Mice were allowed to naturally transition to sleep in their home cage. Montages of

glutamate activity across the whole dorsal cortex during wakefulness, REM sleep and NREM sleep are shown in **Figure 7.6a**. Hippocampal LFP clearly indicated transition to NREM sleep and subsequently REM sleep (**Figure 7.6b-c**). Consistent with previous studies, spontaneous cortical activity patterns during quiet wakefulness and NREM were highly synchronized across hemispheres.[48] In addition, cortical activity patterns were not necessarily global changes in activity state and were instead composed of complex local activity patterns (**Figure 7.6a**). The transition from wakefulness to NREM sleep and REM sleep resulted in decreased fluorescence, indicating reduced cortical glutamate activity (**Figure 7.6a-d**). We also observed a reduction of slow cortical glutamate fluctuations during REM sleep (**Figure 7.6e**). Correlation analysis of cortical activity revealed that connectivity decreases in REM sleep compared to quiet wakefulness and NREM sleep (**Figure 7.6f-g**). Moreover, consistent with previous studies, the strength of functional connectivity is less in NREM sleep compared to quiet wakefulness.[48]

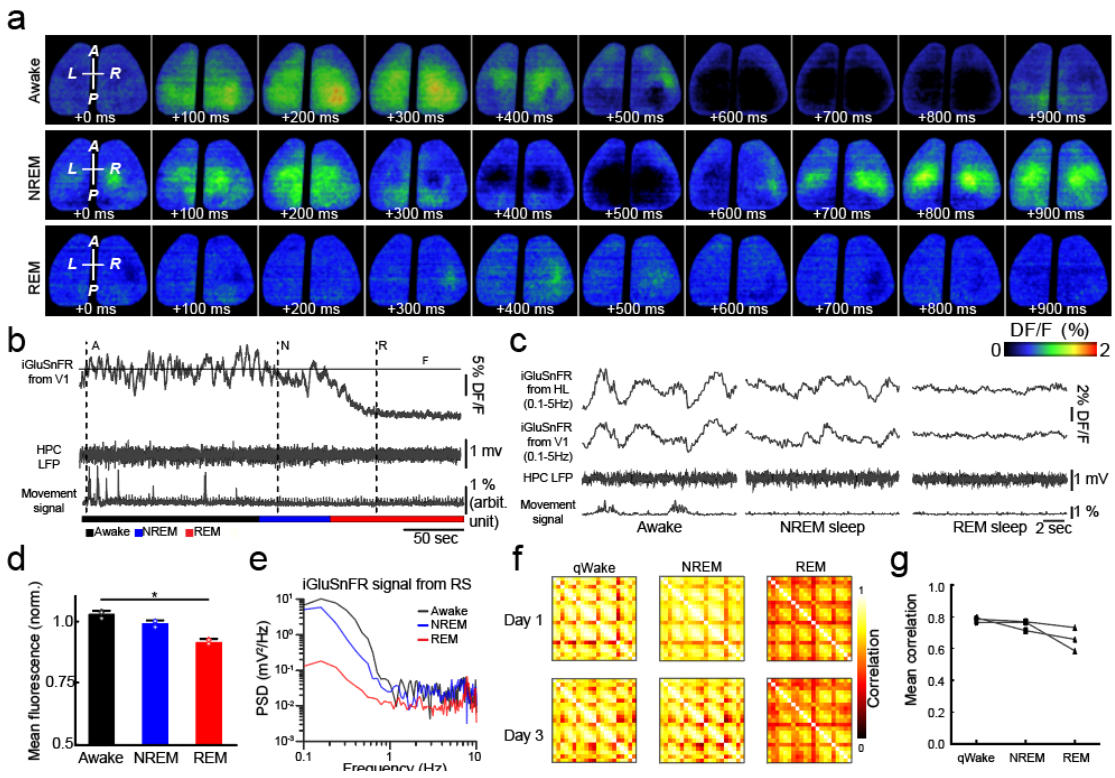


**Figure 7.6 Imaging Cortical Dynamics During Wakefulness and Natural Sleep:** **(a)** Montages of change in glutamate activity over 1s period during awake, REM and NREM sleep states. **(b)** Representative traces of raw glutamate signals from V1, hippocampal LFP, and video-based movement signals during states of waking, NREM sleep and REM sleep in a freely moving mouse. F0 is the baseline glutamate signal calculated by averaging the fluorescence over the entire recording time. **(c)** Magnification of glutamate, LFP and movement signals selected in b. **(d)** Grouped mean raw glutamate signal from the entire cortex (normalized to baseline) during wakefulness, NREM sleep and REM sleep (n = 3 mice, Friedman paired nonparametric test; post-hoc multiple comparison with Dunn's correction * indicates $p < 0.05$. **(e)** Spectral analysis of glutamate signal shows differences in power content between three states. **(f)** Change in the correlation maps of cortical activity between quiet wakefulness, NREM sleep and REM sleep. Cortex was divided into 21 ROIs. Similar changes between quiet wakefulness, NREM sleep, and REM sleep can be observed on different days. **(g)** Reduction of mean correlation of cortical activity from waking and NREM sleep to REM sleep (n = 3 mice).

# Chapter Eight

# Discussion

We have introduced a new neurotechnology for mesoscale activity mapping of the dorsal cortex in freely behaving mice. The Mesoscope represents a significant addition to toolkits available for neuroscientists to study how multiple regions of the cortex coordinate their activity to produce behavior. The overall weight of Mesoscope was comparable to existing head-mounted imaging devices,[27] and it did not significantly affect locomotion in an open-field arena. Despite using relatively simple optics and inexpensive imaging sensor, the Mesoscope performs comparably to a conventional epifluorescence macroscope when used for imaging calcium dynamics across the dorsal cortex. The Mesoscope can simultaneously perform both fluorescence imaging and reflectance imaging to correct for hemodynamic changes. Perhaps the biggest advantage of the Mesoscope when compared to existing preparations for studying mesoscale dynamics is the ability to perform experiments in animals performing complex behaviors that would be impossible to study in head-fixed animals. As demonstrated in this study, we constructed to our knowledge the first functional connectivity maps in mice locomoting and socially interacting with a companion mouse in an open field arena.

Among mammalian models used in neuroscience, mice have the widest range of transgenic animals for broad expression of genetically encoded calcium indicators,[49–51] voltage

indicators[5] as well as reporters of neurotransmitters.[4] In this study we also take advantage of available transgenic mice expressing reporters of glutamate to study dynamics glutamate release in the cortex in naturally sleeping mice. Combined with a wide range of mouse models of neurodegenerative and neuropsychiatric disorders,[52] the Mesoscope should enable studies of mesoscale cortical activity mediating a wide range of complex behaviors in healthy mice and how these activities may be disrupted in diseased states.

The Mesoscope uses simple hardware to enable simultaneous imaging of a large area of the dorsal cortex. Once the custom fabricated parts are procured, the Mesoscope can be rapidly assembled (< 1 day). The design takes advantage of the sensors made available through the open source miniature imaging systems pipeline.[25] This is a rapidly evolving ecosystem where new sensors with increased sensitivity and imaging speed,[53] miniaturization,[28] wireless imaging capabilities[54] being developed. Relatively simple modifications to the current Mesoscope design will allow these newer sensors to be incorporated.

The Mesoscope performs reflectance measurements at a single wavelength using a green LED for correcting for hemodynamic effects. Single wavelength reflectance measurements are not enough for correction of hemodynamic effects.[42,55] In future versions, an additional red LED could be incorporated to obtain reflectance measurements at two wavelengths. This will allow more accurate corrections for hemodynamic effects. Alternately, issues with hemodynamic corrections could be addressed by including illumination at 405 nm to excite GCaMP6f at its isosbestic point.[56] The Mesoscope architecture can also be readily adapted to image red-shifted fluorescent reporters where hemodynamic effects are not prevalent.[2,57] Future improvements on a faster switching power circuit to improve the decay time for the excitation and reflectance LEDs would also provide reductions in any light-leakage between channels and maximize the on-time off each LED to collect more neural and reflectance information.

The Mesoscope was designed to be compatible with our previously developed See-

Shells.[34] Compared to intact skull preparations, implanting the See-Shells increases the surgical complexity, which may be a drawback of the current device. However, the Mesoscope images the cortex at higher resolution compared to intact skull imaging. Additionally, the See-Shell implants can last for long durations of time (< 300 days), allowing the possibility to perform longitudinal and developmental brain imaging studies. See-Shell implantation allows us to readily perceive any motion that may cause artifacts in the imaging. For instance, we tracked minute changes in SSS diameter and were able to precisely eliminate locations close to the SSS where such motion artifacts were observed from further analysis. Higher resolution images can be used to identify surface blood vessels where lateral motion artifacts and hemodynamics cannot be corrected for, and the surface blood vessels can be digitally masked prior to analysis. Further, the digital design methodology of the See-Shell could be used to develop polymer skulls with an expanded FOV to encompass the cerebellar cortex or more lateral regions of the cortex. Finally, future Mesoscopes could be designed to incorporate miniaturized amplifiers for integrating chronically implanted recording electrodes for simultaneous mesoscale imaging and deep brain neural recordings, or to interface with electrodes incorporated in the See-Shells for electrocorticography (ECoG).[58]

# REFERENCES


[1] Chen, T. W. *et al.* Ultrasensitive fluorescent proteins for imaging neuronal activity. *Nature* **499**, 295–300 (2013).

[2] Gong, Y. *et al.* High-speed recording of neural spikes in awake mice and flies with a fluorescent voltage sensor. *Science* **350**, 1361–1366 (2015).

[3] Adam, Y. *et al.* Voltage imaging and optogenetics reveal behaviour-dependent changes in hippocampal dynamics. *Nature* **569**, 413–417 (2019).

[4] Madisen, L. *et al.* Transgenic Mice for Intersectional Targeting of Neural Sensors and Effectors with High Specificity and Performance. *Neuron* **85**, 942–958 (2015).

[5] Daigle, T. L. *et al.* HHS Public Access **174**, 465–480 (2019).

[6] Vanni, M. P. & Murphy, T. H. Mesoscale Transcranial Spontaneous Activity Mapping in GCaMP3 Transgenic Mice Reveals Extensive Reciprocal Connections between Areas of Somatomotor Cortex. *Journal of Neuroscience* **34**, 15931–15946 (2014).

[7] Vanni, M. P., Chan, A. W., Balbi, M., Silasi, G. & Murphy, T. H. Mesoscale mapping of mouse cortex reveals frequency-dependent cycling between distinct macroscale functional modules. *Journal of Neuroscience* **37**, 7513–7533 (2017).

[8] Borden, P. Y. *et al.* Genetically expressed voltage sensor ArcLight for imaging large scale cortical activity in the anesthetized and awake mouse. *Neurophotonics* **4**, 031212 (2017).

[9] Allen, W. E. *et al.* Global Representations of Goal-Directed Behavior in Distinct Cell Types of Mouse Neocortex. *Neuron* **94**, 891–907.e6 (2017).

[10] Wekselblatt, J. B., Flister, E. D., Piscopo, D. M. & Niell, C. M. Large-scale imaging of cortical dynamics during sensory perception and behavior. *Journal of Neurophysiology* **115**, 2852–2866 (2016).

[11] Makino, H. *et al.* Transformation of Cortex-wide Emergent Properties during Motor Learning. *Neuron* **94**, 880–890.e8 (2017).

[12] Orsolic, I., Rio, M., Mrsic-Flogel, T. D. & Znamenskiy, P. Mesoscale cortical dynamics reflect the interaction of sensory evidence and temporal expectation during perceptual decision-making. *bioRxiv* 552026 (2019).

[13] Musall, S., Kaufman, M. T., Juavinett, A. L., Gluf, S. & Churchland, A. K. Single-trial neural dynamics are dominated by richly varied movements. *Nature Neuroscience* **22**, 1677–1686 (2019).

[14] Shimaoka, D., Steinmetz, N. A., Harris, K. D. & Carandini, M. The impact of bilateral ongoing activity on evoked responses in mouse cortex. *eLife* **8**, 1–19 (2019).

[15] Gilad, A. & Helmchen, F. Spatiotemporal refinement of signal flow through association cortex during learning. *Nature Communications* **11**, 1–14 (2020).

[16] Fink, A. J., Axel, R. & Schoonover, C. E. A virtual burrow assay for head-fixed mice measures habituation, discrimination, exploration and avoidance without training. *eLife* **8**, 1–21 (2019).

[17] Guo, Z. V. *et al.* Procedures for behavioral experiments in head-fixed mice. *PLoS ONE* **9** (2014).

[18] Pinto, L. *et al.* Task-Dependent Changes in the Large-Scale Dynamics and Necessity of Cortical Regions. *Neuron* **104**, 810–824.e9 (2019).

[19] Murphy, T. H. *et al.* High-throughput automated home-cage mesoscopic functional imaging of mouse cortex. *Nature Communications* **7** (2016).

[20] Bolaños, F. *et al.* Mesoscale cortical calcium imaging reveals widespread synchronized infraslow activity during social touch in mice. *bioRxiv* 430306 (2018).

[21] Meyer, A. F., O'Keefe, J. & Poort, J. Two distinct types of eye-head coupling in freely moving mice. *bioRxiv* (2020).

[22] Juczewski, K., Koussa, J. A., Kesner, A. J., Lee, J. O. & Lovinger, D. M. Stress and behavioral correlates in the head-fixed method. *bioRxiv* (2020).

[23] Impaired spatial selectivity and intact phase precession in two-dimensional virtual reality. *Nature Neuroscience* **18**, 121–128 (2015).

[24] Ghosh, K. K. *et al.* Miniaturized integration of a fluorescence microscope. *Nature Methods* **8**, 871–878 (2011).

[25] Cai, D. J. *et al.* A shared neural ensemble links distinct contextual memories encoded close in time. *Nature* **534**, 115–118 (2016).

[26] Zong, W. *et al.* Fast high-resolution miniature two-photon microscopy for brain imaging in freely behaving mice. *Nature Methods* **14**, 713–719 (2017).

[27] Skocek, O. *et al.* High-speed volumetric imaging of neuronal activity in freely moving rodents. *Nature Methods* **15**, 429–432 (2018).

[28] de Groot, A. *et al.* Ninscope, a versatile miniscope for multi-region circuit investigations. *eLife* **9**, 1–24 (2020).

[29] Scott, B. B. *et al.* Imaging Cortical Dynamics in GCaMP Transgenic Rats with a Head-Mounted Widefield Macroscope. *Neuron* **100**, 1045–1058.e5 (2018).

[30] Namiki, S., Sakamoto, H., Iinuma, S., Iino, M. & Hirose, K. Optical glutamate sensor for spatiotemporal analysis of synaptic transmission. *European Journal of Neuroscience* **25**, 2249–2259 (2007).

[31] Marvin, J. S. *et al.* An optimized fluorescent probe for visualizing glutamate neurotransmission. *Nature Methods* **10**, 162–170 (2013).

[32] Denk, W., Strickler, J. & Webb, W. Two-photon laser scanning fluorescence microscopy. *Science* **248**, 73–76 (1990).

[33] Ozbay, B. N. *et al.* Three dimensional two-photon brain imaging in freely moving mice using a miniature fiber coupled microscope with active axial-scanning. *Scientific Reports* **8**, 1–14 (2018).

[34] Ghanbari, L. *et al.* Cortex-wide neural interfacing via transparent polymer skulls. *Nature Communications* **10** (2019).

[35] Ghanbari, L. *et al.* Craniobot: A computer numerical controlled robot for cranial microsurgeries. *Scientific Reports* **9**, 1–12 (2019).

[36] Ying, M. *et al.* Wide-field optical mapping of neural activity and brain haemodynamics: considerations and novel approaches. *Philosophical Transactions of the Royal Society B: Biological Sciences* **371**, 20150360 (2016).

[37] Silasi, G., Xiao, D., Vanni, M. P., Chen, A. C. & Murphy, T. H. Intact skull chronic windows for mesoscopic wide-field imaging in awake mice. *Journal of Neuroscience Methods* **267**, 141–149 (2016).

[38] Mathis, A. *et al.* DeepLabCut: markerless pose estimation of user-defined body parts with deep learning. *Nature Neuroscience* **21**, 1281–1289 (2018).

[39] Dubbs, A., Guevara, J. & Yuste, R. moco: Fast motion correction for calcium imaging. *Frontiers in Neuroinformatics* **10**, 1–4 (2016).

[40] Schindelin, J. *et al.* Fiji: An open-source platform for biological-image analysis. *Nature Methods* **9**, 676–682 (2012).

[41] Ma, Y. *et al.* Resting-state hemodynamics are spatiotemporally coupled to synchronized and symmetric neural activity in excitatory neurons. *Proceedings of the National Academy of Sciences of the United States of America* **113**, E8463–E8471 (2016).

[42] Valley, M. T. *et al.* Separation of hemodynamic signals from GCaMP fluorescence measured with wide-field imaging. *Journal of Neurophysiology* **123**, 356–366 (2020).

[43] Dash, M. B., Douglas, C. L., Vyazovskiy, V. V., Cirelli, C. & Tononi, G. Long-term homeostasis of extracellular glutamate in the rat cerebral cortex across sleep and waking states. *Journal of Neuroscience* **29**, 620–629 (2009).

[44] Abadchi, J. K. *et al.* Spatiotemporal patterns of neocortical activity around hippocampal sharp-wave ripples. *eLife* **9**, 1–26 (2020).

[45] Patti, C. L. *et al.* Effects of sleep deprivation on memory in mice: Role of state-dependent learning. *Sleep* **33**, 1669–1679 (2010).

[46] Colavito, V. *et al.* Experimental sleep deprivation as a tool to test memory deficits in rodents. *Frontiers in Systems Neuroscience* **7**, 1–17 (2013).

[47] Xie, Y. *et al.* Resolution of high-frequency mesoscale intracortical maps using the genetically encoded glutamate sensor iGluSnFR. *Journal of Neuroscience* **36**, 1261–1272 (2016).

[48] Mohajerani, M. H., McVea, D. A., Fingas, M. & Murphy, T. H. Mirrored bilateral slow-wave cortical activity within local circuits revealed by fast bihemispheric voltage-sensitive dye imaging in anesthetized and awake mice. *Journal of Neuroscience* **30**, 3745–3751 (2010).

[49] Dana, H. *et al.* Thy1-GCaMP6 transgenic mice for neuronal population imaging in vivo. *PLoS ONE* **9** (2014).

[50] Li, P. *et al.* Measuring sharp waves and oscillatory population activity with the genetically encoded calcium indicator GCaMP6f. *Frontiers in Cellular Neuroscience* **13**, 1–15 (2019).

[51] Dana, H. *et al.* High-performance calcium sensors for imaging activity in neuronal populations and microcompartments. *Nature Methods* **16**, 649–657 (2019).

[52] Dawson TM, L.-T. C., Golde TE. Animal models of neurodegenerative diseases. *Nature Neuroscience* (2018).

[53] Juneau, J., Duret, G., Robinson, J. & Kemere, C. Enhanced Image Sensor Module for Head-Mounted Microscopes. *Proceedings of the Annual International Conference of the IEEE Engineering in Medicine and Biology Society, EMBS* **2018-July**, 826–829 (2018).

[54] Barbera, G., Liang, B., Zhang, L., Li, Y. & Lin, D.-T. A wireless miniscope for deep brain imaging in freely moving mice. *Journal of Neuroscience Methods* **323**, 56 – 60 (2019).

[55] Ma, Y. Analysis of Resting-State Neurovascular Coupling and Locomotion-Associated Neural Dynamics Using Wide-Field Optical Mapping. *ProQuest Dissertations and Theses* (2018).

[56] Lerner, T. N. *et al.* Intact-Brain Analyses Reveal Distinct Information Carried by SNc Dopamine Subcircuits. *Cell* **162**, 635–647 (2015).

[57] Dana, H. *et al.* Sensitive red protein calcium indicators for imaging neural activity. *eLife* **5**, 1–24 (2016).

[58] Donaldson, P. D., Ghanbari, L., Rynes, M. L., Kodandaramaiah, S. B. & Swisher, S. L. Inkjet-Printed Silver Electrode Array for in-vivo Electrocorticography. *International IEEE/EMBS Conference on Neural Engineering, NER* **2019-March**, 774–777 (2019).

# APPENDIX

# Appendix A

# Mesoscope Assembly

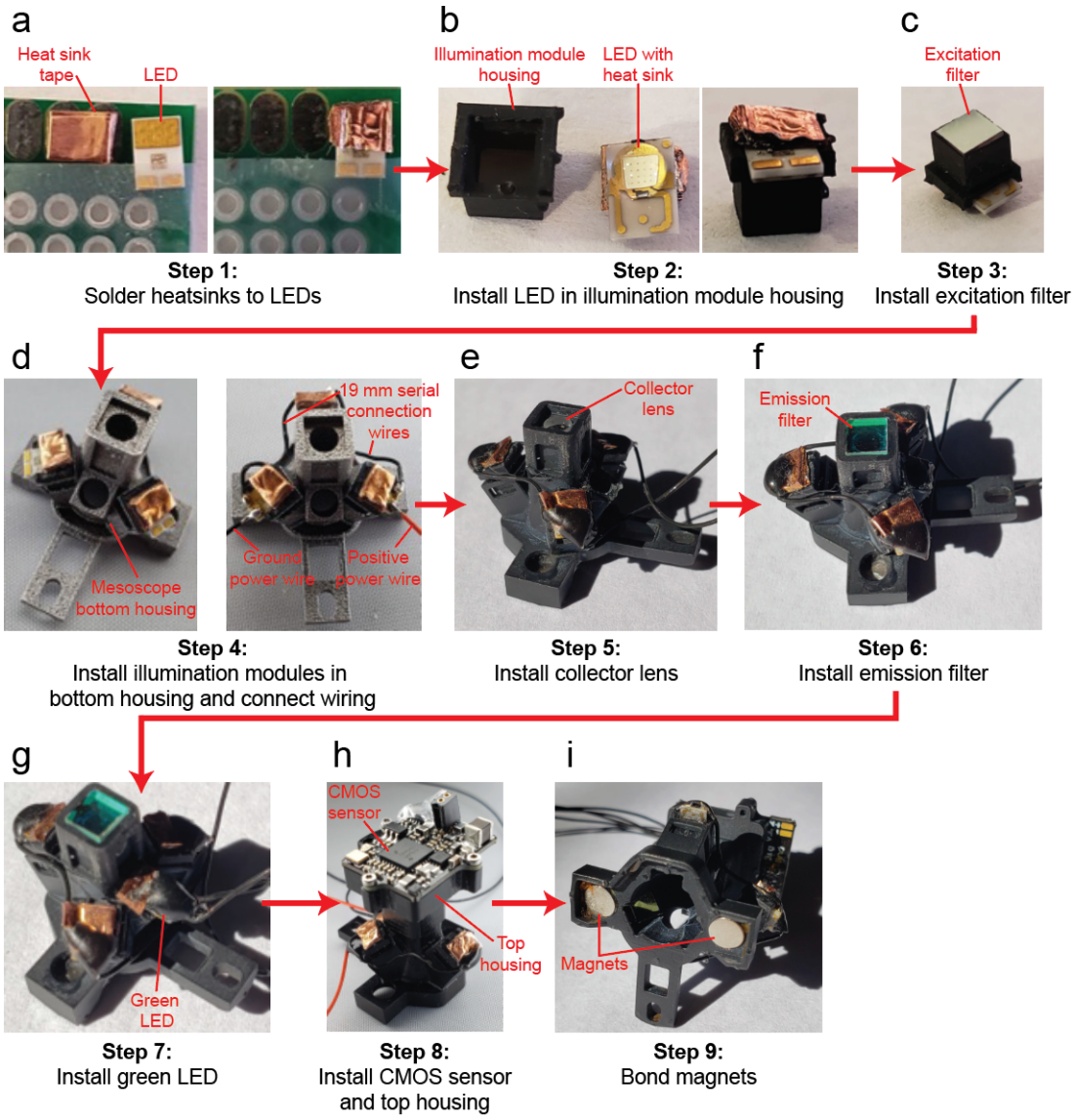


**Figure A.1** Step by step illustration of assembly of the Mesoscope

ASSEMBLY

1. **Pre-fabricate custom parts:** The Mesoscope has custom parts that need to be prefabricated before assembly. These includes the top and bottom housing (**Figure 2.4a**) that are CNC machined out of Delrin and illumination module housings that are 3D printed using a desktop stereolithography (SLA) printer.

1.1. Use *filter_cube_ver5* (Supplementary File 1) to print three illumination module housings. Use files *082019_mesoscope_frame.STL* and *10-15-19_frame_cap* to print the Mesoscope See-Shells and See-Shells protective cover. Clean the 3D printed parts and post cure under UV light.

1.2. Use files *meso4.22_top_delrin* and *meso4.27_bottom_delrin* to CNC machine the top and bottom housing using a 5-axis CNC mill. Alternately, they can be procured from a commercial low volume fabrication services provider (e.g., Protolabs Inc.).

2. **Illumination module assembly:** The illumination module assembly consists of a blue LED, a housing and the excitation filter. Three illumination modules for each excitation light source need to be assembled.

2.1. Solder heat sink to LED: Secure each LED (1416-1028-1-ND, 1416-1035-1-ND, Digikey) to a prototyping board using tape (**Supplementary Figure A.1a left**).

2.2. Measure out approximately 80mm of heat sink copper tape (B071JKLFXX, Amazon). Mix solder paste and flux in a small container and apply it to the heatsink pad on the LED.

2.3. Fold the heat sink tape 4-5 times so that it is layered, then cut to the dimensions of the heat sink pad (**Supplementary Figure A.1a left**).

2.4. Press the folded heatsink onto heatsink pad on the LED using forceps. Apply heat to the copper heat sink using a heat gun at 400F, until solder has melted and solidified. Be sure to keep pressure on the copper heat sink so the melting solder can bind to both the LED heat sink pad and the copper heat sink (**Supplementary Figure A.1a right**).

2.5. Repeat this process for each of the three blue LEDs and one green LED.

2.6. Remove the blue LEDs with heatsinks from prototyping board and place on top of the illumination module housing on the top face with the largest square opening and small extrusions to hold the LED in place (**Supplementary Figure A.1b left**). Secure the LED to the filter cube using a few drops of cyanoacrylate glue (1818A5, McMaster) around the perforated edge that the LED fits tightly into. Be sure to avoid getting drops of super glue on the bulb of the LED. Avoid getting drops of super glue on transparent potting covering the diode. Repeat this step for each of the three illumination modules (**Supplementary Figure A.1b right**).

2.7 Apply a very thin coat of UV-cured optical glue (NOA81, Thorlabs) to the excitation filter (ET470/40x, Chroma) edge and gently insert into the bottom face of the illumination module housing (**Supplementary Figure A.1c**). Use stick tack to handle the filters. Arrows marked on the edge of the diced filters point to the direction of the light propagation. Ensure the filter is inserted in the right orientation. Ensure optical glue does not cover any part of the filter surface. Repeat this step for each of the three illumination modules.

3. **Installing and wiring the illumination module:** Insert the illumination modules into the three illumination arms of the Mesoscope bottom housing (**Supplementary Figure A.1d left**). Cut 2 small pieces of 29-gauge wire to approximately 19 mm (9510T2, McMaster). Cut four 29-gauge wire (2 black and 2 red to provide LEDs power) to the height of the commutator (or power control circuit if no commutator is used). Strip the wires 3-4mm on either side and apply flux to the positive and negative pads of the blue L EDs. Connect the blue LEDs in series using the 19 mm wires. Attach the longer red and black wires to the remaining pads in either terminal of the LEDs wired in series. Check for any shorts in the soldering process. Ensure the LEDs are functioning properly at this step in the assembly. Apply a layer of black epoxy (RS-F2-GPBK-04, FormLabs) to the LED power pads. The epoxy reinforces solder strength at the pad site and provide light shielding (**Supplementary**

**Figure A.1d right**).

4. **Collector lens installation:** Apply optical glue to cylindrical face of the collector lens (47-721, Edmund Optics). Insert into the lens chute within the central shaft of the bottom housing (**Supplementary Figure A.1e**).

5. **Emission filter installation:** Apply optical glue to edges of the emission filter (ET525/50m, Chroma) and insert into the square emission filter slot in the central shaft of the Mesoscope's bottom housing (**Supplementary Figure A.1f**).

6. **Green LED Installation:** Insert green LED into the remaining circular slot within the bottom housing of the Mesoscope and secure using several drops of super glue. Attach power wires to the positive and negative pads of the LED. Check for any shorts in the soldering process. Ensure the LED is functioning properly at this step in the assembly. Insert green LED into the remaining circular slot within the bottom housing of the Mesoscope and secure using several drops of super glue. Apply a layer of black epoxy to the LED power pads. The epoxy reinforces solder strength at the pad site and provide light shielding (**Supplementary Figure A.1g**).

7. **Top Housing attachment:** Use 18-8 M1 torx flat head set screws (96817A704, McMaster) to fasten the CMOS sensor to the top housing. Slide the top housing on the central shaft of the bottom housing. Use the 0-80 adjustment screw (91735A262, McMaster) to secure the top housing in place. Feed the LED power wires through the wire holder in the top housing. Use a little epoxy to fix the wires in place, ensure some slack to ensure strain relief (**Supplementary Figure A.1h**). Additional strain relief points were added along the Mesoscope using heat shrink wrap to keep wires together (repeat as needed for your designs, keep in mind more heat shrink also adds additional weight to the device).

8. **Magnets and fastening nut attachment:** Attach two disk magnets to the bottom surface of the bottom housing (**Supplementary Figure A.1i**).

SOFTWARE INSTALLATION

9. **Miniscope software installation:** Follow the instructions listed on the Miniscope page to install the DAQ software successfully on your computer. It will require installing the Miniscope software in various steps (http://miniscope.org/index.php/Software_and_Firmware_Setup).

10. **Microcontroller software installation:** Download the Arduino software (https://www.arduino.cc/en/main/software). You will additionally need to download the teensy (microcontroller) software (https://www.pjrc.com/teensy/td_download.html). Follow the steps on the Teensy page aforementioned to install the teensy software successfully and interface it with the Arduino library.

WIRING

11. Connect the Mesoscope to the power circuit as shown in **Figure 4.3a, Figure 4.4**. Follow the steps below to connect the power circuit controller to the computer and synchronize with the Miniscope CMOS sensor. **Ensure all ground wires from the DAQ and power supplies are connected to the common ground in the Mesoscope PCB.**

12. Solder wires to the signal and ground pads (urlhttps://imgur.com/a/hgzua), of the CMOS sensor DAQ. These will connect to the microcontroller "trig-in" port (**Figure 4.3a, Figure 4.4**). This will act as the external trigger to start and stop synchronized videos.

13. Strip both ends of a piece of coax cable and separate into signal and ground wires. Solder a wire to each of the separated signal channels on one end, which will connect to the microcontroller "TTL out" port (**Figure 4.3a, Figure 4.4**). Solder the SMA to connector PCB on the other end of the stripped coax cable, which will be attached to the J5 port on the DAQ. This will allow you to collect TTL frame capture signals from the Miniscope DAQ.

14. Set up the two power supplies and ensure they are turned off during setup. Connect both power supply negative leads to the ground rail for each power supply (Supplementary Figure 2b). Connect the positive cable from one power supply to the blue power terminal on the control board. Connect the positive cable from the other supply to the green power

terminal on the control board. You should have a complete illumination power circuit now where the LEDs are powered by each power supply.

TESTING LEDS

15. Now we can test the assembled circuit on any fluorescent object. Connect the Teensy and DAQ data cables to the USB 3.0 cables on the computer. Open the Arduino .ino file called *focusing LED.ino* and upload it to the Teensy. Open the Miniscope software to get a real-time view of the fluorescent molecules. Switch on the green LED power supply and you should see the green LED switch on (and remain on). The power supply should be at around 3V.

Focus the Mesoscope to the desired FOV via the course focusing mechanism and tighten the set screw when a desired focus is achieved. Ensure to not overtighten the screw as it can break the set screw slot. Note green light is used because it can illuminate the cortex at a low power and therefore can be left on without being pulsed at these low powers. If you can see in-focus fluorescent material, the system is working.

USING MESOSCOPE IN AN EXPERIMENT

16. With the Mesoscope focused and the system is wired as shown in **Figure 4.3a, Figure 4.4**, run the *spontaneous pulsing.ino* Arduino file on the Teensy. Ensure all the power supply wiring is correct (especially that the external power supply and signals are sharing the common ground rail with the Teensy). Open the .ino program and set desired parameters.

17. Set **Led_warm_up** to 120 seconds (LEDs are pulsed at moderate powers so they take time to warm up). This means the first 2 or so minutes of the video rendering are usually discarded since the LED dynamics have not stabilized.

18. Set the **experiment time per trial** as desired. The LEDs can usually be run for 6-8 minutes at a time before they start to heat up, so keep this in mind for the total time.

19. Set the **total number of trials**. The LEDs will warm up and the experiment time for

one trial will be added to the first trial (i.e. if LEDs are 120sec to warm up and experiment time is 10 seconds, the first experiment trial will be finished at 130 sec. If there are more trials, i.e. 2, the second trial will occur between 130-140 seconds as the LEDs do not need to be warmed up again).

20. Set the blue LED pulse time (20 ms is recommended for 30 Hz acquisition) and the green LED pulse time (4 ms is recommended for 30 Hz CMOS acquisition). Note that the LED pulse time should be less than the duration of the specified framerate (i.e. if the frame rate is 60 Hz, 1 frame is captured every 16.66 ms. As the LEDs are pulsed on and off between frames, the LED pulse duration has to be less than 16.66 ms (usually 5-6 ms less than the frame rate works well).

21. Upload the .ino code with the set parameters to the Teensy

22. LED pulsing is synchronized to the frame capture of the Miniscope CMOS. Open the Miniscope software and connect the Miniscope CMOS. Set the desired frame rate (60hz usually drops a lot of frames so may not be recommended) and set the gain to a desired value (usually in the 50s). Tick the "trigger ext" box (by the record button); this will allow the microcontroller to trigger a video.

23. In Arduino, navigate to Tools, Serial Monitor. This will prompt the user (you) to enter the character 'y' to trigger the camera and begin recording the trial once the character command has been entered. Check the settings are correct and begin the trial. Usually the first trial is a test trial where you adjust the gain and LED power settings to ensure you are within the CMOS dynamic range (no over-saturation in the FOV).

24. Adjust the LED powers until you have sucient illumination. The blue LEDs are usually run around 9-10V. The green LED is usually set to 4-6V. If the green LED is not required or desired, simply leave this power supply off during testing.